The Thesis Committee for Justin David Lowrey
Certifies that this is the approved version of the following thesis:

Production and Subsurface Vertical Transport of Radioxenon Resulting from Underground Nuclear Explosions

APPROVED BY
SUPERVISING COMMITTEE:

Supervisor:

Steven Biegalski

Mark Deinert

Production and Subsurface Vertical Transport of Radioxenon resulting from Underground Nuclear Explosions

by

Justin David Lowrey, BS

Thesis

Presented to the Faculty of the Graduate School of

The University of Texas at Austin

in Partial Fulfillment

of the Requirements

for the Degree of

Master of Science in Engineering

The University of Texas at Austin

December 2010

Dedication

To my parents for always keeping faith in me and to Jen for keeping me grounded even in the roughest times.

Acknowledgements

Completion of this thesis would not have been possible without the immeasurable guidance, encouragement, and good leisure conversion of Dr. Steven Biegalski; thank you for always making time. I would also like to express deep gratitude for the good humor and support of Dr. Sheldon Landsberger, without whom I would have never considered the field of nuclear engineering and would not have returned to the University of Texas at Austin.

Lastly, this thesis is based upon work supported by the Department of Energy, National Nuclear Security Administration under Award Number DE-AC52-09NA28608.

December 2010

Abstract

Production and Subsurface Vertical Transport of Radioxenon resulting from Underground Nuclear Explosions

Justin David Lowrey, M.S.E.

The University of Texas at Austin, 2010

Supervisor: Steven Biegalski

Atmospheric monitoring of radionuclides as part of the International Monitoring System requires the capability to differentiate between a radionuclide signature emanating from peaceful nuclear activity and one emanating from a well-contained underground nuclear explosion. While the radionuclide signatures of nuclear weapons are generally well known, radionuclides must first pass through hundreds of meters of earth to reach the surface where they can be detected and analyzed. Less well known is the affect that subsurface vertical transport has on the isotopic signatures of nuclear explosions.

In this work, a model is developed, and tested, simulating the detonation of a simple underground nuclear explosion and the subsequent vertical transport of resulting radioxenon to the surface. First, the fast-fission burn of a fissile spherical core surrounded by a layer of geologic media is modeled, normalized to 1 kton total energy. The resulting

source term is then used in the testing and evaluation of the constructed vertical transport model, which is based on the double-porosity model of underground fluid transport driven by barometric pumping.

First, the ability of the vertical transport code to effectively model the underground pressure response from a varying surface pressure is demonstrated. Next, a 100-day simulation of the vertical migration of a static source is examined, and the resulting cumulative outflow of roughly 1% initial inventory outflow per cycle is found to closely follow the analytical predictions. Finally, calculated radioxenon source terms are utilized to model the resulting vertical transport and subsequent surface outflow. These results are found to be consistent with the physical expectations of the system, and lastly a cursory sensitivity analysis is conducted on several of the physical parameters of the model. The result is that the vertical transport model predicts isotopic fractionation of radioxenon that can potentially lie outside of currently accepted standard bounds.

Table of Contents

List of Tables

List of Figures

Chapter 1: Introduction

1.1 MOTIVATION

Since the signing of the Limited Test Ban Treaty in 1963, a majority of nuclear explosions tests have been carried out in underground facilities intended to contain the fission products that result, therefore minimizing evidence of the explosions. Three decades later in September 1996, the Comprehensive Test Ban Treaty (CTBT), an international resolution banning any and all nuclear explosions, was opened for signatures; to date the treaty has been signed by 182 countries and ratified by 153 countries [1]. Implicit in the CTBT is the need for a cooperative, global capacity to reliably detect underground nuclear explosions. The International Monitoring System (IMS) is a 321-station network spread out around the globe (see Figure 1.1), consisting of seismic, infrasound, hydroacoustic, as well as radionuclide monitoring technologies [2]. Along with established lines of international consultation, clarification and on-site inspections, the IMS is a major component in the CTBT verification system.

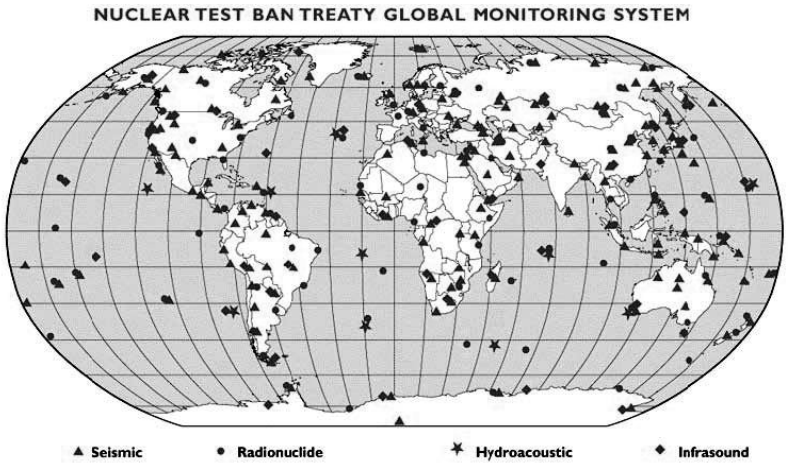

Figure 1.1. Global distribution of IMS stations.

Underground nuclear explosions directly inject the surrounding geologic media with resultant fission products, as well as induce radionuclide production through neutron activation of soil and rock components. What results is a distribution of radionuclides within the geology hundreds of meters below the surface known as the initial contaminant distribution halo. Vertical transport by a number of mechanisms inevitably brings some amount of this contaminant to the surface and into the atmosphere where it can be detected by specific atmospheric monitoring stations. Of the 321 stations in the IMS network, 80 serve to monitor radionuclides in the atmosphere [2]. These stations are generally located strategically in areas of rapid wind mixing to facilitate a high volume air sampler, which filters and collects radioactive particulates. These filters are subsequently counted with gamma ray detectors to determine activity levels of various radionuclides that might be present.

Monitoring of radionuclide levels in the atmosphere faces a number of challenges. First and foremost, clandestine nuclear explosions are assumedly conducted with the intent of containing as much of the explosion evidence as possible to prohibit detection. Accordingly, in an effort to increase radionuclide detection efficiency and reliability, the International Noble Gas Experiment, started in 1999, developed and deployed at IMS stations four different types of xenon detectors [2]. Xenon, as a noble gas fission product, is of special interest in atmospheric monitoring for underground nuclear activity because chemically it is largely nonreactive, and therefore it can be expected to transport relatively free of filtering. Xenon is present naturally in the atmosphere at a level of 0.087 ± 0.001 parts per million with the natural isotopic abundances listed in Table 1.1 [3].

Table 1.1. Natural abundance of Xenon Isotopes

Xe Isotope	Natural Abundance
^{124}Xe	0.095%
^{126}Xe	0.089%
^{128}Xe	1.91%
^{129}Xe	26.4%
^{130}Xe	4.07%
^{131}Xe	21.2%
^{132}Xe	26.9%
^{134}Xe	10.4%
^{136}Xe	8.86%

Radioactive isotopes of xenon in the atmosphere, however, are largely anthropogenic in origin [4] [5]. So-called radioxenon is primarily produced as release from the commercial nuclear power industry as well as in the medical industry, but radioxenon is also released in nuclear explosions. This leads to a second major challenge to atmospheric monitoring of radionuclides – generally speaking nuclear explosions are far from the only source of radionuclide production in the modern world, thus identifying a particular radioisotope signal as emanating from a nuclear explosion is not trivial. Peaceful nuclear applications, such as for power generation and medical isotope production, have associated with them their own radionuclide signatures that can potentially serve to mimic or obscure more concerning signs of weapons applications. As such, not just the activity levels of radionuclides in the atmosphere, but their isotopic ratios are of central importance to atmospheric monitoring and distinguishing sources of nuclear explosions from other anthropogenic sources.

A major objective of IMS atmospheric monitoring is to observe radioxenon signals and examine the ratios of four xenon isotopes, ^{135}Xe, ^{133}Xe, ^{133m}Xe and ^{131m}Xe for comparison with expected values for nuclear explosion sources. Being able to predict the isotopic ratio signatures produced by underground nuclear explosions is therefore crucial to the effectiveness of atmospheric monitoring of radionuclides. Currently, the bulk of the

knowledge and methods used to predict these signatures have focused on simply modeling the production source. Largely neglected in these calculations are the effects of chemical and isotopic fractionation that occur as a result of environmental transport of radioxenon and its parent radionuclides. As compared to the point of production hundreds of meters beneath the surface, this fractionation can significantly alter the isotopic ratios before radioxenon reaches the surface and atmosphere. Given that atmospheric monitoring for radionuclides is the only IMS technology by which a nuclear explosion can be positively verified, a greater understanding of the various physical phenomena responsible for subsurface radionuclide transport is essential.

1.2 NPE GAS TRACER EXPERIMENT

1.2.1 The Experiment

Following the signing of the CTBT in 1996, the Comprehensive Test Ban Treaty Research program was initiated for the purpose of researching technologies of potential use for on-site inspections (OSI). Within this, the Lawrence Livermore National Laboratory On-Site Inspection project considered four technologies that were considered particularly promising for use in an OSI, yet insufficiently developed. One such technology considered was noble gas transport modeling and sampling, carried out as part of the Non-Proliferation Experiment [6].

The Non-Proliferation Experiment (NPE), conducted by Lawrence Livermore National Laboratory (LLNL), entailed the September 22, 1993 detonation of a one-kiloton chemical explosion within Rainier Mesa at the Nevada Test Site. Situated at a depth of about 400m below the surface, the NPE afforded a unique opportunity to simulate the release and subsequent transport of radionuclides from a nuclear event. As a

whole, the NPE consisted of a broad range of goals. First, on-site, pre-shot, shot-time, and post-shot measurements of gas seepage and seismic activity were taken to mimic challenge on-site inspection scenarios. Second, there was the objective of comparing the underground chemical explosion with the measurements of nearby nuclear test explosions within the same geologic medium. Lastly were a number of university-set scientific objectives regarding the structure of the regional crust and upper mantle, examined by seismic stations located across the region [7]. The specific aim of the LLNL OSI project was to determine whether a well-contained underground explosion could be detected by gas sampling along nearby geologic faults, and if so, to define a basis for predicting the detectability of quickly decaying radionuclides that could be positively linked to fission products from a nuclear detonation [6].

The setup of the NPE was as follows. Approximately 1.29 kg of ANFO[1] blasting agent was placed within a 15.2 m diameter, 5.5 m tall cylindrical cavity. Within the cavity two samples of tracer gas, 8 m^3 of SF_6 and 1.3 m^3 of ^3He were placed. Sulfur hexafluoride, SF_6, is a relatively inert compound of high molecular weight (146), good thermal stability, and was detected at background levels of only 3 ppt (parts-per-trillion by volume) at the test site. Helium-3 similarly existed at very low background levels, only 7.34 ppt. To detect the concentration of SF_6 in gas samples, chromatography was used, while mass spectrometry was used to determine ^3He concentrations

Over a roughly 500-day period following the detonation, 200 gas samples were collected in the region and analyzed for traces of the gases. Figure 1.2 shows an overview of the NPE site at Rainier Mesa [8]. A NOAA[2] weather station located at an elevation of 2286m on Rainier Mesa recorded barometric readings throughout the duration of the

[1] AN/FO, ammonium nitrate/fuel oil; by far the most common type of explosive utilized in North America
[2] National Oceanic and Atmospheric Administration, United States Department of Commerce

experiment. Sampling sites as indicated in Figure 1.2 can be broadly categorized as either being located on pre-existing fault lines or near the point of detonation. Fault line stations were sampled most often, but during "barometric events," additional surface samples were collected at stations near the detonation point. It would turn out that only one ground zero gas sample ever recorded a SF_6 concentration above background. Due to heavy snows, the majority of samples were collected during the fall and spring following the detonation, particularly during periods of deep barometric depressions [6].

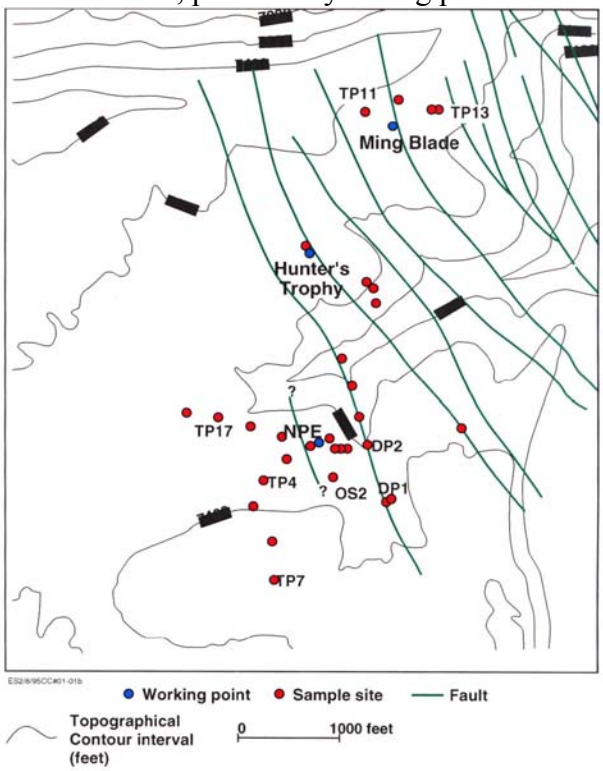

Figure 1.2. Surface distribution of soil gas sampling stations. Stations denoted 'OS' and 'DP' are located on pre-existing faults or fissures. Note also that Hunter's Trophy is the site of a previously conducted underground nuclear explosion [6].

1.2.2 NPE Results

Table 2 summarizes the gas sampling observations [6]. Over a period of 508 days, thirteen samples were identified as positive for SF_6, the first of which came 50 days following the detonation at the site OS-6. Like all but one of the locations of positive samples, this station site is located on a pre-existing fault several hundred meters from the point of detonation, near to the site of a previously conducted underground nuclear explosion called Hunter's Trophy. This initial positive sample followed a number of large barometric depressions. Of particular interest is that while SF_6 was subsequently detected well above background in a few other sample suites, no amounts were seen in many additional sample suites, as indicated by the "no detects" in Table 1.2. Helium-3 was not detected significantly above background levels until day 375 following the detonation, 325 days following the initial detection of SF_6.

Table 1.2. Summary of Rainier Mesa Gas Sampling Observations from the NPE [6].

Sample Suite	Date	No. Sites F=fracture S=soil	Total Detects (Total Samples)	Locations of SF_6 Detection	SF_6 Conc., ppt	Locations of ^3He Detection	^3He Conc., ppt	Barometric Pressure (mbar)
1	08-Jul-93	3F	0 (3)		ND		-	772.1
2	11-Aug-93	3F	0 (5)		ND		ND	775.2
3	09-Sep-93	3F	0 (6)		ND		ND	777.6
4	22-Sep-93	Tunnel Port	0 (2)		ND		ND	772.5
5	24-Sep-93	3F	0 (3)		ND		-	778.2
6	10-Nov-93	3F	0 (6)	OS-6	340		ND	764.8
7	17-Mar-94	3F	1 (7)	OS-1	540		ND	771.2
		3F		OS-6	580			
		3F		OS-6	280			
8	23-Mar-94	3F	1 (6)	OS-1	580		ND	765.3
		3F		OS-2	450			
		3F		OS-3	400			
9	17-May-94	2F	3 (2)		ND		-	765.2
10	19-May-94	3F	0 (3)		-		ND	770.7
11	11-Aug-94	1F	0 (1)		ND		-	779.1
12	29-Sep-94	5F	0 (9)		ND		ND	771.6
13	04-Oct-94	1F	0 (11)		ND		ND	766.6
14	06-Oct-94	5F	2 (11)	OS-1	13	OS-6	8.42	771.2
15	12-Oct-94	5F	1 (12)	OS-3	18		ND	769.8
16	02-Nov-94	6F	3 (15)	DP-1	45	DP-1	9.22	760.9
		6F		OS-6	45			
17	03-Nov-94	8F	0 (15)		ND		ND	764.5
18	10-Nov-94	13S	3 (41)	DP-1	18	DP-1	21.4	760.8
		6F		TP-4	9			
19	16-Nov-94	18S, 8F	1 (40)		ND	DP-1	14.7	762.8

An important goal of the LLNL OSI project team was to develop a basis for future prediction of the detectability of rapidly decaying radionuclides unambiguously emanating from nuclear detonations. To this end, a numerical model of tracer transport was developed with two broad points in mind, both of which were strongly supported by the results of the NPE. First, the fact that all but one positive sample came at stations located near pre-existing faults considerable distances from the detonation point lends support to the theory that fractures within an otherwise homogeneous geologic media (matrix) provide "fast tracks" for the migration of contaminants to the surface. The study of continuous and networked fractures and their role as effective contaminant transport was undertaken in the 1970's by a handful of groups including Wilson and Witherspoon (1970), Nelson and Handin (1977), and Gale (1979) [9], [10], [11]. A second key element of the NPE migration study was the magnitude of the affect of variations in surface pressure on bringing a tracer contaminant to the surface, a process termed *barometric pumping* first modeled as a source of tracer transport by Nilson and Lie (1990), which will be described in great detail below and constitutes the bulk of this thesis [12]. While large barometric depressions tended to precede the positive sample results in the NPE, smaller amplitude, higher frequency barometric variations seemed to have little effect on the detection of trace gas.

1.3 BAROMETRIC PUMPING

Binary gas diffusion has long been known to be too slow to account for the transport of detectable concentrations of rapidly decaying radionuclides from hundreds of meters underground to the surface. Two well-considered examples are ^{37}Ar and ^{133}Xe, radionuclides of particular interest in atmospheric monitoring having short half-lives of 34.8 days and 5.2 days, respectively. Additionally, long term, highly pressurized

subsurface sources are ineffective in pushing gases to the surface – gas flow in this scenario is typically largely horizontal due to the anisotropic permeability of geologic layers [6]. Alternatively, as demonstrated in the results of the NPE, a deep, extended drop in surface pressure can be very effective in the transport of subsurface gas to the surface.

The concept of barometric pumping is simple. Consider a concentration of trace gas located deep beneath the surface within the rock matrix. During periods when the barometric pressure falls below the ambient pressure of the formation, tracer gas within fractures is pulled upwards. The flow is complicated by the fact that, as the gas travels along the fracture it also has the opportunity to diffuse horizontally back into the higher levels of rock matrix. As a result, the concentration of a trace gas moving along a fracture toward the surface during a pressure low will tend to decrease. When the barometric pressure rises higher than the pressure in the formation, gas within the fractures is pushed back downwards, and again the tracer gas escapes into rock matrix through the porous fracture walls. On the next cycle, decreasing pressure again pulls trace gas from the matrix upwards through the fractures. The effect of fracture-matrix diffusion in these cycles is that low/high pressure cycles are not completely reversible – even if pressure variations are perfectly sinusoidal, there is a net upward "ratcheting" of the tracer concentration front.

Models, both numerical and analytical, of subsurface gas transport have been explored well before the NPE-migration model reported on by the LLNL team. Of particular relevance to this thesis are two works by Grisak and Pickens (1980) and Tang et al. (1981), which demonstrated the role of fracture-matrix interactions in controlling the rate of contaminant migration in hydrological applications. In the former study, a

finite element model was developed for solute transport by advection[3], mechanical dispersion, and diffusion in single-direction flow field [13]. Similarly, the later study considered an analytical solution to tracer transport within a fracture surrounded by saturated porous rock. Additionally, however, the Tang study considered molecular diffusion both along the fracture axis as well as into the surrounding matrix, adsorption[4] in the matrix, and lastly radioactive decay [14]. In 1984, Neretnieks and Rasmuson developed an integrated finite difference scheme to model radionuclide migration that examined variation in both fracture cross section and fluid velocity, which ultimately demonstrated how simplified models of 1D transport could be extended to more complex configurations [15].

The first actual trace gas vertical transport model based on barometric pumping as the primary transport mechanism was developed by Nilson and Lie (1990). This finite difference based numerical model considers a double-porosity formulation[5] in which fractures are the dominant pathways by which contaminants migrate, and fracture-matrix interactions play a critical role in determining the rate of migration [12], [16], [17].

Finally and somewhat more recently, the **N**on-isothermal **U**nsaturated-Saturated **F**low **T**ransport (NUFT) model was developed by Nitao (1996) and utilized in the NPE-migration model by the LLNL OSI team [18], [19], [20]. Using this model and based on the results of the NPE, Carrigen et al. made predictions regarding the vertical transport of ^{37}Ar and ^{133}Xe due to barometric pumping. Beginning with an initial source of 9.7×10^{12} Bq of ^{37}Ar and 6.7×10^{15} Bq of ^{133}Xe, they used the 1D model based on Nilson and Lie

[3] Advection refers to transport of a substance due to the bulk motion of a fluid.
[4] Adsorption refers to the adhesion of atoms or molecules to a surface, as opposed to *absorption* within a permeable liquid or solid
[5] Double-porosity models of fracture and matrix systems were previously looked at in Gringarten (1984) and Chen (1989), referenced in the bibliography.

(1990) to calculate a resulting surface concentration of 6 Bq/m^3 after 80 days and 41 Bq/m^3 after 50 days for ^{37}Ar and ^{133}Xe respectively.

1.4 STATEMENT OF GOALS

Of utmost importance to the accuracy and reliability of radionuclide monitoring for IMS on-site inspections is the capacity to unambiguously identify a radioisotope signature as one emanating from an underground nuclear explosion as opposed to a source of a peaceful nature. In order to distinguish one radioisotope signature from another, the expected isotopic ratios of important radionuclides must be known. While the ability to well-define such ratios as they are produced by nuclear explosions exists, challenge on-site inspections can only study samples once radionuclides have transported through hundreds of meters of rock to reach the surface. The effects of vertical transport on isotopic fractionation are not as well understood. The broad goal of this work is to develop a vertical transport model for xenon and its parent nuclides as they result from an underground nuclear explosion in an effort to better understand the effects of this transport on the isotopic ratios of xenon.

To accomplish a self-contained transport model, the first task is to define a source term – that is, to calculate an inventory of the concentration or activities of the radionuclides that result from a nuclear explosion. In particular, the source term in this work will be time-dependent, and entail tracking the quantities of xenon isotopes ^{131m}Xe, ^{133m}Xe, ^{133}Xe, and ^{135}Xe, as well as their parent radionuclides. Next, a vertical transport model following the scheme defined by Nilson and Lie (1990) is to be developed. The code should consider 1D tracer transport in a double-porosity model. Additionally, it should accept a generalized pressure function, user-defined physical parameters, as well

as a time varying source term to calculate the outflow of tracer gas from the surface. Properties of the particular gas transport to be modeled will be specified through the diffusion coefficient. Lastly, a brief sensitivity study is to be carried out to gain initial insight into the effects of varying the system's physical parameters on the resulting outflow of radioactive contaminant.

Chapter 2: Theory

2.1 Source Term Model

This first section concerns the theory and assumptions behind determination of the source term resulting from a 1 kton nuclear explosion. A source term can be thought of as an inventory of all the radionuclides resulting from the detonation of a nuclear explosion. Of particular importance to this work is radioxenon; among other radionuclides, the source term needs to track the production of ^{131m}Xe, ^{133m}Xe, ^{133}Xe, and ^{135}Xe, as well as their parent radionuclides. The time-varying source term will later serve to determine the amount of a particular radionuclide that gets created and added in the vertical transport model at each step in time considered.

2.1.1 A Nuclear Explosion

A nuclear explosion derives its energy output from either fission reactions, or a combination of fission and fusion reactions depending on the specific design of the detonation device. Broadly speaking, two basic concepts of a nuclear weapon exist – the first is the atomic, or fission bomb, and is composed of a mass of fissile material configured in such a way that a fission chain reaction is possible. The second, more complex nuclear design type is that of a thermonuclear, or hydrogen bomb. This type of device typically consists of a primary fission bomb that serves to compress and heat a secondary fusion fuel, comprised of tritium, deuterium, etc.

While many heavy elements are *fissionable*, fissile material within a fission bomb generally consists of either ^{235}U or ^{239}Pu. These particular isotopes are capable of sustaining the exponentially growing fission chain reactions characteristic of the energy capability of a fission bomb. Fission is induced by the collision of a free neutron with a fissionable nucleus, the result being that the nucleus splits into smaller nuclei (fission

products), gamma rays, one or more free neutrons, as well as a release of energy. Upon fission, a ^{235}U nucleus can split in dozens of ways, but one such fission reaction can be written

$$^{235}\mathrm{U} + n \rightarrow {}^{95}\mathrm{Sr} + {}^{139}\mathrm{Xe} + 2n + 180\ \mathrm{MeV}$$

Note that in this particular fission reaction, two neutrons result where only one was needed to undergo the fission. Once a fission reaction within a mass of fissionable material is initiated, whether the reactions are self-sustainable or "fizzle" out depends on whether the assembly is in a *critical* state. Given a specific geometric configuration, the critical mass can be defined as the smallest quantity of fissile material that must be present to sustain the fission chain reaction. The criticality of a nuclear system can be quantified by the neutron multiplication factor, k, which is simply the ratio of the average number of neutrons released per fission to the number lost. A value of $k \geq 1$ for a system means that a fission chain reaction can ensue because on average, for each fission reaction that consumes a neutron, at least one neutron is released back into the system to induce further fissions. A fission bomb requires a critical assembly of fissile material and a means to initiate the fission chain reaction (two such means are shown in Figure 2.1).

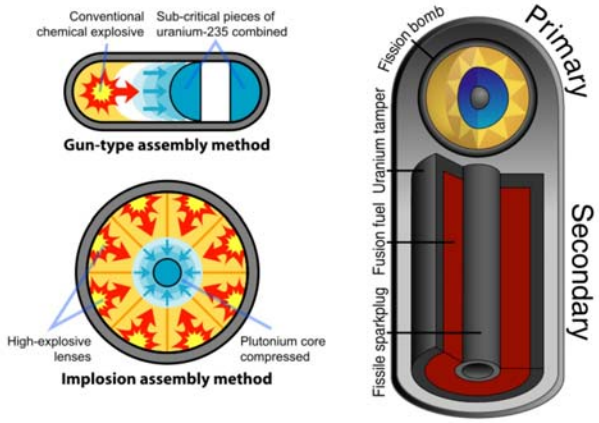

Figure 2.1. Two general types of nuclear devices; left: the two most common fission device designs, and right: the Teller-Ulam thermonuclear device design [21].

A key factor in fission reactions, as described above, is the number of neutrons within the system capable of inducing fission. A thermonuclear device, in addition to utilizing a fission device, relies on a secondary fusion process to essentially multiply the number of very high energy neutrons in the system. These types of devices can be built in increasingly complex design with no theoretical limit to the number of fission/fusion stages they can contain. A fusion reaction involves the interaction of two light nuclei at extremely high temperature and pressure resulting in the release of two or more products. A typical fusion reaction relevant to the fusion fuel used in a thermonuclear device might be

$$^{2}_{1}\mathrm{D} + {}^{2}_{1}\mathrm{D} \rightarrow {}^{3}_{1}\mathrm{T}\ (1.01\ \mathrm{MeV}) + p\ (3.02\ \mathrm{MeV}) \qquad 50\%$$
$$^{2}_{1}\mathrm{D} + {}^{2}_{1}\mathrm{D} \rightarrow {}^{3}_{2}\mathrm{He}\ (0.82\ \mathrm{MeV}) + n\ (2.45\ \mathrm{MeV}) \qquad 50\%$$

Of particular importance in this reaction are the 2.45 MeV fast neutrons that can result. In a thermonuclear device like the one depicted on the right side of Figure 2.1, first a fission device is detonated, which raises the heat and pressure of the fusion fuel to the point that fusion reactions are initiated. The large number of very fast neutrons that result from fusion reactions can then induce fission in materials like depleted uranium that are not fissioned easily. By stacking fission/fusion stages, a thermonuclear device of any yield can theoretically be designed.

2.1.2 Modeling a Nuclear Explosion

Only a simplified model of a fission-only system will be considered in this work. This choice is believed justified as follows. With regard to a proliferation scenario in which an industrial nation is in a developing stage of its nuclear weapons program, the technological challenges associated with building a thermonuclear explosion device precludes that it would first design and test simpler, fission devices [22]. This

technological progression has its precedent in the history of nuclear-capable nations. To date, only six[6] nations worldwide have detonated thermonuclear-type explosions; these are the Unites States, Russia, the United Kingdom, China, France, and India – all nations with advanced, well-established nuclear infrastructures [23].

Production of radionuclides by a fission device detonated underground occurs predominantly by two processes. The first yields the fission products associated with the fission reactions that take place within the device itself before being blown apart by the explosion. Also of importance are *activation products* that result from non-fission reactions induced by free neutrons. Neutrons produced by fission reactions in the nuclear device can escape into the surrounding media where they may undergo one or more interactions with nuclei. A typical fast neutron produced within the exploding core that escapes into the surrounding geologic medium can interact with nuclei in that medium in all the following ways: scattering (elastic and inelastic), radiative capture, charged-particle interactions, fast neutron reactions, and in some instances even fission.

The two primary interactions between free neutrons and nuclei within the surrounding geologic media that need be considered are inelastic scattering and neutron activation through radiative capture. Inelastic scattering is the primary interaction by which a high energy neutron is slowed down, and can be summarized by the simple expression

$$n + {}^{A}Z \rightarrow {}^{A}Z' + n'$$

where ${}^{A}Z'$ and n' denote the same nucleus and neutron but with altered kinetic energies. Fast neutrons scattering from much heavier nuclei will typically lose momentum as a

[6] There is some lingering debate regarding whether India has actually detonated a true, multi-stage thermonuclear weapon.

result of the interaction; successive interactions of this type will eventually reduce neutron energies by several orders of magnitude.

Neutron activation by radiative capture occurs when a neutron is captured by a nucleus, ${}^{A}Z$, thus creating an isotope of the nucleus that is heavier by one neutron, which is typically in an excited, meta-stable state, denoted ${}^{A+1}Z^{*}$. Upon de-excitation a gamma-ray is given off, leaving ${}^{A+1}Z$. Radiative capture can be summarized

$$n + {}^{A}Z \rightarrow {}^{A+1}Z^{*} \rightarrow {}^{A+1}Z + \gamma .$$

The final product ${}^{A+1}Z$ of this reaction is often itself radioactive, and subsequently undergoes beta decay to yield other nuclei also termed activation products within the source term. In addition to simple radiative capture, fast neutron interactions can also occur in an underground nuclear explosion. Of particular importance is the production of radioactive ${}^{37}\mathrm{Ar}$ through

$$n + {}^{40}\mathrm{Ca} \rightarrow {}^{37}\mathrm{Ar} + \alpha .$$

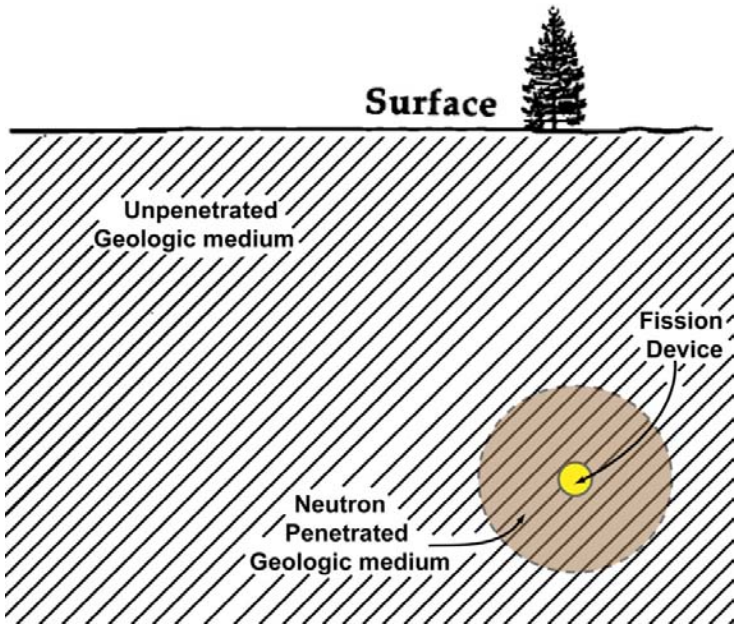

Figure 2.2. Depiction of the simple nuclear explosion model, not drawn to scale. Modified from an illustration in [24].

The simplest possible model of an underground nuclear explosion consists of the 2D configuration depicted in Figure 2.2. In this model, there are only two regions of interest: the fission device and the surrounding neutron-penetrated geologic medium. The fission device can be modeled as a small, spherical, critical assembly of fissile material in which fission occurs to produce a distribution of neutrons. Surrounding the fission core is a spherical region of geologic medium; neutrons that escape the core interact with nuclei of this medium. A basic assumption inherent in this model is that the nuclear detonation occurs at a depth deep enough that all of the free neutrons are eventually absorbed in the geologic medium.

2.1.3 Calculation of the Source Term

To model the neutron flux within the fission core as well as in the surrounding geologic medium, the code MCNP is to be utilized. MCNP is a general **M**onte **C**arlo **N**eutral-**P**article code used for the simulation of neutron, electron, or photon transport. This code is capable of modeling an arbitrary 3D configuration of various material cells with specified boundaries. With the neutron flux profiles generated in MCNP as input, the code ORIGEN 2.2 is used to model the resulting material compositions resulting from the various particle interactions. To facilitate this inter-program functionality, MONTEBURNS is used. MONTEBURNS is essentially a PERL script that takes an MCNP input file with specified system geometry and initial material compositions, calculates and transfers one-group cross-sections and flux values to ORIGEN, which in turn calculates and returns to MCNP the resulting material compositions. These cycles, or burn steps, are repeated until the desired energy burnup is achieved.

Modeling of the system using MONTEBURNS requires specification of all of the following major parameters: geometry of the system's various cells, initial material

composition within those cells, all boundaries and boundary conditions, total time to burn, power output, number of burn steps, and which nuclides are to be explicitly tracked in MONTEBURNS.

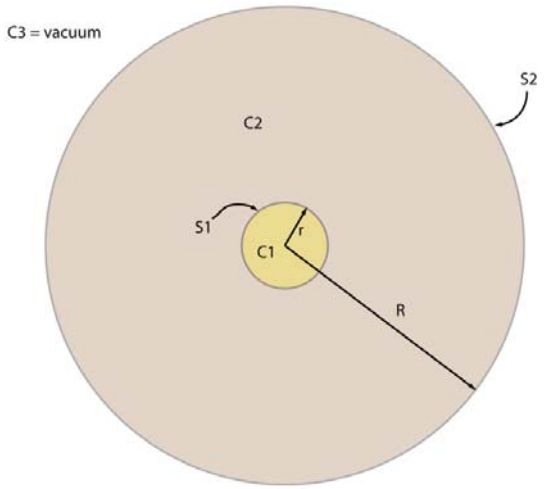

Figure 2.3. Explosion model to be used in MCNP, with C1 (cell 1) being the fission core, and C2 the surrounding geologic medium.

Two compositions of fissile materials are to be considered for the fission core, one consisting of weapons-grade uranium and the other plutonium, the compositions of which are shown below in Table 2.1 [25]. Figure 2.3 represents a simple illustration of the model geometry. Given these compositions, a $k = 1$ assembly requires the cores to be of radius $r = 8.7$ cm for HEU and $r = 5.1$ cm for Pu. These radii can be found through simple trial and error by running kcode calculations in MCNP with the system modeling only the spherical cores. See A.1 of the Appendix for an example MCNP input deck used for a kcode calculation to determine the effective k of a given core configuration.

Since a true underground explosion scenario would take place hundreds of meters beneath the surface, the radius of the surrounding geologic medium, R, should ideally be of the same order as the depth of the device. However, not only is it computationally

ineffectual to simulate millions of cubic meters worth of medium, but it is also unnecessary due to neutron attenuation and eventual capture. As a result, the parameter *R* is a variable parameter to be determined in such a way that a satisfactory fraction of all neutrons in the system eventually die within the system without escaping into the vacuum cell surrounding the geometry, as shown in Figure 2.3.

Table 2.1. Composition of Weapons-Grade U & Pu [25].

Weapons-Grade U (HEU)		Weapons-Grade Pu	
^{234}U	0.12	^{238}Pu	0.01
^{235}U	94.00	^{239}Pu	93.80
^{238}U	5.88	^{240}Pu	5.80
		^{241}Pu	0.13
		^{242}Pu	0.02
		^{241}Am	0.22

The goal of the source term calculation is to calculate an inventory of radionuclide activities resulting from a nuclear explosion, normalized to a total of 1 kiloton total energy release, or 4.184×10^{12} J. MONTEBURNS requires an average power as one of its input parameters. Estimating the time of explosion to be 1μs, the average power output can easily be calculated to be

$$P = \frac{4.184\times10^{12}\,\mathrm{J}}{10^{-6}\,\mathrm{s}} = 4.184\times10^{18}\,\mathrm{W} = 4.184\times10^{12}\,\mathrm{MW}\,.$$

Lastly, the composition of the surrounding geologic medium needs to be defined, element by element. Compositions of five different mediums are presented in A.2 of the Appendix, three of which constitute rock estimates and two soil estimates. These compositions assume natural isotopic abundances. These five samples have been chosen for consideration in this study in large part because they likely represent upper and lower bounds for the number of activation products produced in the media surrounding the fission device. Note that the five estimates vary little in the concentrations of the majority

of elements; the most notable exceptions are in the estimates of H and Fe concentration, the former due mainly to a difference in the treatment of water within the studies. Hydrogen and iron both act as neutron moderators, for they have relatively large inelastic neutron scattering cross-sections. Iron in particular interacts very strongly with thermal neutrons. The presence of these nuclei in the medium around the fission device is likely to mean a quicker attenuation of the outward neutron flux, therefore altering the distribution of activation products that result.

2.2 Overview of Transport

The intent of this section is twofold. First, the basic terminologies and principles underlying the theory of gas transport that are necessary to the forthcoming discussion of the vertical transport model are presented. Second, these basic principles are utilized to characterize two very simple scenarios of subsurface vertical transport of a trace gas. This discussion then leads into the significantly more complex analytical, double-porosity model of gas transport.

2.2.1 Basics of Transport Theory

Of particular importance to the double-porosity model of gas transport is the distinction between the transport mechanisms of diffusion versus advection.

Diffusion refers to the net spread of particles from regions of higher concentration to regions of lower concentration as a result of random particle motions. Defining $C = C(\mathbf{x})$ as the concentration of a substance in a system described by the vector coordinates $\mathbf{x}$, and $\mathbf{J}$ the flux of the substance, then the above definition for diffusion can be restated mathematically as

$$\mathbf{J} = -D\nabla C. \tag{2.1}$$

This relation is known as Fick's first law of diffusion. The negative sign in Eq. (2.1) indicates that a positive flux of particles is directed down the concentration gradient. The constant of proportionality, D, is termed the diffusion coefficient, or diffusivity, and accordingly has dimensions in SI units of [m^2/s]. The diffusion coefficient is actually specific to the substance that is diffusing as well as the fluid in which it is located, and is a function of temperature, pressure, and dynamic viscosity (defined below) [26]. Considering the one-dimensional isothermal, isobaric, binary diffusion of one substance i in another j, Eq. (2.1) becomes simply[7]

$$J^i = -D^{ij} \frac{\partial C^i}{\partial x}. \tag{2.2}$$

In a porous medium, the ratio of fluid-filled, void volume V_{void} to the bulk volume V_{bulk} is termed the *porosity*, $\phi = V_{void} / V_{bulk}$. Diffusion through a porous medium is characterized by the bulk properties of the medium in addition to the properties of the fluid which fills the pores. As such, an *effective diffusion coefficient* D_e^{ij} is defined as

$$D_e^{ij} = \frac{\phi}{\tau} D^{ij} \tag{2.3}$$

where τ is a dimensionless parameter called tortuosity, which has no single, agreed-upon definition, but basically is a measure of how "twisty" a curve is [27]. Note also that some sources define the tortuosity as $T = \phi / \tau$. While conventions might differ, the effect of the tortuosity factor is to reduce the diffusivity to account for an increase in path lengths as a result of "obstacles" within a porous medium.

Advection refers to the transport of a substance by a fluid as a result of the bulk motion of the fluid. Here the term fluid is used loosely, but because advection by

[7] Note that the superscripts in Eq. (2.2) are indices rather than exponents; or more accurately they are labels.

definition requires the existence of a *current*, it cannot occur in a solid. One dimensional advection of a fluid through a porous medium is described generally by Darcy's law

$$J = -\frac{k}{\mu}\frac{\partial p}{\partial x}. \tag{2.4}$$

Note that this equation has the same form as Eq. (2.2): the movement of a substance is determined by a pressure gradient in the bulk fluid. The constant of proportionality in this case is determined by the *permeability*, k, and the *dynamic viscosity*, μ. The permeability is a characteristic of a porous medium describing its capability to transmit fluid, and has SI units of [m^2]. Permeability is also commonly given in the literature in terms of millidarcy (mD), equivalent to 10^{-15} m^2. The dynamic viscosity is essentially a measure of a fluid's internal resistance to flow in response to an applied stress, and has SI units of [Pa·s].

Nominal values for the parameters described above are given in Table 2.2, adopted from Nilson et al. (1991), and unless stated otherwise, these values will be assumed throughout the rest of this chapter.

Table 2.2. Values assumed for transport theory parameters.

Parameter	Assumed Value
porosity (in matrix)[8]	$\phi_m =$ 0.1
permeability (of matrix)	$k_m =$ 10^{-15} m^2
tortuosity	$\tau =$ 10
dynamic viscosity (air)	$\mu =$ 2×10^{-5} Pa·s

[8] The '*m*' label here is necessary to distinguish parameters as they apply to the bulk matrix medium from later values as they apply to fractures.

2.2.2 Gas Flow by Diffusion

It has long been known that diffusion alone cannot account for the vertical transport of contaminant gases from deep underground to the surface. As an example, consider the following scenario, which will be utilized and modified in subsequent sections as well. Assume that a gaseous contaminant is distributed underground throughout an area bounded from below at a depth L = 500 m by an impenetrable floor and initially extends upwards a distance L_0 = 300 m as depicted in Figure 2.4.

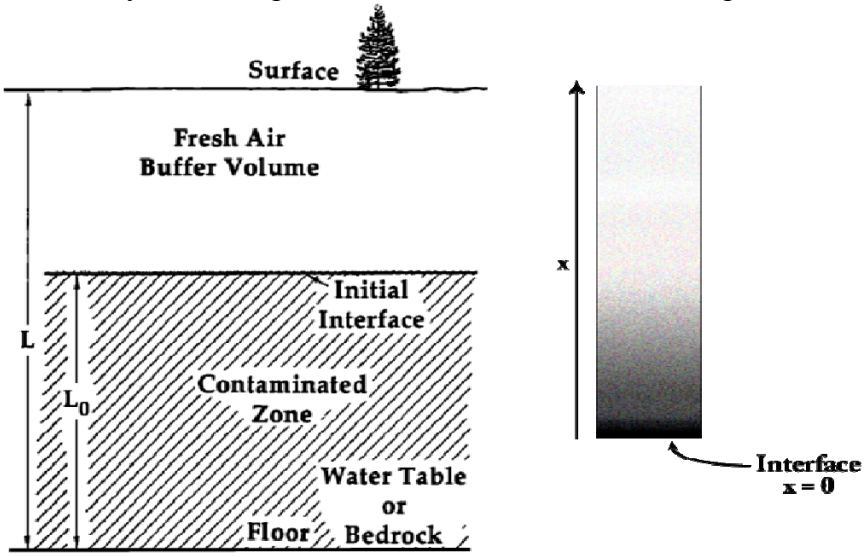

Figure 2.4. Depiction of diffusion transport scenario. Modified from a figure in [24].

Consider one small element of the so-called contamination front, which lies on the initial fresh air-contaminant interface as shown on the right of Figure 2.4. If the contaminated region extends sufficiently far laterally, then the transport of this element can be considered one-dimensional. Discounting adsorption effects, continuity requires that a change in concentration in this element must be due to a flux of contaminant, therefore

$$\frac{\partial C}{\partial t}+\frac{\partial}{\partial x}\left(J\right)=0 \tag{2.5}$$

and upon substitution of Eq. (2.2) for the flux (ignoring the *i* and *j* labels for clarity) this becomes

$$\frac{\partial C(x,t)}{\partial t} = D\frac{\partial^2 C(x,t)}{\partial x^2}. \tag{2.6}$$

Eq. (2.6) is the diffusion equation, the solution of which in this 1D scenario is a quick, easy exercise in the application Laplace transformations. Since the vertical column begins with no concentration inside, the initial condition is $C(x>0,0)=0$. As for boundary conditions, clearly $C(x\to\infty,0)=0$ is one. As for the second, assume that diffusion beneath the interface is sufficient to maintain the concentration at $x=0$ at a constant value $C_0 = C(0,0) = C(0,t)$. Transforming both sides of Eq. (2.6) with respect to time yields.

$$s\overline{C}(x,s) - \underbrace{C(x,0)}_{=0} = D\frac{\partial^2 \overline{C}(x,s)}{\partial x^2}$$

$$\frac{\partial^2 \overline{C}(x,s)}{\partial x^2} = \frac{s}{D}\overline{C}(x,s)$$

$$\overline{C}(x,s) = a_1 e^{\sqrt{\frac{s}{D}}x} + a_2 e^{-\sqrt{\frac{s}{D}}x}.$$

This is the general solution. Based on the first boundary condition above, $a_1 = 0$. The transformed second boundary condition requires that $\overline{C}(0,s) = \int_0^\infty C(0,t)e^{-st}dt = C_0/s$ so

$$\overline{C}(x,s) = \frac{C_0}{s}e^{-\sqrt{\frac{s}{D}}x}$$

the reverse transform of which finally yields

$$C(x,t) = C_0 erfc\left(\frac{x}{\sqrt{4Dt}}\right). \tag{2.7}$$

This result introduces a very important ratio $x/\sqrt{4Dt}$ that is characteristic of solutions to the general diffusion equation. *Erfc* is the complimentary error function, and varies between 1 and 0 as the above ratio varies from 0 to ∞. Since *D* is typically very small, long times *t* are usually required to make the above ratio approach 1 or less. This

introduces the notion of the *characteristic timescale* for the migration of the contaminant front by diffusion given D and a desired depth of transport x, usually written

$$t_D = \frac{x^2}{D}. \tag{2.8}$$

Taking $D(^{133}Xe) = 1.24 \times 10^{-5}\ \mathrm{m^2 \cdot s^{-1}}$, the characteristic time for diffusion of ^{133}Xe up the 200 m separating the interface and surface in Figure 2.4 is $t_D \approx 3.23 \times 10^9 \mathrm{s}$ or 102.3 years! This is much too long of a window for atmospheric monitoring.

2.2.3 Gas Flow in a homogeneous medium

Consider now a simple model of vertical transport of a contaminant in a homogeneous single-porosity medium, driven by atmospheric pumping. The scenario is depicted in Figure 2.5.

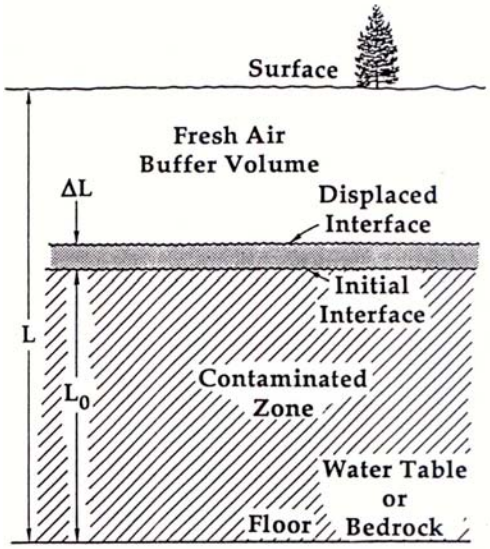

Figure 2.5. Depiction of transport in a homogenous medium by differential volumetric displacement [24].

The flow through this medium is determined by the same parabolic partial differential equation as the diffusion scenario

$$\frac{\partial p}{\partial t} = \alpha \frac{\partial^2 p}{\partial x^2} \tag{2.9}$$

where

$$\alpha = \frac{kp_0}{\mu\phi} \tag{2.10}$$

is known as the bulk pneumatic diffusivity and p_0 is the mean static pressure in the system [28]. If the surface pressure varies harmonically about p_0 with period T and maximum amplitude Δp, and the system is bounded from below by a water table then the pressure at a depth x responds according to Eq. (2.9), the solution of which is given by

$$\frac{p - p_0}{\Delta p} = \frac{\cosh \lambda\sqrt{i}\left(1 - \frac{x}{L}\right)}{\cosh \lambda\sqrt{i}} e^{i\omega t} \tag{2.11}$$

where $\lambda = L\sqrt{\omega/\alpha}$ and $\omega = 2\pi/T$ [28]. If the average static pressure p_0 is taken to be 10^5 Pa, the amplitude of the variation $\Delta p = 2/30\, p_0$, the period T = 200 hours, and the depth to the floor L = 500 m, then using Eq. (2.11) to model the pressure response within the top ten meters of the system yields Figure 2.6.

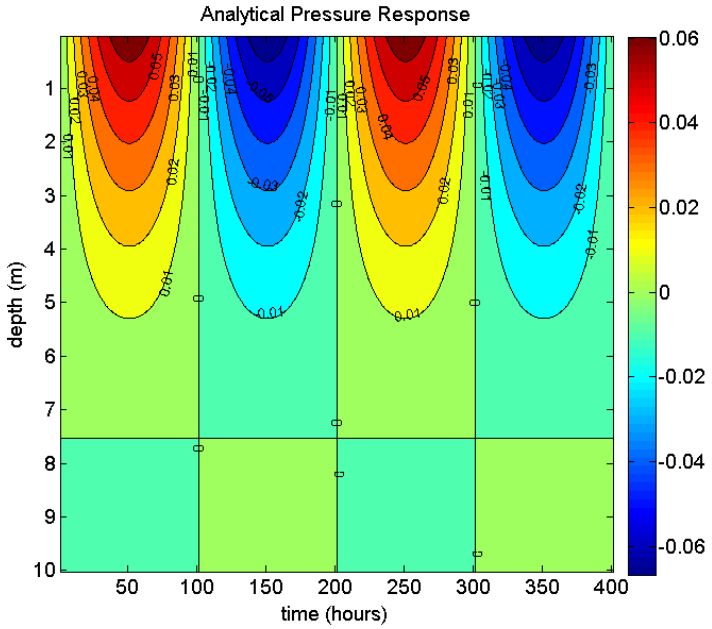

Figure 2.6. The analytical pressure response within the first 10 meters below the surface; given as a fraction of the deviation from the mean static pressure.

Being able to model the underground pressure response to variations in the surface pressure will be an important component to the vertical transport model to be developed. For now, however, assume as a theoretical upper bound that the diffusivity of the porous medium is large enough that the air pressure within the entire system very closely follows any variations at the surface. For isothermal, sinusoidal variations in surface pressure, a piston-like response results in which there is a differential volumetric displacement of the concentration front, as illustrated in Figure 2.5. If L_0 is the depth of contaminant beneath the surface, and *A* the lateral area of the system, then an isothermal change in pressure $\Delta p/p_0$ results in an incremental shift in volume $\Delta V/V_0$, where $V_0 = \phi A L_0$ and accordingly $\Delta V = \phi A \Delta L$. As a result, the differential displacement in concentration front due to an isothermal shift in pressure can be estimated by

$$\frac{\Delta L}{L_0} = \frac{\Delta p}{p_0}. \tag{2.12}$$

A value of $\Delta p = 2/30\, p_0$ as utilized above in Figure 2.6 represents more or less an upper bound variation in surface pressure. Even with this value, for $L_0 = 300$ m of contaminant, the maximum expected displacement of the concentration front would be

$$\Delta L = \frac{\Delta p}{p_0} L_0 = \frac{2}{30}(300 \text{ m}) \approx 20 \text{ m}.$$

Given that the contaminant lies 200 m below the surface, a shift of 20 m during a deep barometric low will never bring contaminant to the surface. Additionally, by this simple model the front will retreat back down once the pressure rises again.

2.2.4 Gas Flow in a fracture embedded in a homogeneous medium

As a last example before considering the double-porosity model on which the vertical transport code is to be based, consider now the same scenario as described in section 2.2.3 but with the addition of a narrow fracture embedded within the otherwise

homogeneous matrix medium. In contrast to the model without the fracture, consider now that the differential volumetric expansion that results from a barometric low is channeled entirely into the narrow fracture. Assuming for now that there is no further seepage of the contaminant from the fracture into the higher matrix levels, then this addition of the fracture to the system leads essentially to an amplification of the expansion.

If the width of the matrix slab between successive fractures is δ_m and the fracture width is δ_f, then by taking a simple ratio of matrix to fracture volumes, Eq. (2.12) now leads to

$$\Delta L = \frac{\Delta p}{p_0} L_0' \frac{\phi_m \delta_m}{\delta_f} . \tag{2.13}$$

Note that the porosity of the fracture, ϕ_f, is taken to be 1, otherwise it too would appear in the denominator. Taking $\delta_m = 2 \text{ m}$, $\delta_f = 0.001 \text{ m}$, then the height by which the contaminant can rise within the fracture is

$$\Delta L = \frac{2}{30}(300 \text{ m}) \frac{(0.1)(1 \text{ m})}{(0.001 \text{ m})} = 2000 \text{ m} .$$

Even much more modest pressure variations of $1/100\, p_0$ would be enough to bring the contaminant up the 200 m to the surface in a single low period.

2.3 DOUBLE-POROSITY MODEL

As a basis for vertical transport of subsurface contaminant, the double-porosity model is a 2D model that is locally 1D and builds upon lessons learned from the simpler models described previously. By *double-porosity* and *1D* it is meant that the model considers gas flow both horizontally in the bulk matrix as well as gas flow vertically within the fractures as driven by pressure responses due to varying surface pressure.

In this section, an analytical outline of the double-porosity model is presented as a foundation for the numerical treatment that it will receive in the next chapter. Beyond facilitating an understanding of the numerical approach, this analytical theory also provides an upper bound estimate of the amount of the outflow possible with barometric pumping as the driving force. A large amount of the following is derived from the work of Nilson et al. 1991 [24].

2.3.1 Overview of the model

Figure 2.7 depicts the scenario as well as the major parameters that influence the double-porosity model. The model considers homogeneous slabs of bulk matrix media, porosity ϕ_m and permeability k_m, embedded with vertical fractures of width δ_f and separated by an average distance δ_m. The contaminating gas is assumed to be distributed uniformly throughout the matrix medium below the interface line. Above the contaminated zone lies an assumedly partially-saturated fresh air buffer zone; saturation effects in this model are presumed to be accounted for in the values of ϕ_m and k_m. Unlike the model presented in section 2.2.4, seepage from the fractures into this buffer region is assumed with the effect being that gas moving upwards along a fracture gets filtered, thus trapping rising contaminant.

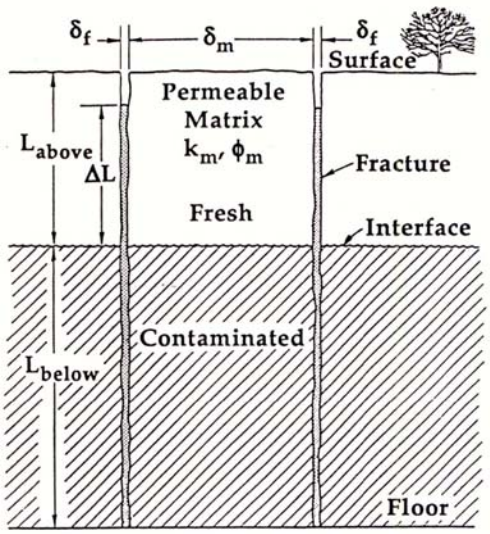

Figure 2.7. Schematic of the double-porosity model [12].

The first objective in this model is to modify Eq. (2.11) to determine the pressure response of the matrix plus fracture system, where before only the matrix was considered. From this, a *breathing efficiency* is derived to describe the amount of gas that "breathes" in and out of the system during a single barometric cycle. Next, the actual contaminant transport within the combined fracture-matrix system is analytically determined based on the harmonically varying flow of fluid induced by the calculated pressure response. As contaminant rises (and falls) within the fractures, seepage into the buffer region results in a generally upward migration of the contaminant front with each cycle. From this a *diffusion-exchange efficiency* is derived to quantify the fraction of gas that flows out. After a number of barometric cycles, a quasi-steady state is established in which the maximum contaminant outflow per cycle is estimated by the overall transport efficiency, a combination of the breathing efficiency and the diffusion-exchange efficiency.

2.3.2 Pressure response of the fracture-matrix system

Pressure within the fracture and matrix individually follow diffusive equations like Eq. (2.9). Because there is an exchange between the two, an additional interaction term must be included. Defining the *x*-direction as decreasing upward along a fracture and the *y*-direction as horizontal into the matrix, the flow of gas within the system is governed by two coupled partial differential equations

$$\begin{aligned} \frac{\partial p}{\partial t} &= \alpha_f \frac{\partial^2 p}{\partial x^2} + \frac{2\phi_m \alpha_m}{\delta_f} \frac{\partial p}{\partial y} && \text{Fracture} \\ \frac{\partial p}{\partial t} &= \alpha_m \frac{\partial^2 p}{\partial y^2} && \text{Matrix} \end{aligned} \quad . \tag{2.14}$$

Parameters α_f and α_m are termed pneumatic diffusivities and relate the speed of pressure waves along the fracture (laminar flow[9]) and within the porous matrix ("Darcian" flow[10]) respectively, defined

$$\alpha_f = \frac{\left(\delta_f\right)^2}{12} \frac{p_0}{\mu} \qquad \text{and} \qquad \alpha_m = \frac{k_m p_0}{\mu \phi_m} . \tag{2.15}$$

For a sinusoidal variation in barometric pressure at the surface, an exact solution to Eq. (2.14) can be found through separation of variables to be the real part of

$$\frac{p - p_0}{\Delta p} = \frac{\cosh \lambda_{fm} \sqrt{i} \left(1 - \frac{x}{L}\right)}{\cosh \lambda_{fm} \sqrt{i}} \frac{\cosh \lambda_m \sqrt{i} \left(1 - \frac{2y}{\delta_m}\right)}{\cosh \lambda_m \sqrt{i}} e^{i\omega t} . \tag{2.16}$$

where $\sqrt{i} = (1+i)/\sqrt{2}$ [24]. The parameters λ_m, λ_f, and λ_{fm} are so-called Fourier numbers defined according to

$$\lambda_m = \frac{\delta_m}{2} \sqrt{\frac{\omega}{\alpha_m}} \qquad \text{and} \qquad \lambda_f = L \sqrt{\frac{\omega}{\alpha_f}} \tag{2.17}$$

$$\lambda_{fm} = \lambda_f \left(1 + \frac{\phi_m \delta_m}{\delta_f} \frac{\tanh \lambda_m \sqrt{i}}{\lambda_m \sqrt{i}}\right)^{1/2} \tag{2.18}$$

[9] Laminar flow can be thought of as smooth flow without obstruction.
[10] Just refers to flow through a porous medium following Darcy's laws.

where L is the total depth from the surface to the impermeable floor.

If the velocity u within the fracture at the surface is given by

$$u = -\frac{\left(\delta_f\right)^2}{12\mu}\frac{\partial p}{\partial x} = \frac{\left(\delta_f\right)^2}{12\mu}\frac{\Delta p}{L}\lambda_{fm}\sqrt{i}\tanh\left(\lambda_{fm}\sqrt{i}\right)e^{i\omega t} \tag{2.19}$$

then the outflow volume of gas that leaves and then reenters the system at the surface each cycle can be calculated from

$$\Delta V = \int_0^{T/2} u dt = \frac{\Delta p}{p_0} L\delta_f \left|\frac{\lambda_{fm}^2}{\lambda_f^2}\frac{\tanh\lambda_{fm}\sqrt{i}}{\lambda_{fm}\sqrt{i}}\right|. \tag{2.20}$$

This result, ΔV, represents the *actual* volumetric outflow in a given cycle. A theoretical *maximum* volumetric outflow is obtained if the pressure response, instead of given by Eq. (2.16), is assumed everywhere to closely follow the barometric variations at the surface. In this upper bound case

$$\Delta V_{\max} = \frac{\Delta p}{p_0}V_0 = \frac{\Delta p}{p_0}L\left(\delta_f + \phi_m\delta_m\right). \tag{2.21}$$

From Eqs. (2.20) and (2.21), the breathing efficiency is defined as the ratio of the actual versus the maximum volumetric outflow per cycle

$$\eta_B = \frac{\Delta V}{\Delta V_{\max}} = \frac{\delta_f}{\delta_f + \phi_m\delta_m}\left|\frac{\lambda_{fm}^2}{\lambda_f^2}\frac{\tanh\lambda_{fm}\sqrt{i}}{\lambda_{fm}\sqrt{i}}\right|. \tag{2.22}$$

Figure 2.8 shows values of the breathing efficiency η_B versus the fracture spacing δ_m for several values of $\alpha_{fm} \equiv L^2\omega/\lambda_{fm}^2$. Note that a sharp knee occurs in each case at around δ_m = 10 m, corresponding roughly to half the *penetration depth* of each pressure wave. For spacing greater than the penetration depth, the efficiency falls off quickly because the inner regions within the matrix slabs are not being reached.

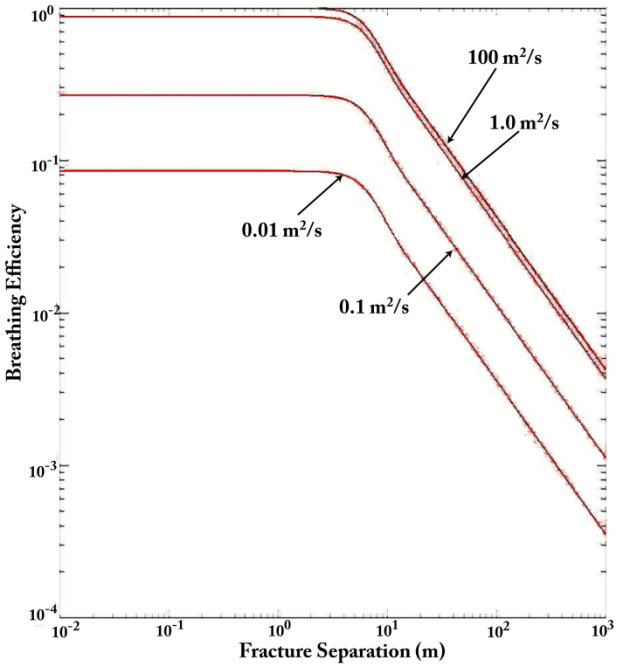

Figure 2.8. Breathing efficiency versus fracture spacing for several values of α_{fm}

2.3.3 Diffusion exchange efficiency

Having derived the efficiency with which barometric pumping leads to the outflow of gas from the system during each cycle, consider now the actual transport of a small quantity of contaminant gas up through a fracture. As contaminant rises (or falls) within the fracture, diffusion drives contaminant through the permeable fracture walls and into the fresh air-filled regions within the buffer region of the matrix. This creates a filtering effect, and ultimately slows down the initial rise of contaminant within the fractures as the concentration gradient extends upward. Figure 2.9 depicts a fracture embedded within a permeable matrix, as well as the diffusion effects.

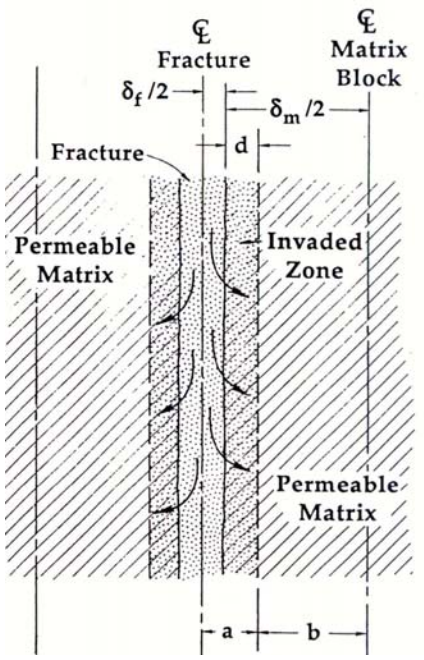

Figure 2.9. Illustration of diffusion exchange between fracture and matrix [24].

The diffusion exchange model of transport depicted in Figure 2.9 is governed by another pair of differential equations not too different from those in the previous section

$$\begin{aligned} &\phi_c \frac{\partial C}{\partial t} + u\frac{\partial C}{\partial x} = \phi_w \frac{D}{a}\frac{\partial C}{\partial y} && \text{Fracture} \\ &\phi_w \frac{\partial C}{\partial t} = \phi_w D \frac{\partial^2 C}{\partial y^2} && \text{Matrix} \end{aligned} \quad . \tag{2.23}$$

The first equation governs advection along the fracture (left side of the equation) as well as diffusion into the matrix (inhomogeneous term on the right). The porosities ϕ_c and ϕ_w describe the porous material filling the channel of half-width a and the wall of thickness b respectively. The depth to which diffusion occurs in the matrix is given by d. Because the channel consists of both fracture and matrix material, the channel porosity is taken as a volume-weighted average

$$\phi_c = \frac{\phi_m d + (\delta_f/2)\phi_f}{d + \delta_f/2} .$$

The wall porosity ϕ_w is simply the matrix porosity ϕ_m. The second equation in (2.23) describes simple diffusion within the matrix. Note that the diffusivity here D is assumed to be the *effective* diffusivity given that diffusion is taking place within a porous medium.

The solution to the coupled differential equations in Eq. (2.23) is far from trivial. If the simplifying assumption that the longitudinal velocity (along the fracture) is harmonic, $u = \mathrm{Re}(u_0 \exp(i\omega t))$ and no bulk motion occurs in the transverse direction, then the problem becomes analogous to the heat transfer problem investigated by Chatwin (1975) and Kurweg (1985) [29], [30]. Rather than look for a general solution, consider a particular solution of the form

$$C = \gamma\left(x + bg\left(y^*\right)e^{i\omega t}\right) \tag{2.24}$$

wherein $y^* \equiv y/b$, and $\gamma \equiv dC/dx$ represents the gradient of the time mean concentration along the fracture. If the gradient along the fracture is assumed to be constant, i.e. $\gamma = C_B / L$ where C_B is the time-averaged concentration at the bottom, then upon substituting Eq. (2.24) back into the matrix portion of Eq. (2.23) the following ordinary differential equation for $g\left(y^*\right)$ is found

$$g'' - i\frac{b^2\omega}{D}g = 0\,. \tag{2.25}$$

This has the solution

$$g\left(y^*\right) = A\cosh\left(\sqrt{i}W\left(1-y^*\right)\right) \tag{2.26}$$

where $W = b\sqrt{\omega/D}$ is known as the Womersley number. Lastly, substitution of Eqs. (2.24) and (2.26) into the fracture portion of Eq. (2.23) and solving for A yields

$$g = \frac{iu_0}{b\omega\phi_c}\left(\frac{W\sqrt{i}}{W\sqrt{i} + \beta\tanh W\sqrt{i}}\right)\frac{\cosh W\sqrt{i}\left(1-y^*\right)}{\cosh W\sqrt{i}} \tag{2.27}$$

where $\beta = b\phi_w / a\phi_c$ is simply the ratio of wall volume to channel volume. With g now determined, plugging Eq. (2.27) back into Eq. (2.24) gives the final expression for the concentration along the fracture at a given time.

The diffusion-exchange efficiency is found by determining the ratio of actual mass outflow in one cycle to the maximum possible outflow. Recall that the velocity of gas was assumed to be harmonic along the fracture, $u = \mathrm{Re}(u_0 \exp(i\omega t))$. Using this, the *actual* mass of contaminant exiting the system in one cycle (period T) is given by the time-integral of the flux of contaminant passing through the upper surface at $x = 0$.

$$\begin{aligned} \Delta M &= -\int_0^T \mathrm{Re}(u)\,\mathrm{Re}(C)\,dt \\ &= -\frac{\gamma u_0^2 T^2}{4\pi\phi_C}\,\mathrm{Re}\left(\frac{iW\sqrt{i}}{W\sqrt{i} + \beta\tanh W\sqrt{i}}\right) \end{aligned} \quad . \tag{2.28}$$

The *maximum* outflow is given by the time-averaged concentration C_B multiplied by the gross outflow per cycle (i.e. no diffusion into the matrix) given by

$$\Delta V = -\int_{T/2}^{T} \mathrm{Re}(u)\,dt = \frac{u_0 T}{\pi} . \tag{2.29}$$

so that

$$\begin{aligned} \eta_D &\equiv \frac{\Delta M}{C_B \Delta V} \\ &= -\frac{\pi}{4}\,\mathrm{Re}\left(\frac{iW\sqrt{i}}{W\sqrt{i} + \beta\tanh W\sqrt{i}}\right) \end{aligned} \quad . \tag{2.30}$$

Figure 2.10 shows a graph of the diffusion-exchange efficiency versus fracture spacing for various values of the pneumatic diffusivity, α_{fm}. Similar to the case of the breathing efficiency, beyond a fracture spacing of 10 m there is no added benefit to the diffusion-exchange efficiency because the pressure wave can only penetrate so far into the matrix.

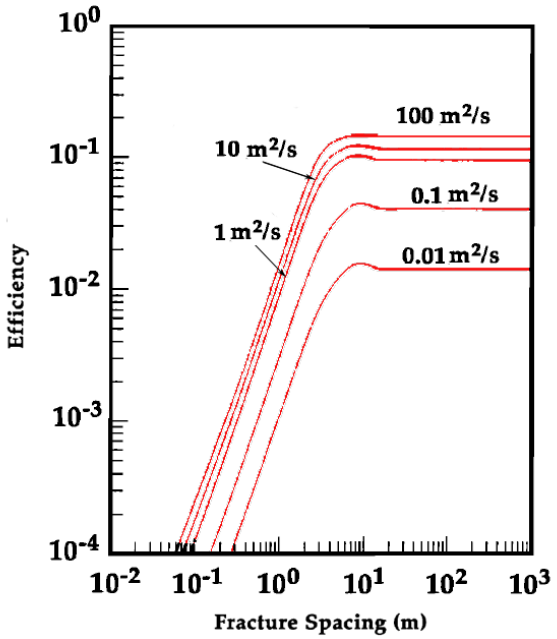

Figure 2.10. Diffusion-exchange efficiency versus fracture spacing for several values of α_{fm}

With both the breathing efficiency η_B and the diffusion-exchange efficiency η_D defined in Eqs. (2.22) and (2.30), the overall transport efficiency is just

$$\eta = \eta_B \eta_D = \left(\frac{\Delta V}{\Delta V_{\max}}\right)\left(\frac{\Delta M}{C_B \Delta V}\right) = \frac{\Delta M}{C_B \Delta V_{\max}} \tag{2.31}$$

Figure 2.11 shows graphs of the overall efficiency versus fracture spacing for several values of α_{fm} using a value of $D = 3\times10^{-6}$ m^2/s. As depicted in the figure, for high pneumatic diffusivities, a maximum overall efficiency of 10% is theoretically possible. If the latter part of Eq. (2.31) is rearranged and the approximation that the initial mass of contaminant is $M_0 = C_B V_0 / 2$ then the fraction of contaminant exiting per cycle can be roughly estimated

$$\frac{\Delta M}{M_0} = 2\eta \frac{\Delta p}{p_0}. \tag{2.32}$$

Taking a maximum overall efficiency of 10% as well as a maximum pressure variation of the order 10%, then Eq. (2.32) suggests a fractional outflow of about 1% per barometric cycle is theoretically possible.

Clearly, as a rigorous mathematical evaluation of a real scenario, Eq. (2.32) and perhaps even the idea of an overall efficiency are lacking. However, as a back-of-the-envelope approximation they serve a great deal to suggest an upper bound theoretical limit for the effectiveness of barometric pumping as a mechanism for subsurface transport. Additionally, within the analytical framework presented here, the governing equations for a numerical vertical transport model have been laid out.

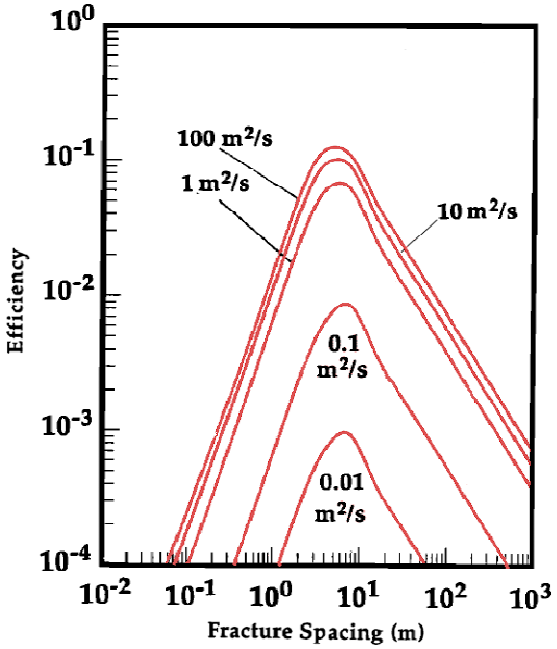

Figure 2.11. Overall efficiency versus fracture spacing for several values of α_{fm}.

Chapter 3: Modeling the Transport

In the preceding chapter, the governing equations for isothermal gas transport in the double-porosity model have been laid out. Though perhaps implied previously but not exactly stated explicitly, the applicability of the double-porosity model is founded on five broad assumptions regarding the system of study [14]:

1. Fracture width is assumed to be much less than the length of the fracture, $\delta_f \ll L$.
2. Complete mixing across the fracture width is assumed.
3. Gas transport within the matrix is assumed to be due mainly to molecular diffusion, i.e. the matrix permeability, $k_m \ll 1$.
4. Fracture transport is assumed to be much faster than matrix transport.
5. Isothermal transport is assumed; heat transfer could also apply

These assumptions combined facilitate the simplification of the model as locally 1D, in that, the two-dimensional system reduces to two coupled, orthogonal 1D systems: vertical transport in the fracture and horizontal transport in the matrix.

An outline for the numerical vertical transport model is as follows. First, the pressure response throughout the system due to variation of the surface pressure will be established. From that, resulting fluid velocities can be calculated. Next, the concentrations of contaminant within the system can be determined through the coupled tracer transport equation, which assumes diffusion and advection along the fracture, orthogonal transfer of mass between the fracture and surrounding matrix blocks, and finally diffusion and advection within the horizontal matrix blocks. Radioactive decay will as well be accounted for throughout the system. Note that because this work is

concerned primarily with the transport of the noble gas xenon, sorption effects are not considered in the model.

Lastly, the introduction of numerical approximation schemes for differential operators in advective transport equations can lead to effects of so-called numerical diffusion. These effects are due largely from the repetitive switching of the periodic "upwind direction" in the calculation. These errors are most dangerous as they accumulate over many cycles. To combat the potential erroneous effects of numerical diffusion, the filtering remedy and methodology (FRAM) originally suggested in a study by Chapman (1981) and extended by Chapman and Waisman (1985) is to be employed and will be explained at length [31], [32]. Additionally, instead of using fracture-matrix flux values to determine mass exchange, evaluation and comparison of the mass storage values between time steps will be used to eliminate potential numerical diffusion effects due to the oscillatory nature of the exchange.

Note that even though much of the framework for what follows has been devised and illustrated previously in the preceding chapter, for the sake of completeness and readability, many equations and definitions are likely to be repeated.

3.1 SETTING UP THE SYSTEM MODEL

An illustration of the system as it will be modeled is given in Figure 3.1. All parameters as utilized in Chapter 2 will be reused here. Specifically, fractures are assumed to have width δ_f and have an air-filled porosity of ϕ_f. Fractures are separated by matrix slabs of thickness δ_m, and are characterized by an air-filled porosity ϕ_m and permeability k_m. Given the symmetry of the system, only one half-slab of matrix and fracture are modeled. A $N \times M$ computational mesh is utilized wherein the positive x-

direction is downwards along the fracture with $i \in [1, N]$ while the positive *y*-direction stretches into the matrix with $j \in [1, M]$.

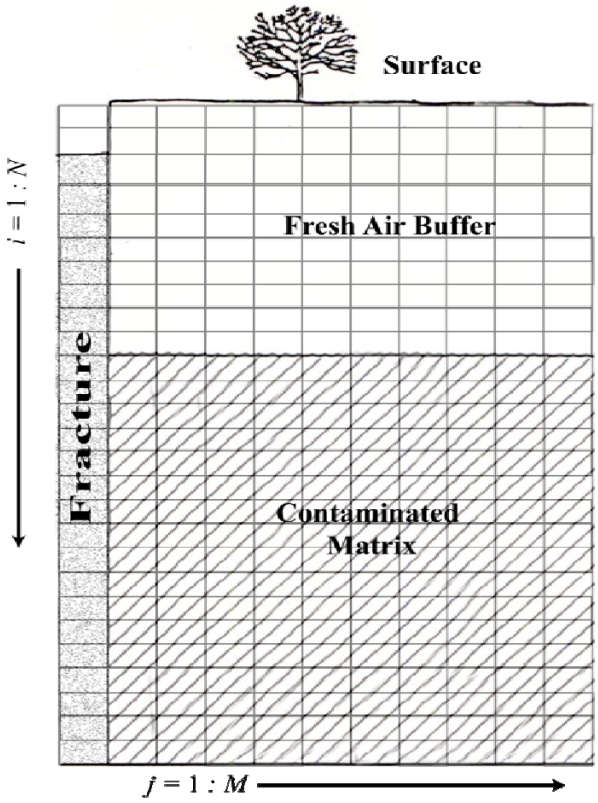

Figure 3.1. Diagram of the numerical system to be modeled.

Throughout this chapter, subscripts *i* and *j* will refer to *x* and *y* cell indices respectively, while superscripts *n* will denote time steps. Cell widths as illustrated in Figure 3.1 will be defined by Δx and Δy and time step duration will be denoted Δt.

3.2 PRESSURE RESPONSE

The first step in any given time step within the execution of the code is to determine from the barometric pressure at the surface, what the subsequent pressure response will be throughout the system. Given the slab-like geometry of the system

model, the isothermal flow of an ideal gas within the 1D system is governed by the coupled pore-fluid diffusion equations [18]

$$\frac{\partial p}{\partial t} = \frac{1}{A}\frac{\partial}{\partial x}\left(\alpha_f A \frac{\partial p}{\partial x}\right) - \underbrace{\frac{\Gamma}{A}\frac{\phi_m}{\phi_f}\int_0^{\delta_m}\frac{\partial p}{\partial t}dy}_{\text{Fracture-Matrix Interaction Term}} \tag{3.1}$$

$$\frac{\partial p}{\partial t} = \frac{\partial}{\partial y}\left(\alpha_m \frac{\partial p}{\partial y}\right) \tag{3.2}$$

wherein A is defined as the cross-sectional area of the fracture and Γ is the fracture-matrix contact area per unit length, which can be assumed for simplicity to satisfy $\Gamma = A$. Again, α_f and α_m are the pore-fluid diffusivities with the fracture and matrix respectively

$$\alpha_f = \frac{\left(\delta_f\right)^2}{12}\frac{p_0}{\mu\phi_f} \qquad \text{and} \qquad \alpha_m = \frac{k_m p_0}{\mu\phi_m}. \tag{3.3}$$

3.2.1 Implicit Diffusion in the Matrix

To account for time (and other first) derivatives, a first-order backwards difference approach will be employed, meaning that

$$\frac{\partial p}{\partial t} \longrightarrow \frac{p_{ij}^{n+1} - p_{ij}^{n}}{\Delta t} \tag{3.4}$$

and second-order diffusive operators will be estimated by second-order centered differencing, for example

$$\frac{\partial^2 p}{\partial x^2} \longrightarrow \frac{p_{i-1j}^{n} - 2p_{ij}^{n} + 2p_{i+1j}^{n}}{\Delta x^2}. \tag{3.5}$$

Of the two governing equations above, Eq. (3.2) can be represented in a fully implicit discretized form. Application of the differencing schemes above to Eq. (3.2) yields the following tridiagonal system of equations

$$\frac{p_{ij}^{n+1} - p_{ij}^{n}}{\Delta t} = \frac{\alpha_m}{\Delta y^2}\left(p_{ij-1}^{n+1} - 2p_{ij}^{n+1} + p_{ij+1}^{n+1}\right) \tag{3.6}$$

Eq. (3.6) is the discretized form of Eq. (3.2), and can be rearranged to give

$$a_j p_{ij-1}^{n+1} + b_j p_{ij}^{n+1} + c_j p_{ij+1}^{n+1} = f_{ij} \tag{3.7}$$

for any horizontal line of fixed *i* where

$$\begin{aligned} a_j &= -\alpha_m \Delta t / \Delta y^2 \\ b_j &= 1 + 2\alpha_m \Delta t / \Delta y^2 \\ c_j &= a_j \\ f_{ij} &= p_{ij}^n \end{aligned} \quad . \tag{3.8}$$

This system of equations is well-known in numerical studies and has a general recursive solution based on the Thomas-algorithm [33]

$$p_{ij}^{n+1} = e_{ij} p_{ij-1}^{n+1} + d_{ij}^{n+1} \tag{3.9}$$

where the solution coefficients are given by

$$\begin{aligned} e_{ij} &= -\frac{a_j}{b_j + c_j e_{ij+1}} \\ d_{ij}^{n+1} &= \frac{f_{ij} - c_j d_{ij+1}^{n+1}}{b_j + c_j e_{ij+1}} \end{aligned} \quad . \tag{3.10}$$

To evaluate e_{ij} and d_{ij}^{n+1}, calculation begins within the matrix and moves towards the fracture; the initial values within matrix block are taken to be

$$\begin{aligned} e_{iM} &= 1 \\ d_{iM}^{n+1} &= 0 \end{aligned} \qquad \forall\ i \in [1, N]\,. \tag{3.11}$$

Additionally, it will prove more convenient to write each p_{ij} in terms of p_{i1}, the instantaneous pressure at the interface between the fracture and the matrix. This can be done by further defining for a fixed *i*

$$p_{ij}^{n+1} = g_{ij} p_{i1}^{n+1} + h_{ij}^{n+1} \tag{3.12}$$

where the coefficients are given recursively for fixed *i* as

$$\begin{aligned} g_{ij} &= g_{ij-1} e_{ij} \\ h_{ij}^{n+1} &= h_{ij-1}^{n+1} e_{ij} + d_{ij}^{n+1} \end{aligned} \tag{3.13}$$

and initial conditions

$$\begin{aligned} g_{i1} &= 1 \\ h_{i1}^{n+1} &= 0 \end{aligned} \qquad \forall\ i \in [1, N]\,. \tag{3.14}$$

Note that in Eqs. (3.9) and (3.12) for each fixed $i \neq 1$ the pressure p_{ij}^{n+1} requires knowledge of p_{i1}^{n+1}, the pressure at the fracture-matrix interface, which itself will depend on the pressure at the surface, p_{11}^{n+1}. In this way, the seepage to/from the matrix is felt in the pressure state of the fracture, thus the need for the fracture-interaction term in Eq. (3.1).

3.2.2 Diffusion and Matrix Interaction within the Fracture

As given by Eq. (3.1), the pressure within the fracture is affected by the diffusion-like response due to the surface pressure as well as seepage from the fracture-matrix interaction. For the interaction term in Eq. (3.1), the following discretization is used

$$\int_0^{\delta_m/2} \frac{\partial p}{\partial t} dy \longrightarrow \sum_{j=1}^{M} \frac{p_{ij}^{n+1} - p_{ij}^{n}}{\Delta t} \Delta y$$

With this substitution, Eq. (3.1) for the fracture (j = 1) becomes

$$\frac{p_{i1}^{n+1} - p_{i1}^{n}}{\Delta t} = \frac{\alpha_f}{\Delta x^2}\left(p_{i-11}^{n+1} - 2p_{i1}^{n+1} + p_{i+11}^{n+1} \right) - \frac{\phi_m}{\phi_f} \sum_{j=1}^{M} \frac{p_{ij}^{n+1} - p_{ij}^{n}}{\Delta t} \Delta y \tag{3.15}$$

The summed-over quantity, for fixed *i,* is just $\partial p / \partial t$ in Eq. (3.2), which is equal to Eq. (3.6).

This leads to another system of fully implicit tridiagonal equations

$$A_i p_{i-11}^{n+1} + B_i p_{i1}^{n+1} + C_i p_{i+11}^{n+1} = F_{i1} \tag{3.16}$$

where

$$\begin{aligned} A_i &= -\alpha_f \frac{\Delta t}{\Delta x^2} \\ B_i &= 1 + 2\alpha_f \frac{\Delta t}{\Delta x^2} + \frac{\phi_m}{\phi_f} \Delta y \sum_{j=1}^{M} g_{ij}^{n+1} \\ C_i &= A_i \\ F_{i1} &= p_{i1}^{n} + p_{i1}^{n} \frac{\phi_m}{\phi_f} \Delta y \sum_{j=1}^{M} g_{ij}^{n} + \frac{\phi_m}{\phi_f} \Delta y \sum_{j=1}^{M} \left(h_{ij}^{n} - h_{ij}^{n+1} \right) \end{aligned} \tag{3.17}$$

The fracture pressures p_{i1}^{n+1} for each *i* can be calculated using the same solution scheme as before; by making an appropriate interchange of *i* and *j* etc. in Eqs. (3.10) and (3.9) , the p_{i1}^{n+1} are recursively determined. With p_{i1}^{n+1} defined for each *i* the final p_{ij}^{n+1} can be calculated from (3.12) as described in the previous section.

3.2.3 Summary of the Numerical Pressure Response Algorithm

For each time step, the following routine is executed

1. For each *i* (horizontal line into matrix):
   Sweep from *j* = M to 1 and calculate e_{ij} and d_{ij}^{n+1} using Eq. (3.10).
   Sweep from *j* = 1 to *M* and calculate g_{ij}^{n+1} and h_{ij}^{n+1} using Eq. (3.13)
2. For each *j* = 1 (along fracture):
   Sweep from *i* = *N* to 1 and calculate e_{i1} and d_{i1}^{n+1} using Eq. (3.10) & (3.17).
   Sweep from *i* = 1 to N and calculate g_{i1}^{n+1} and h_{i1}^{n+1} using Eq. (3.13) & (3.17).
   Sweep from *i* = 1 to N and calculate p_{i1}^{n+1} using Eq. (3.12).
3. For each *i* (horizontal line into matrix):
   Sweep from *j* = 1 to *M* and calculate p_{ij}^{n+1} using Eq. (3.12).

The fluid-flow velocities within the fracture and the matrix are given respectively by

$$u = \frac{\left(\delta_f\right)^2}{12\mu}\frac{\partial p}{\partial x} \qquad \text{and} \qquad v = -\frac{k_m}{\mu}\frac{\partial p}{\partial y} \tag{3.18}$$

With the pressure response throughout the system determined, these velocities can be determined as follows

$$u_i^{n+1} = \frac{\left(\delta_f\right)^2}{12\mu}\frac{p_{i+11}^{n+1} - p_{i-11}^{n+1}}{2\Delta x} \qquad i \in [2, N-1]$$
$$v_{ij}^{n+1} = -\frac{k_m}{\mu}\frac{p_{ij+1}^{n+1} - p_{ij-1}^{n+1}}{2\Delta y} \qquad i, j \in [2, N-1]\times[2, M-1] \tag{3.19}$$

3.3 CONTAMINANT TRANSPORT

3.3.1 Transport Equations

The entire objective of the previous section was the eventual determination of the fluid-flow velocities in Eq. (3.19). With these in-hand for a given time step, the resulting contaminant transport equations can be written and solved by a numerical scheme that turns out to closely mirror that which was employed for the pressure response. Contaminant flow within the fracture and matrix are governed by the following conservation equations

$$\phi_f \frac{\partial C}{\partial t} + \frac{1}{A}\frac{\partial}{\partial x}\left(ACu\right) = -\int_0^{\delta_m/2} \phi_m \frac{\partial p}{\partial t} dy + \frac{1}{A}\frac{\partial}{\partial x}\left(A\phi_f D\frac{\partial C}{\partial x}\right) - \phi_f \lambda C \tag{3.20}$$

$$\phi_m \frac{\partial C}{\partial t} + \frac{\partial}{\partial y}\left(Cv\right) = \frac{\partial}{\partial y}\left(\phi_m D\frac{\partial C}{\partial y}\right) - \phi_m \lambda C \tag{3.21}$$

where λ is the radioactive decay constant for the contaminant gas and the integral represents the instantaneous rate of mass transfer between the fracture and matrix. These equations include from left to right: an advection term driven by the fluid-flow velocities u and v as defined in Eq. (3.18), a fracture-matrix interaction term (in the fracture equation), a diffusion term, and lastly a radioactive decay term. Before moving on to writing down another trigiagonal system of equations, the advective transport will be looked at more closely using the FRAM scheme to minimize potential numerical diffusion error.

3.3.2 FRAM Advection

To counter the spurious oscillations that occur in advection solutions resulting from large velocity gradients, the Filtering Remedy and Methodology (FRAM) developed by Chapman will be used to determine the advection terms in Eqs. (3.20) and (3.21). An outline of this scheme is as follows.

Crowley's so-called second order scheme is first used to calculate provisional values for the concentration by adjusting the advection to counter the leading temporal truncation error that grows large with sharp velocity gradients. Next, to determine acceptable concentration bounds, the local Lagrangian forms of the advective transport equations are solved, and the provisional values for the concentration are filtered to determine if these bounds are exceeded. If the bounds are exceeded then numerical diffusion is artificially introduced to counter the exceeding value. Finally, the advection terms as well as any artificial diffusion terms are added back to the tracer transport equations.

First a provisional value for the concentration is estimated using the 1D advection equation

$$\frac{\partial C}{\partial t} + u\frac{\partial C}{\partial x} = 0 \tag{3.22}$$

which in discretized form becomes

$$\frac{C_{ij}^{n+1} - C_{ij}^{n}}{\Delta t} + \frac{u}{2}\left(\frac{C_{i+1j}^{n} - C_{i-1j}^{n}}{\Delta x}\right) = 0\,. \tag{3.23}$$

To account for the error introduced by the leading term in the truncated error, an artificial diffusion term is introduced on the right side

$$\frac{C_{ij}^{n+1} - C_{ij}^{n}}{\Delta t} + \frac{u}{2}\left(\frac{C_{i+1j}^{n} - C_{i-1j}^{n}}{\Delta x}\right) = \frac{\partial}{\partial x}F \tag{3.24}$$

where

$$F = \varepsilon \frac{\partial C}{\partial x} \quad . \tag{3.25}$$

Following the recommendation of Hirt (1968) [34], the diffusion is made large enough to counter the oscillations by letting

$$\varepsilon = \frac{u\Delta x}{2} - \frac{u^2 \Delta t}{2}. \tag{3.26}$$

By including Eqs. (3.26) and (3.25) in Eq. (3.24) and solving for the *provisional* concentration, $C_{ij}^{n+1} \to \tilde{C}_{ij}^{n+1}$, the result is

$$\tilde{C}_{ij}^{n+1} = C_{ij}^{n} - \frac{u\Delta t}{2}\left(\frac{C_{i+1j}^{n} - C_{i-1j}^{n}}{\Delta x} \right) + \frac{u^2 \Delta t^2}{2\Delta x^2}\left(C_{i+1j}^{n} - 2C_{ij}^{n} + C_{i-1j}^{n} \right) \tag{3.27}$$

In areas of the mesh where $u\Delta t / \Delta x < 1$, Eq. (3.27) is enough to stabilize the advection solution. However, in regions of particularly high pressure gradients, additional dissipation ε must be added. Consider now the Lagrangian equation for *C* or rather the flux, *uC*

$$\frac{d}{dt}\left(C \right) + C\frac{\partial u}{\partial x} = 0 \tag{3.28}$$

from which

$$C_{ij}^{*} = C_{ij}^{n} - C_{ij}^{n}\left(\frac{u_{i+1j}^{n} - u_{i-1j}^{n}}{2\Delta x} \right)\Delta t \,. \tag{3.29}$$

Eq. (3.29) essentially says that the upper bound C_{ij}^{*} is represented by a pure translation $u\Delta t$ of the previous time concentration.

Now a filtering scheme can be established for the provisional concentration $\tilde{C}_{ij}^{n+1}$ by defining the minimum and maximum acceptable values for the provisional concentration by

$$\begin{aligned} C_{ij}^{-} &= \min\left(C_{i-1j}^{*}, C_{ij}^{*}, C_{i+1j}^{*} \right) \\ C_{ij}^{+} &= \max\left(C_{i-1j}^{*}, C_{ij}^{*}, C_{i+1j}^{*} \right) \end{aligned} \quad . \tag{3.30}$$

If the provisional concentration $\tilde{C}_{ij}^{n+1}$ does not fall between these two values, then an additional artificial diffusive step ε is added. If a "gate" parameter is defined as

$$\chi_{ij} = \begin{cases} 0 & C_{ij}^{-} \le \tilde{C}_{ij}^{n+1} \le C_{ij}^{+} \\ 1 & \text{otherwise} \end{cases} \tag{3.31}$$

then the diffusive step can be written

$$\varepsilon_{ij} = \chi_{ij}\left(\frac{\left|u_{ij}^{n}\right|\Delta x}{2} - \frac{\left(u_{ij}^{n}\right)^{2}\Delta t}{2}\right) \rightarrow \varepsilon_{i\pm 1/2\,j} = \chi_{ij}\frac{\left|u_{ij}^{n}\right|\Delta x}{2}\left(1 \pm \frac{u_{ij}^{n}\Delta t}{\Delta x}\right). \tag{3.32}$$

The final filtered advection term then becomes

$$C_{ij}^{n+1} = \tilde{C}_{ij}^{n+1} + \frac{\Delta t}{\Delta x^{2}}\left[\varepsilon_{i+1/2\,j}\left(C_{i+1\,j}^{n} - C_{ij}^{n}\right) - \varepsilon_{i-1/2\,j}\left(C_{ij}^{n} - C_{i-1\,j}^{n}\right)\right] \tag{3.33}$$

3.3.3 Final Solution Scheme

Upon writing out all of the discretized terms in Eq. (3.20), with the addition of the filtered advective term in Eq. (3.33) , the following expansion results

$$\begin{aligned} C_{i1}^{n+1} = C_{i1}^{n} &+ \underbrace{\frac{D\Delta t}{\Delta x^{2}}\left(C_{i+11}^{n+1} - 2C_{i1}^{n+1} + C_{i-11}^{n+1}\right)}_{Diffusion} - \underbrace{\frac{u\Delta t}{2\Delta x}\left(C_{i-11}^{n} - C_{i+11}^{n}\right)}_{Advection} + \underbrace{\frac{u^{2}\Delta t^{2}}{2\Delta x^{2}}\left(C_{i-11}^{n} - 2C_{i1}^{n} + C_{i+11}^{n}\right)}_{Stabilized\ Advection} \\ &+ \underbrace{\frac{\Delta t}{\Delta x^{2}}\left[\varepsilon_{i+1/2}\left(C_{i+11}^{n} - C_{i1}^{n}\right) - \varepsilon_{i-1/2}\left(C_{i1}^{n} - C_{i-11}^{n}\right)\right]}_{Oscillations\ Filtered} + \underbrace{\frac{\phi_{m}}{\phi_{f}}\sum_{j=1}^{M}\left(C_{ij}^{n+1} - C_{ij}^{n}\right)\Delta y}_{Fracture-Matrix\ Interaction} - \underbrace{\lambda C_{i1}^{n}}_{\substack{Radioactive \\ Decay}} \end{aligned} \tag{3.34}$$

To turn this into a fully-implicit scheme, the fracture-matrix interaction term must be rewritten using the substitution

$$\begin{aligned} \sum_{j=1}^{M} C_{ij}^{n+1} &= \sum_{j=1}^{M}\left(g_{ij}^{n+1}C_{i1}^{n+1} + h_{ij}^{n+1}\right) \\ &= C_{i1}^{n+1}\sum_{j=1}^{M} g_{ij}^{n+1} + \sum_{j=1}^{M} h_{ij}^{n+1} \end{aligned} \tag{3.35}$$

The final solution scheme is again the fully implicit tridiagonal form

$$A_i C_{i-11}^{n+1} + B_i C_{i1}^{n+1} + C_i C_{i+11}^{n+1} = F_{i1} \tag{3.36}$$

with solution as described for the pressure response, where

$$\begin{aligned} A_i &= -D\frac{\Delta t}{\Delta x^2} \\ B_i &= 1 + 2D\frac{\Delta t}{\Delta x^2} - \Delta y \frac{\phi_m}{\phi_f}\sum_{j=1}^{M} g_{ij}^{n+1} \\ C_i &= A_i \\ F_i &= C_{i1}^n - \lambda C_{i1}^n - C_{i1}^n \Delta y \frac{\phi_m}{\phi_f}\sum_{j=1}^{M} g_{ij}^n - \Delta y \frac{\phi_m}{\phi_f}\sum_{j=1}^{M}\left(h_{ij}^n - h_{ij}^{n+1}\right) + Advection\ Terms \end{aligned} \tag{3.37}$$

Solution for the matrix is just the same, but without fracture-matrix interaction term:

$$\begin{aligned} a_j &= -D\frac{\Delta t}{\Delta y^2} \\ b_j &= 1 + 2D\frac{\Delta t}{\Delta y^2} \\ c_j &= a_j \\ f_{ij} &= C_{ij}^n - \lambda C_{ij}^n + Advection\ Terms \end{aligned} \tag{3.38}$$

Chapter 4: Results and Discussion

4.1 SOURCE TERM RESULTS

With a working compilation of MONTEBURNS, MCNP, and ORIGEN 2.2 and the major parameters set as described in section 2.1, running a source term calculation is as easy as executing the MONTEBURNS script and waiting for the computation to finish. Examples of MCNP and MONTEBURNS input decks are shown in A.3 and A.4 of the Appendix. Upon completion of a burn run, MONTEBURNS outputs a number of files, including summaries of neutron histories, particle interactions by type, as well as ORIGEN output tapes consisting of the material compositions in each cell of the system geometry.

4.1.1 Diagnostics

The first step in the source term calculation was to simply test the implementation on the fission core and then test it with the addition of a thin shell of surrounding geologic media to determine whether the model depicts the neutron physics that are expected. Immediately noticeable in the calculation was that even though no neutron source was present in the geologic medium, the addition of the surrounding medium produced a definite alteration in the neutron flux profile within the fission core. The reason for this is obvious; due to inelastic scattering events in the surrounding geologic medium, a certain fraction of neutrons are reflected back into the core where they add to the overall neutron flux.

To get an idea of the magnitude of these effects, a simple analysis of the neutron flux profile was conducted, the results of which are summarized in Table 4.1 and Figure 4.1. In order to determine the number of neutrons passing first out of the core and then back into the core upon reflection, a *flag* within MCNP was set up to flag neutrons that

pass the core's surface from the positive (rock) side to the negative (core) side. As seen below, neutron reflection contributes a significant fraction of the neutron flux within the core; by 50 cm of rock thickness, 20% of the neutrons contributing to the total neutron flux in the core are flagged as having passed from the rock to the core cells. This neutron reflection contributes to an increase in the overall k_{eff} of the fission core as shown in Table 4.1.

Table 4.1. Neutron flux profile of HEU fissioning core with various thicknesses of surrounding Wedepohl rock.

Rock thickness	k_{eff}	*n* flux from core alone	*n* flux coming from rock
1cm	1.035	0.9491	0.0509
10cm	1.140	0.8442	0.1558
50cm	1.252	0.7972	0.2028
100cm	1.226	0.7947	0.2053

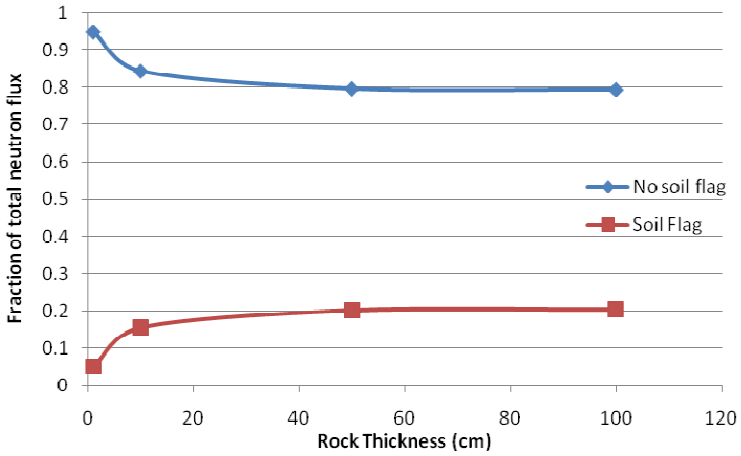

Figure 4.1. Fraction of neutrons in HEU fissioning core flagged and non-flagged as coming from the surrounding medium

In addition to contributing to the overall neutron flux, the reflected neutrons also significantly alter the energy flux spectrum within the core, as demonstrated by the data in Table 4.2. Neutrons that undergo inelastic collisions with nuclei of the surrounding rock also lose energy along their path. As the rock thickness surrounding the fissioning core increases, neutrons penetrate deeper into the rock and lose increasing amounts of energy. The result is that reflected neutrons in the core have a lower average energy. The explosion model indeed seems to accurately depict the expected scenario.

Table 4.2. HEU core neutron energy flux profile for various thicknesses of Wedepohl rock

Rock Thickness(cm)	% flux by energy range		
	Thermal	Intermediate	Fast
0	0	5.39	94.61
1	0	5.54	94.46
10	0	7.02	92.98
25	0	9.92	90.08
50	0.14	12.44	87.42
100	0.34	12.90	86.76

Of secondary importance in Figure 4.1 and Table 4.1 is the asymptotic nature of the variation of neutron flux characteristics and k_{eff} with increasing thickness of surrounding rock. For the Wedepohl rock composition used in those analyses, beyond an outer thickness of 80-100 cm, additional amounts of rock media have negligible effect on the physics within the fissioning core. As stated in Section 2.1.3, the explosion model should include a geologic media of thickness, R, such that a suitably small fraction of the system neutrons escape into the outer vacuum cell. Given that 80-100 cm thickness is enough to account for all neutrons capable of transporting from the nucleus out into the

surrounding rock, and then back into the core, it seems reasonable to guess that a neutron's effective range within a time of 1 μs is about 160-200 cm.

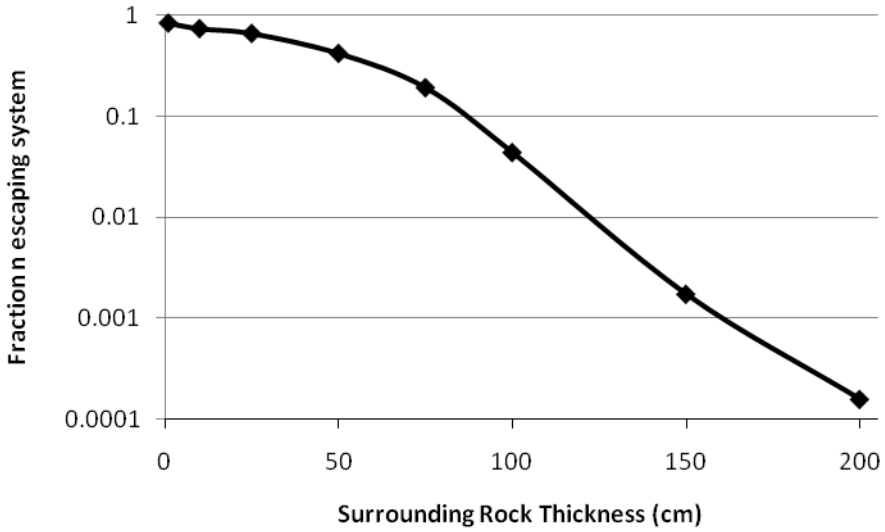

Figure 4.2. Fraction of *n* escaping the system for various thicknesses of Wedepohl rock surrounding HEU core

Figure 4.2 shows the results of a simple MCNP analysis of the fraction of neutrons that are lost through escape into the outer vacuum as the thickness of surrounding rock is increased. Again, the Wedepohl rock composition was utilized surrounding a HEU fission core. As depicted in the figure, the neutron escape fraction drops below 1% around R = 125 cm, below 0.1% around 160 cm, and approaches 0.01% by 200 cm. The particular value that constitutes a "suitably small" escape fraction is somewhat arbitrary; the runtime of a MONTEBURNS burn source term calculation involving a fissioning core and 200 cm thickness of surrounding geologic medium was of the order 12 hours on an Intel® Core™ 2 Duo CPU computer, a length of time deemed long enough to devote to a single calculation. As such, an R = 2 m was taken for the thickness of geologic media for all source term calculations. Given that the five

compositions studied have some variation, particularly in their hydrogen and iron content, 200 cm of thickness assured that all source term calculations yielded neutron escape fractions of below 0.1%.

4.1.2 Source Term Calculation Results

With the input parameters verified and set, calculation of the source term was just a matter of patience while letting the numerical model process. The output of most interest from a burn run of MONTEBURNS is a final inventory of nuclide concentrations within the system. These concentrations represent the initial state of the system immediately following the detonation of the underground fission device, assuming one of the five geologic compositions listed in A.2. To determine the time-varying source term, this initial inventory was easily fed into ORIGEN 2.2 and decayed for various lengths of time to obtain a database of radionuclide inventories at various times following the detonation. Tables 4.3 and 4.4 provide a snapshot of the source terms of some of the most pertinent radionuclides.

Table 4.3. Activities in Ci of Xe radioisotopes following modeled 1 kton explosion at various post-burn decay times, assuming both uranium and plutonium cores.

		Initial	1 hr	10 hr	1 day	10 days	30 days	100 days
Uranium Core	^{131m}Xe	1.361E-01	7.948E-01	2.386E+01	5.972E+01	3.555E+02	2.638E+02	7.439E+00
	^{133}Xe	1.964E+02	6.481E+03	8.824E+04	1.709E+05	1.127E+05	8.120E+03	7.805E-01
	^{133m}Xe	1.560E+03	1.984E+03	7.379E+03	1.208E+04	1.743E+03	3.122E+00	7.441E-10
	^{135}Xe	1.109E+05	6.651E+05	2.000E+06	1.329E+06	1.843E-01	2.334E-17	0.000E+00
Plutonium Core	^{131m}Xe	1.811E-01	9.736E-01	2.705E+01	6.791E+01	4.147E+02	3.094E+02	8.740E+00
	^{133}Xe	6.991E+02	7.171E+03	8.886E+04	1.717E+05	1.134E+05	8.178E+03	7.861E-01
	^{133m}Xe	5.446E+03	5.831E+03	1.078E+04	1.490E+04	1.906E+03	3.425E+00	8.163E-10
	^{135}Xe	2.648E+05	9.930E+05	2.269E+06	1.459E+06	1.988E-01	2.518E-17	0.000E+00

Table 4.4 Activities of ^{37}Ar in Ci resulting from modeled 1 kton explosion and subsequent neutron activation in 2m of various surrounding soil and rock compositions.

		Initial	10 hr	1 day	10 days	30 days	100 days
Uranium Core	Wedepohl	1.014E+03	1.005E+03	9.937E+02	8.316E+02	5.597E+02	1.401E+02
	Taylor	9.455E+02	9.377E+02	9.270E+02	7.757E+02	5.222E+02	1.307E+02
	Mason	4.616E+02	4.579E+02	4.526E+02	3.788E+02	2.549E+02	6.380E+01
	Bowen	3.488E+02	3.460E+02	3.420E+02	2.862E+02	1.926E+02	4.820E+01
	Vinogradov	3.477E+02	3.448E+02	3.409E+02	2.853E+02	1.920E+02	4.805E+01
Plutonium Core	Wedepohl	1.760E+03	1.745E+03	1.725E+03	1.444E+03	9.717E+02	2.432E+02
	Taylor	1.502E+03	1.489E+03	1.472E+03	1.232E+03	8.294E+02	2.075E+02
	Mason	7.241E+02	7.182E+02	7.100E+02	5.941E+02	3.999E+02	1.001E+02
	Bowen	5.021E+02	4.980E+02	4.922E+02	4.119E+02	2.773E+02	6.938E+01
	Vinogradov	5.011E+02	4.970E+02	4.913E+02	4.111E+02	2.767E+02	6.925E+01

While ORIGEN 2.2 decay is perfectly sufficient to determine these inventories at any time desired, this strategy grows prohibitively cumbersome in the construction of decay cards and the extraction of data for, say, 10,000 time intervals, as will be necessary for use in the vertical transport code. To really make use of these data in the vertical transport code, an analytical source term was derived, for which an understanding of the physics behind the source term time evolution is necessary.

Figures 4.3, 4.4, and 4.5 show the decay chains of ^{131}Xe, ^{133}Xe, and ^{135}Xe respectively and Table 4.5 provides ORIGEN 2.2 generated activity levels for the relevant radionuclides at several times. Even following the detonation, new radioxenon is continually produced from the decay of its parent radionuclides. As an example, consider the decay chain of ^{135}Xe as shown in Figure 4.5. An analytical source term calculation for ^{135}Xe is relatively simple because in this case the first three parent radionuclides have half-lives of less than 20 seconds – within a few minutes, and certainly within an hour, nearly all of these short-lived parents have decayed away.

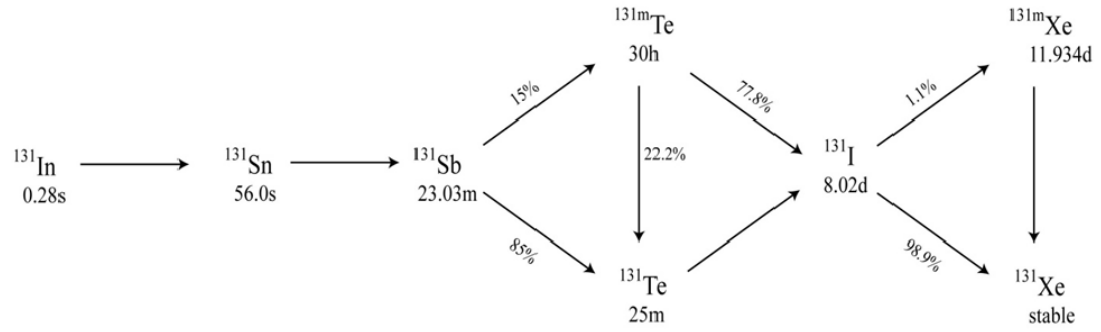

Figure 4.3. The decay chain of ^{131}Xe and its parent radionuclides.

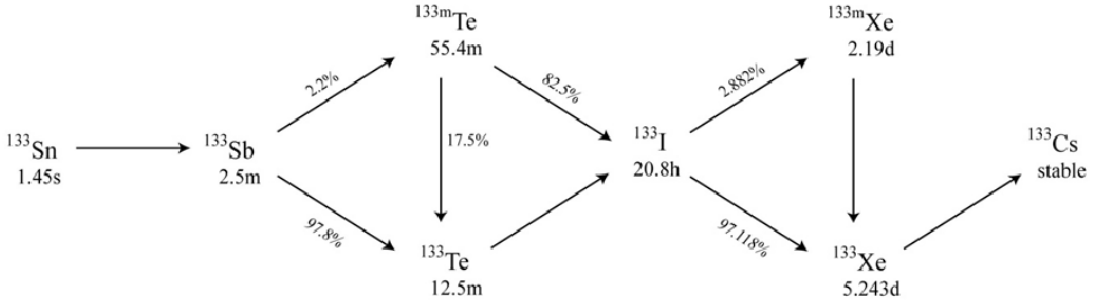

Figure 4.4. The decay chain of ^{133}Xe and its parent radionuclides.

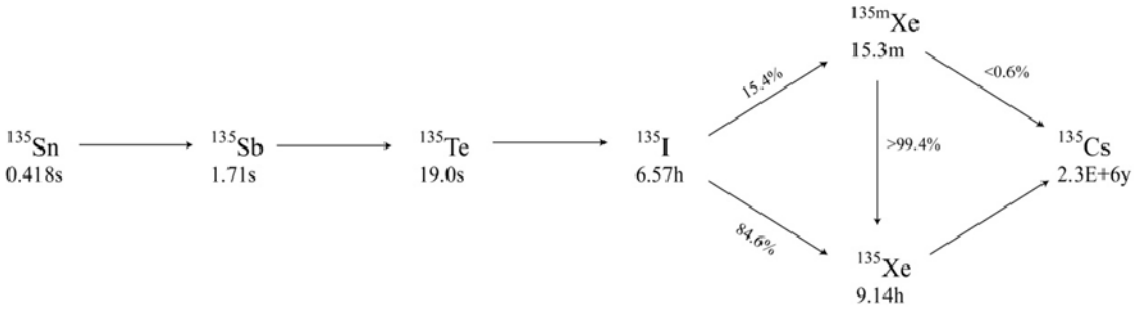

Figure 4.5. The decay chain of ^{135}Xe and its parent radionuclides.

Table 4.5. Activities in Ci of radioxenon and parent radionuclides resulting from 1 kton HEU fission core detonation.

	INITIAL	15.0MI	1.0HR	3.0HR	10.0HR	1.0D	10.0D	100.0D
IN131	2.899E+09	0.000E+00	0.000E+00	0.000E+00	0.000E+00	0.000E+00	0.000E+00	0.000E+00
SN131	4.655E+08	2.400E+04	3.013E-09	0.000E+00	0.000E+00	0.000E+00	0.000E+00	0.000E+00
SB131	2.832E+07	3.257E+07	8.392E+06	2.256E+05	7.181E-01	7.279E-12	0.000E+00	0.000E+00
TE131	3.181E+06	1.434E+07	1.444E+07	1.348E+06	1.636E+04	1.182E+04	8.041E+01	1.703E-20
TE131M	4.729E+04	6.224E+04	8.196E+04	8.511E+04	7.257E+04	5.252E+04	3.572E+02	7.563E-20
I131	3.426E+02	8.821E+03	5.349E+04	9.689E+04	9.966E+04	9.782E+04	4.942E+04	2.115E+01
XE131M	1.361E-01	1.611E-01	7.948E-01	5.252E+00	2.386E+01	5.972E+01	3.555E+02	7.439E+00
IN131	2.899E+09	0.000E+00	0.000E+00	0.000E+00	0.000E+00	0.000E+00	0.000E+00	0.000E+00
SN133	2.967E+09	0.000E+00	0.000E+00	0.000E+00	0.000E+00	0.000E+00	0.000E+00	0.000E+00
SB133	3.431E+08	4.911E+06	1.114E+01	9.895E-15	0.000E+00	0.000E+00	0.000E+00	0.000E+00
TE133	6.012E+07	6.384E+07	6.361E+06	2.809E+05	1.433E+03	3.908E-02	0.000E+00	0.000E+00
TE133M	1.519E+07	1.289E+07	7.345E+06	1.637E+06	8.547E+03	2.330E-01	0.000E+00	0.000E+00
I133	6.203E+04	8.789E+05	1.675E+06	1.868E+06	1.541E+06	9.669E+05	7.233E+02	0.000E+00
I133M	3.895E+08	3.072E-22	0.000E+00	0.000E+00	0.000E+00	0.000E+00	0.000E+00	0.000E+00
XE133	1.964E+02	8.739E+02	6.481E+03	2.582E+04	8.824E+04	1.709E+05	1.127E+05	7.805E-01
XE133M	1.560E+03	1.603E+03	1.984E+03	3.300E+03	7.379E+03	1.208E+04	1.743E+03	7.441E-10
SN135	1.213E+08	0.000E+00	0.000E+00	0.000E+00	0.000E+00	0.000E+00	0.000E+00	0.000E+00
SB135	2.638E+09	0.000E+00	0.000E+00	0.000E+00	0.000E+00	0.000E+00	0.000E+00	0.000E+00
TE135	4.114E+09	3.372E-05	0.000E+00	0.000E+00	0.000E+00	0.000E+00	0.000E+00	0.000E+00
I135	2.519E+06	5.869E+06	5.425E+06	4.399E+06	2.111E+06	4.865E+05	7.108E-05	0.000E+00
XE135	1.109E+05	2.990E+05	6.651E+05	1.275E+06	2.000E+06	1.329E+06	1.843E-01	0.000E+00
XE135M	6.606E+06	3.798E+06	1.241E+06	7.062E+05	3.382E+05	7.793E+04	1.139E-05	0.000E+00

As a result, assuming the dissipation of short-lived parent radionuclides, the differential equations summarizing the inventories of the rest of the decay chain, ^{135}I, ^{135m}Xe, and ^{135}Xe, can be written

$$\frac{dN_{I135}}{dt} = -\lambda_{I135} N_{I135}$$

$$\frac{dN_{Xe135m}}{dt} = 0.15\lambda_{I135} N_{I135} - \lambda_{Xe135m} N_{Xe135m}$$

$$\frac{dN_{Xe135}}{dt} = 0.846\lambda_{I135} N_{I135} + 0.994\lambda_{Xe135m} N_{Xe135m} - \lambda_{Xe135} N_{Xe135}$$

Solving this system of differential equations for N_{Xe135} as a function of time gives the amount of ^{135}Xe at all times. Laplace transforming this system leads to

$$\begin{aligned} sN_{I135}(s) - N_{I135}(0) &= -\lambda_{I135} N_{I135}(s) \\ sN_{Xe135m}(s) - N_{Xe135m}(0) &= 0.15\lambda_{I135} N_{I135}(s) - \lambda_{Xe135m} N_{Xe135m}(s) \\ sN_{Xe135}(s) - N_{Xe135}(0) &= 0.846\lambda_{I135} N_{I135}(s) + 0.994\lambda_{Xe135m} N_{Xe135m}(s) - \lambda_{Xe135} N_{Xe135}(s) \end{aligned} \quad (3.39)$$

The first equation of Eq. (3.39) is easily solvable to yield

$$N_{I135}(s) = \frac{N_{I135}(0)}{s+\lambda_{I135}} \quad \rightarrow \quad N_{I135}(t) = N_{I135}(0)e^{-\lambda_{I135}t}. \tag{3.40}$$

Now Eq. (3.40) is substituted into the second equation of Eq. (3.39) to arrive at

$$N_{Xe135m}(s) = \frac{N_{Xe135m}(0)}{\left(s+\lambda_{Xe135m}\right)} + \frac{0.15\lambda_{I135}N_{I135}(0)}{\left(s+\lambda_{Xe135m}\right)\left(s+\lambda_{I135}\right)} \tag{3.41}$$

the solution to which is

$$N_{Xe135m}(t) = N_{Xe135m}(0)e^{-\lambda_{Xe135m}t} + \frac{0.15\lambda_{I135}N_{I135}(0)}{\left(\lambda_{I135}-\lambda_{Xe135m}\right)}\left[e^{-\lambda_{Xe135m}t} - e^{-\lambda_{I135}t}\right]. \tag{3.42}$$

Lastly, using Eq. (3.41), the third equation of (3.39) can be expressed as

$$N_{Xe135}(s) = \frac{N_{Xe135}(0)}{\left(s+\lambda_{Xe135}\right)} + \frac{0.846\lambda_{I135}N_{I135}(0)}{\left(s+\lambda_{Xe135}\right)\left(s+\lambda_{I135}\right)} + \frac{0.994\lambda_{Xe135m}N_{Xe135m}(0)}{\left(s+\lambda_{Xe135}\right)\left(s+\lambda_{Xe135m}\right)} + \ldots$$
$$\frac{(0.994)(0.15)\lambda_{Xe135m}\lambda_{I135}N_{I135}(0)}{\left(s+\lambda_{Xe135}\right)\left(s+\lambda_{Xe135m}\right)\left(s+\lambda_{I135}\right)},$$

the reverse transform of which is

$$\begin{aligned} N_{Xe135}(t) = {} & N_{Xe135}(0)e^{-\lambda_{Xe135}t} + \frac{0.846\lambda_{I135}N_{I135}(0)}{\left(\lambda_{I135}-\lambda_{Xe135}\right)}\left[e^{-\lambda_{Xe135}t} - e^{-\lambda_{I135}t}\right] + \ldots \\ & \frac{0.994\lambda_{Xe135m}N_{Xe135m}(0)}{\left(\lambda_{Xe135m}-\lambda_{Xe135}\right)}\left[e^{-\lambda_{Xe135}t} - e^{-\lambda_{Xe135m}t}\right] + \ldots \\ & (0.994)(0.15)\lambda_{Xe135m}\lambda_{I135}N_{I135}(0)\left[\frac{e^{-\lambda_{Xe135}t}}{\left(\lambda_{Xe135m}-\lambda_{Xe135}\right)\left(\lambda_{I135}-\lambda_{Xe135}\right)} + \ldots\right. \\ & \left.\frac{e^{-\lambda_{Xe135m}t}}{\left(\lambda_{Xe135}-\lambda_{Xe135m}\right)\left(\lambda_{I135}-\lambda_{Xe135m}\right)} + \frac{e^{-\lambda_{I135}t}}{\left(\lambda_{Xe135}-\lambda_{I135}\right)\left(\lambda_{Xe135m}-\lambda_{I135}\right)}\right] \end{aligned} \tag{3.43}$$

Upon rewriting in terms of activity through the relation $A = \lambda N$, Eq. (3.43) gives the exact, analytical solution to the activity ^{135}Xe for all time t given the initial activities. The iterative nature of this solution process should be quite evident; the corresponding solutions for ^{131m}Xe and ^{133}Xe are significantly longer because of the necessary inclusion of additional parent nuclides whose half-lives are too long to neglect.

The full MATLAB code for the analytical source term calculation given initial activities as provided by MONTEBURNS is included in A.5 of the Appendix. This code calculates the radioxenon inventories at specified time steps, as well as estimates the amount of new radionuclides produced at each time step, for subsequent use in the vertical transport code. The source term for ^{131m}Xe, ^{133m}Xe, ^{133}Xe, and ^{135}Xe carried out to 100 days following the initial detonation of the HEU core is shown in Figure 4.6.

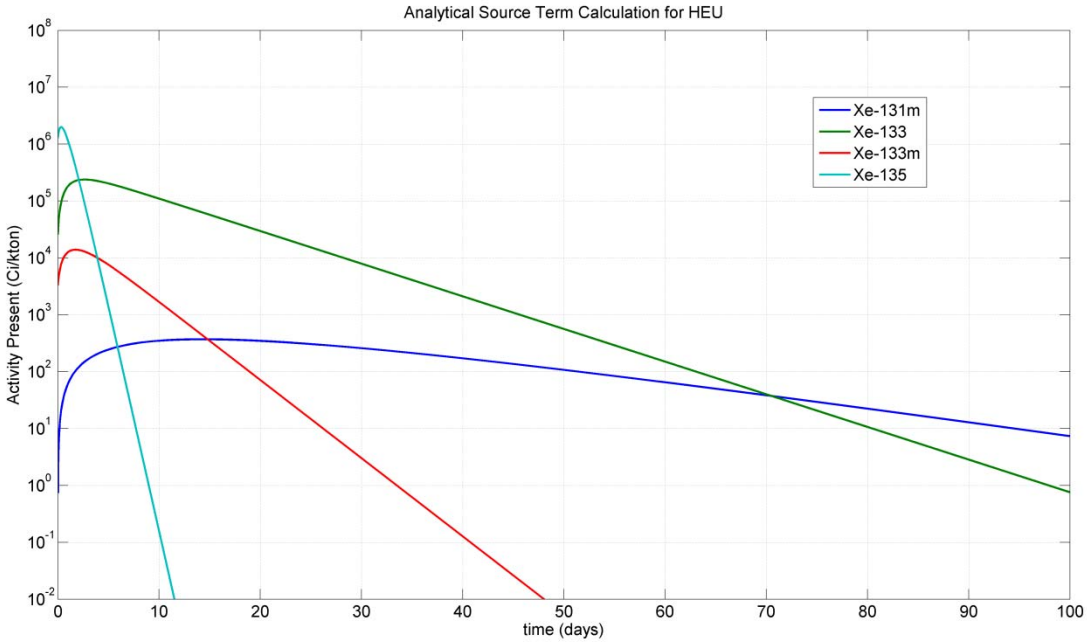

Figure 4.6. Radioxenon source term resulting from HEU core explosion.

4.2 Brief Tour of the Vertical Transport Code

The general physical system considered in this work consists of a depth L = 500 m to the system floor, an initial contaminant distribution of depth of L_0 = 300 m and therefore an initial fresh-air buffer zone extending down 200 m from the surface. In line with the considerations of Nilson et al. (1991), in the base case of study the fracture width

is taken to be $\delta_f = 1$ mm and the fracture separation $\delta_m = 1$ m. The porosities of the fracture and matrix are respectively $\phi_f = 1$ and $\phi_m = 0.1$ and the matrix permeability is assumed to be $k_m = 10^{-15}$ m^2.

The transport code requires as input a history of the surface pressure over the timescale to be studied as given by the $1 \times$ `Cycles` vector `Press`. This work assumes a sinusoidal variation in surface pressure defined as follows

```
12    Static_Pressure=10^5;                %this is the time-averaged static pressure
13    delP=(2/30)*Static_Pressure;         %this is the maximum deviation from the mean
14    Press=zeros(Cycles,1);
15    for ii=0:(Cycles-1)
16        Press(ii+1)=Static_Pressure + delP*cos(8.7266E-6*ii*600);
17    end
18    PressNew = Press(:) - Static_Pressure;
```

The argument of the cosine function in line 16 is assuming that the period of the pressure variations is T = 200 hours, and each time step or cycle corresponds to a step of 600 seconds. In actuality, the surface pressure history can be entirely arbitrary, and be compiled with true meteorological data if such information is available. For purposes of analyzing the code response, the simple sinusoidal variation is ideal.

While the model mesh is defined with $N \times M = 200 \times 7$, due to the iterative (implicit) nature of many of the `for` loops, the modeled mechanical system actually exists in $[i, j] = [3 : N-2, M]$. As assumed in Chapter 3, the first column of the mesh, j = 1, contains the fracture, while j = 2:M contain the matrix. Particularly crucial to the code structure are the $N \times M \times 2$ matrices `p` and `CONC`. These two matrices contain the calculated pressure response and subsequent concentration values at each of the $N \times M$ grid points in the system for the current time step calculation as well as from the previous time step. In the notation of Chapter 3, $n = 1$ and $n+1 = 2$ within these structures for all steps.

The surface of the system is taken to consist of the mesh lying at or above $i = 4$, and at the end of a given time step calculation, the surface is skimmed for new contaminant outflow during that time step as follows

```
442     deloverflow = CONC(4,1,2);
443
444     OVERFLOW(time)=OVERFLOW(time-1)+deloverflow;
445     C_OVERALL(time) = sum(sum(CONC(4:N,:,2))) - deloverflow;
446     C_SURF(time)= CONC(4,1,2);
447
448     OUTFLOW(time)=OVERFLOW(time)/C_OVERALL(1);
449     OUTFLOW(time)                           %just added to display during execution
450     INSTANT_OVERFLOW(time) = deloverflow;
```

The variable `deloverflow` contains the amount of contaminant that has been transported into the surface layer during the current time step. The vectors `OVERFLOW` and `OUTFLOW` in lines 442 and 446 track the cumulative amount of contaminant reaching the surface throughout the execution of the code. Contaminant that reaches the surface is assumed to completely leave the system and no longer reenters subsequent calculations.

4.3 Transport Code Evaluation without Decay and Single Source

In A.6 of the Appendix, the full MATLAB code for the vertical transport model is shown. In this section, the code will be evaluated by considering the vertical transport of only an initial distribution of contaminant at time $t = 0$ with no new source, and radioactive decay will *not* be taken into account. Modification of the code to suit this is relatively simple and noninvasive, and can be achieved by forcing `NewConcentration = 0` and `decay = 0`. The goal of the evaluation is to demonstrate that the transport code exhibits the transport phenomena as expected and in line with analytical bounds set in Chapter 2. Values for the fracture width of $\delta_f = 1$ mm and the fracture separation of $\delta_m = 1$ m are utilized. The porosities of the fracture and matrix are respectively $\phi_f = 1$ and $\phi_m = 0.1$ and the matrix permeability is assumed to be $k_m = 10^{-15}$ m^2. The period of barometric oscillations is remains $T = 200$ hours.

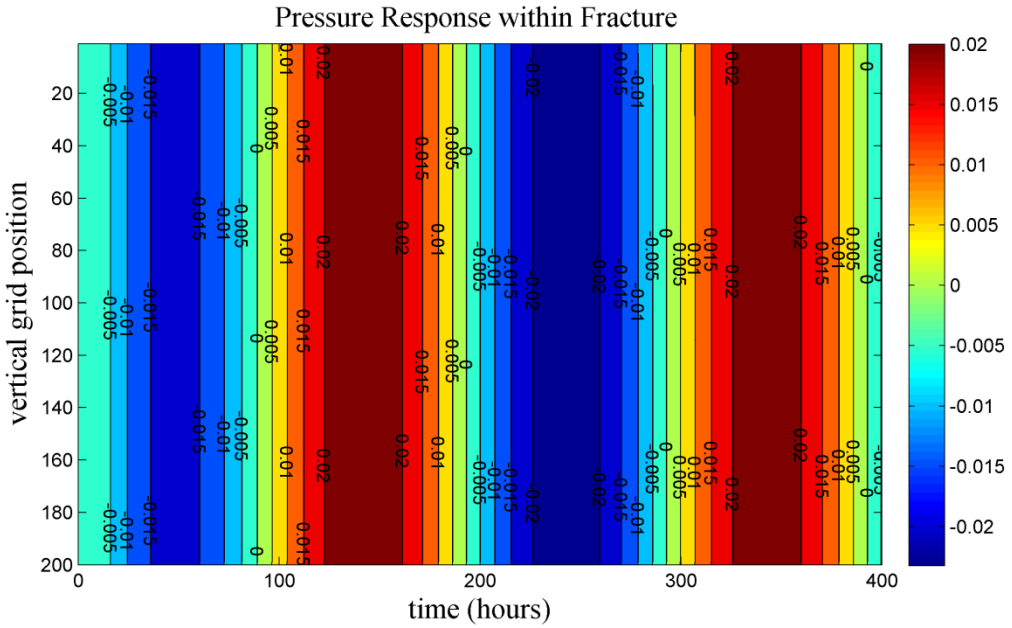

Figure 4.7. Pressure response along the fracture over two periods of barometric oscillations.

Figures 4.7 and 4.8 show examples of the pressure response within the system over two full periods of barometric oscillations. In Figure 4.7, the vertical pressure response within the fracture as a fraction of the variation from the static mean p_0 is shown versus time. Clearly the surface pressure, which begins the cycle at the mean static pressure and dips lower, propagates rapidly down the fracture with virtually no lag. As compared to the analytical solution to the pressure response in the homogeneous, porous medium of Figure 2.6, the pressure response propagating down the fracture does not encounter a porous medium ($\phi_f = 1$) to slow its progress. This result is nearly identical regardless of what vertical slice, j, is examined because the response deeper within the matrix is determined by the pressure at the fracture-matrix interface. If the pressure response along the fracture is nearly constant, then the pressure response as it propagates into the matrix will remain nearly constant along all vertical slices.

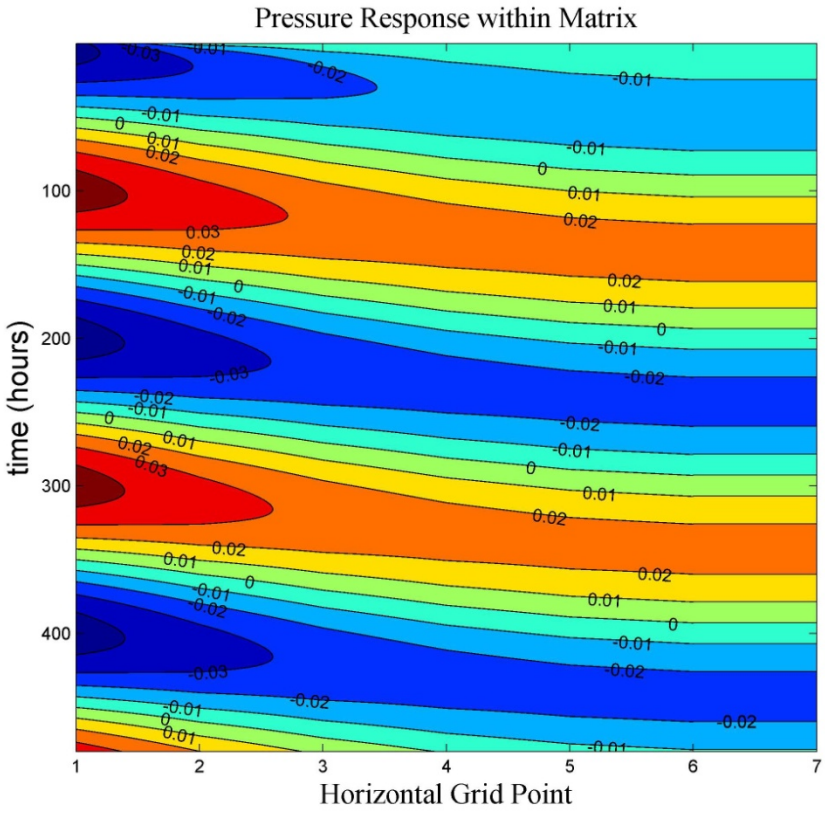

Figure 4.8. Pressure response across a horizontal slice of the matrix over two periods of barometric oscillations at depth $x = 400$ m . Note: time evolves downwards on the plot.

Figure 4.8 is a far more interesting and convincing depiction of the effectiveness of the pressure response portion of the vertical transport code. This plot was constructed by considering the time evolution of the pressure response within a single horizontal slice of the system, so that time evolves from top to bottom in the figure. Unlike Figure 4.7, Figure 4.8 does in fact resemble the analytical response of Figure 2.6, and it should (rotated 90˚ of course). As the pressure at the fracture-matrix interface propagates inwards, it encounters the porosity of the matrix medium, thus slowing it down significantly. The result is that there is a significant time lag between the pressure at fracture and the subsequent response within the matrix. Not only that, the full amplitude

of variation of the pressure never fully penetrates the matrix unless the fracture separation δ_m is made to be substantially smaller.

Figures 4.9, 4.10, and 4.11 on the following pages show 16 plots depicting the migration of the contaminant front over periods of time ranging from 1 hour to 100 days. These plots were constructed simply from snapshots of the CONC matrix at different times, zoomed in on the middle part of the mesh defined by grid points $i, j = (60:100, 1:7)$ to view the area just above and below the original contaminant-buffer interface which lies at $i = 80$. The initial contaminant distribution can be seen in the first plot of Figure 4.9 at $t = 0$. Before delving into these plots, note that the first "column" of the plots, corresponding to $m = 1$, represents the fracture. As has been noted previously, vertical transport within the fracture takes place on a very different time scale than horizontal transport in the matrix. As such, details within the fracture depicted in these plots actually offer little insight; taking the snapshots at slightly different points in time most likely would have yielded very different fracture concentrations.

At $t = 1$ hour, the time step from $t = 0$ is small enough to observe a small transport of tracer up one cell within the fracture; nothing appears yet to have diffused. As shown in the next two plots, within one period of barometric oscillation (8 days), the filtering effects of fracture-matrix seepage can be seen as contaminant has started to migrate into the first 3 matrix layers above the initial interface. At day 16, the migration of the contaminant front is clearly evident from the color stacking on top of the original interface. Continuing through days 20, 24, and 35, the concentrations in the above layers reach levels of the same order of magnitude as the original distribution below the interface. By days 40 and 50, the original line of interface appears to have retreated downwards.

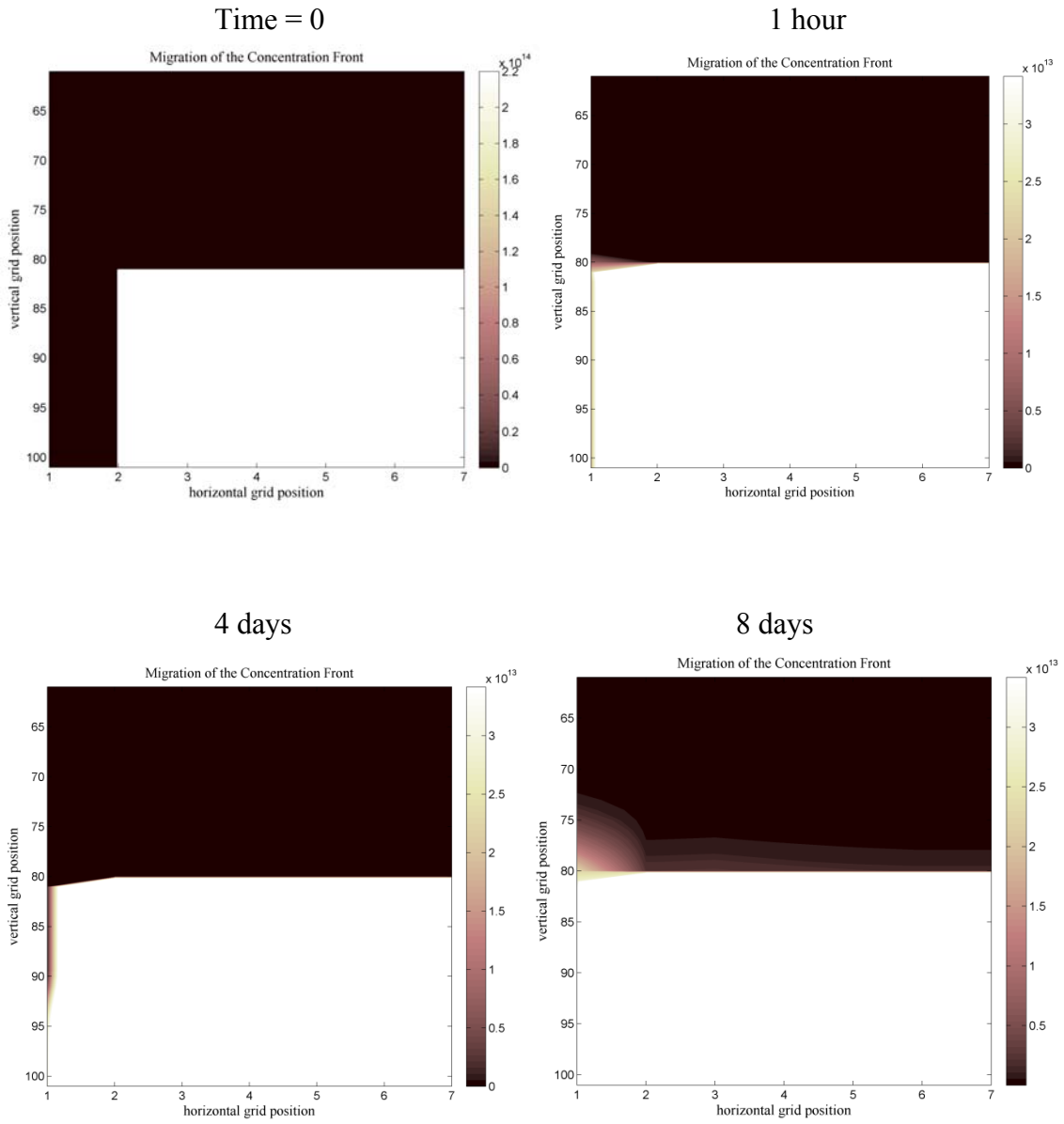

Figure 4.9. Migration of the contaminant front at $t = 0$, 1 hour, 4 days, 8 days. Period of barometric oscillation is 200 hours; single static source, no decay. Vertical grid scale is 5/2 m per grid point and horizontal grid scale is 1/7 m per grid point.

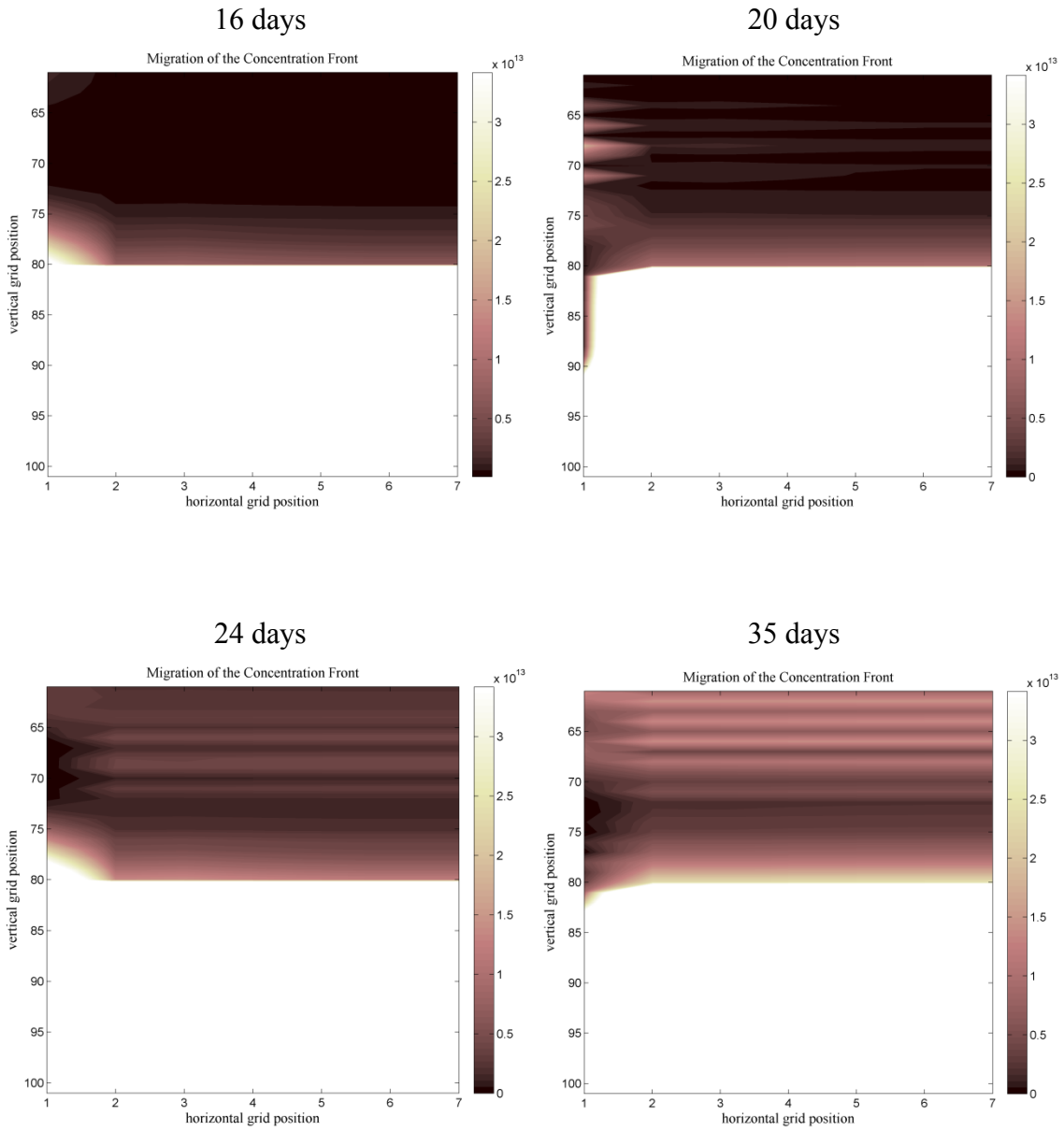

Figure 4.10. Migration of the contaminant front at t = 16 days, 20 days, 24 days, 35 days. Period of barometric oscillation is 200 hours; single static source, no decay. Vertical grid scale is 5/2 m per grid point and horizontal grid scale is 1/7 m per grid point.

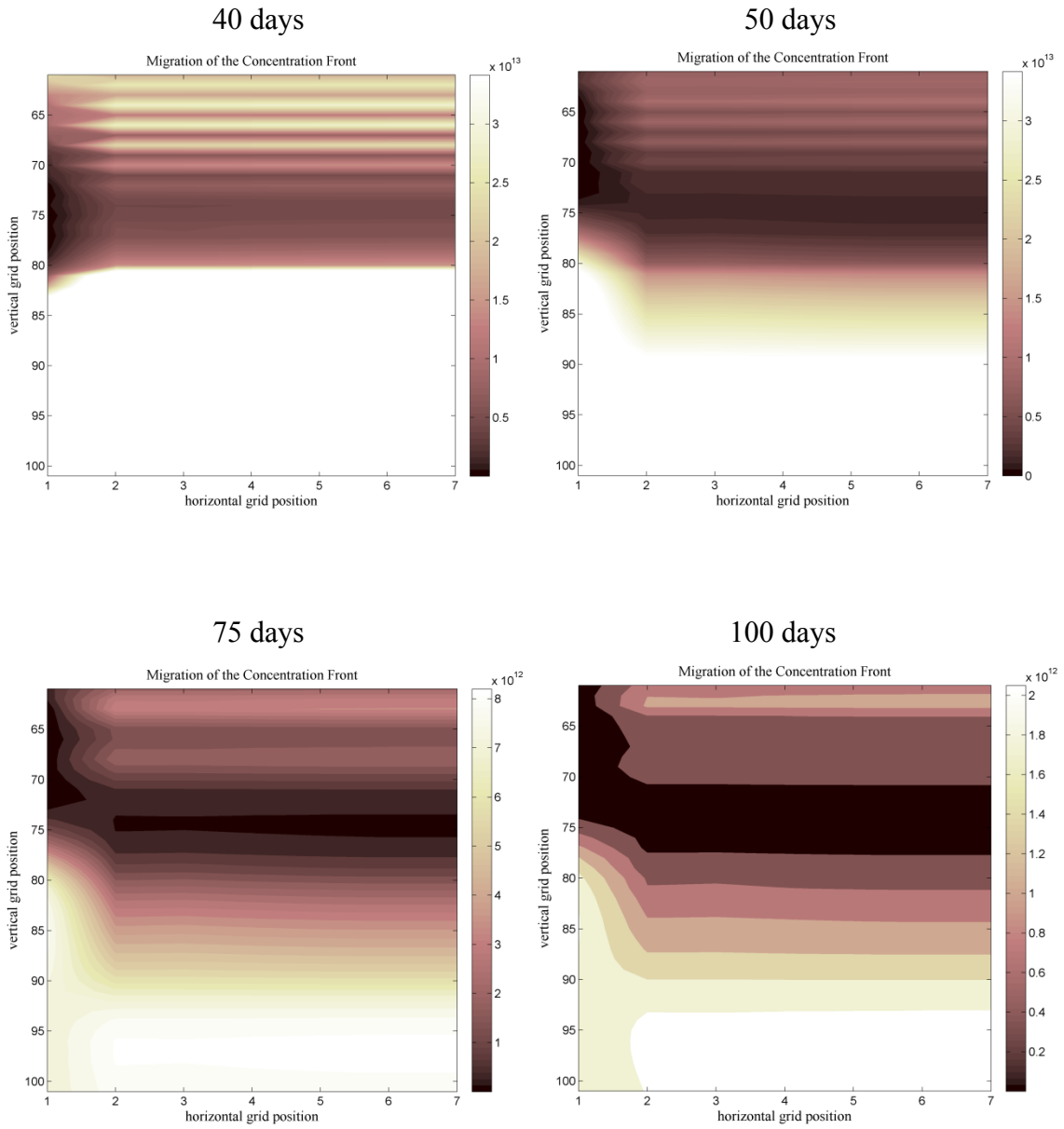

Figure 4.11. Migration of the contaminant front at t = 40 days, 50 days, 75 days, 100 days. Period of barometric oscillation is 200 hours; single static source, no decay. Vertical grid scale is 5/2 m per grid point and horizontal grid scale is 1/7 m per grid point. *Note the switch in color magnitudes on the last two plots.

Plots for 75 days and 100 days show more than an order of magnitude decrease in original concentration due to the upward stretch of the concentration gradient. Note that the color scale in these last two plots has dropped from 10^{13} Bq/ m^3 to 10^{12} Bq/ m^3. Also evident in these plots is the piston-like ratcheting effect that is characteristic of the barometric pumping combined with the fracture-matrix seepage. The importance of this effect is evident in Figure 4.12. In the early *time-filtering* regime for the first three months or so, the outflow is suppressed due to filtering by the fracture-matrix diffusion of gas moving along the fracture. As the concentration gradient extends upward, the pumping begins to pull ever more gas to the surface until a so-called *quasi-steady* state is achieved during which as much as 1% of the original subsurface contaminant is brought to the surface each cycle. This observation is very much consistent with the conclusion of Section 2.3 regarding the total efficiency of the analytical model as summarized by Eq. (2.32).

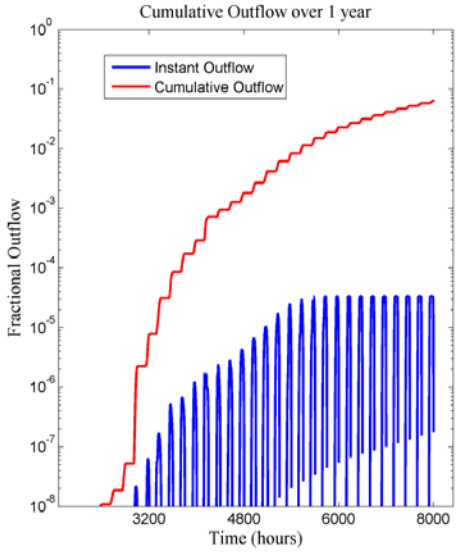

Figure 4.12. Cumulative Fractional Outflow overlaid with the instantaneous fractional outflow over a roughly 1-year period.

4.4 TRANSPORT CODE WITH RADIOACTIVE DECAY AND GENERALIZED SOURCE TERM

With the addition of radioactive decay to the vertical transport code, the primary force behind contaminant removal from the system is no longer attributable to the physical transport mechanisms being modeled, but to the decay of the source. For this reason, there was no way to examine the modeling of the physical processes within the system in Section 4.3 if radioactive decay had been included.

Including the effects of radioactive decay in the transport model can be implemented in a number of different schemes. Broadly speaking, however, there are two options. First, the decay can be instituted within the conservation equations as shown in the derivations of Chapter 3. In this manner, the decay factor occurs as a component of the inhomogeneous coefficient F, which incorporates all of the past system knowledge. Second, the radioactive decay can be applied at the beginning (or end) of each cycle to basically decay the cell concentrations of the previous system state by one time step Δt. For small enough time steps, these two options were found to yield the same effects. Of the two methods, the first is obviously more elegant; however, the second offers the capability to explicitly track the amount of decay, an advantage that will be explained next in the context of another challenge to implementing the vertical transport code.

Inclusion of the effects of radionuclide decay in the transport code is coupled with the need to ascribe a time-varying source term to each nuclide studied in the model – for example, as ^{133}Xe decays away within the system it is also being produced as a result of the decay of both ^{133}I and the meta-stable ^{133m}Xe; see Figure 4.4. So *not only* must the capacity to include a time-varying source term be considered, but given that ^{133m}Xe and ^{135m}Xe are parent nuclides to ^{133}Xe and ^{135}Xe respectively, the vertical transport model must also account for the vertical transport of the source itself.

A relatively simple scheme is introduced to combat this challenge of incorporation of a time-varying, migrating source term. First, using the source term results of Section 4.1, new `[1 × Cycles]` vectors `NewSourceXe13--` are introduced to estimate the quantity of new concentration that is added to the overall source. This is accomplished within the framework of the analytical source term code A.5 of the Appendix by

```
214 for i=2:Cycles+1
215     NewSourceXe133(i)= AXe133(i)-AXe133(i-1)*exp(-LXe133*.006944);
216     NewSourceXe133m(i)= AXe133m(i)-AXe133m(i-1)*exp(-LXe133m*.006944);
217     NewSourceXe131m(i)= AXe131m(i)-AXe131m(i-1)*exp(-LXe131m*.006944);
218     NewSourceXe135(i)= AXe135(i)-AXe135(i-1)*exp(-LXe135*.006944);
219     NewSourceXe135m(i)= AXe135m(i)-AXe135m(i-1)*exp(-LXe135m*.006944);
220 end
```

The concentrations $C(t+1)$ and $C(t)$ are known for each time step. For small time steps Δt they can be related by

$$C(t+1) = C(t) - decay(t) + NewSource(t+1). \tag{3.44}$$

Since the amount decayed is given by $decay(t) = C(t)(1-\exp(-\lambda\Delta t))$, Eq. (3.44) can be rearranged to give

$$NewSource(t+1) = C(t+1) - C(t)e^{-\lambda\Delta t} \tag{3.45}$$

which is precisely the expression found in Lines 215-219 above.

Now, `NewSourceXe13--` tracks the total amount of additional concentration that was created by the parent nuclides in the previous time step. This added source can be thought of as being composed of two components: a static part from non-migrating nuclides and a migrating part resulting from the transport of a parent nuclide. The scheme requires that vertical transport of the parent nuclide be modeled first. Using ^{133}Xe as the example, first the vertical transport code is run on ^{133m}Xe. As the concentrations within each cell are decayed from the previous step, the amount of ^{133m}Xe decayed in each cell is tracked in a (extremely large) `[N × M × Cycles]` size matrix

`NewDecaySource(i,j,time)`. This is accomplished by the commented out Line 176 of the transport code, the relevant portion of which is shown below. Then the vertical transport code is run on ^{133}Xe. This time through, before any new source is added to the system, the total amount of source resulting from decay of the migrating parent is subtracted off from `NewSourceXe133(time)`with this remaining portion being attributed to a static source, as seen in Lines 174-175 below. This static source will be assumed to be distributed evenly throughout the initial region of contamination. Note that the new quantity `NewDecaySource` for ^{133}Xe is commented out in Line 176 below because subsequent daughters are not being modeled. With migrated and non-migrated sources separated, the migrated decay source `NewDecaySource(i,j,time)` is added cell by cell in Line 179. The static source, with concentration `NewConcentration` as determined in Lines 174-175, is then added in Line 181.

```
174         NewConcentration = (NewSourceXe133(time)-...
175             sum(sum(NewDecaySource(:,:,time))))/((200-Interface)*6);
176         %NewDecaySource(:,:,time) = CONC(:,:,2)*(1-exp(-decay*delta_t));
177 %this determines the decayed amount in each cell to be used for modeling of daughter
178          CONC(:,:,2) = CONC(:,:,2)*exp(-decay*Del_t);
179         CONC(:,:,2)= CONC(:,:,2) + NewDecaySource(:,:,time);
180 %this adds the migrating portion of NewSource resulting from parent decay
181         CONC(Interface:N,2:M,2)=CONC(Interface:N,2:M,2)+NewConcentration;
182 %this adds the stationary portion of NewSource to the original contam. distribution
183         NewSource(time)=sum(sum(CONC(:,:,2)))-sum(sum(CONC(:,:,1)));
184 %this variable simply tracks how much new source is added each cycle
```

4.5 TRANSPORT RESULTS AND SENSITIVITY STUDY

With the vertical transport code fully functional, as an example application of the code to the problem of modeling the various radioxenon isotopes, the source term results of Section 4.1 were used to determine an estimated activity outflow for ^{131m}Xe, ^{133m}Xe, ^{133}Xe, and ^{135}Xe. Again, the system is taken to consist of a total depth of L = 500 m below the surface, with an initial source term distributed over L_0 = 300 m, leaving 200 m

of fresh-air buffer above the initial contaminant front. The following physical parameters were again utilized: the fracture width and separation is taken to be $\delta_f = 1$ mm and $\delta_m =$ 1m respectively; values of $\phi_f = 1$ and $\phi_m = 0.1$ for the fracture and matrix porosities were assumed, and the matrix permeability was $k_m = 10^{-15}$ m^2. The barometric pressure at the surface was taken to vary harmonically with period $T = 200$ hours and amplitude $\Delta p = 2/30 p_0$ about the mean static pressure $p_0 = 10^5$ Pa. The dynamic viscosity of air was taken to be $\mu = 2 \times 10^{-5}$ Pa·s. The resulting outflow is summarized in Figure 4.13.

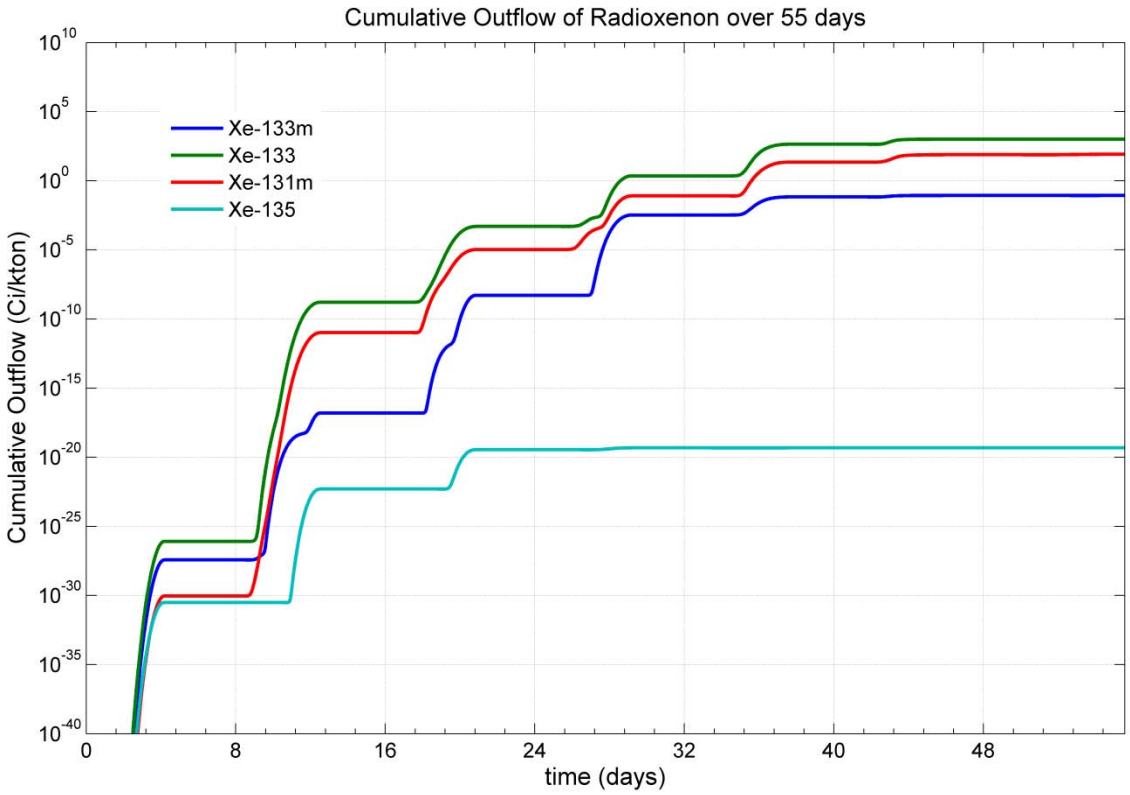

Figure 4.13. Estimated outflow of radioxenon from a 1 kton HEU explosion.

The affects of the barometric pumping driving force is clearly evident in Figure 4.13, as the outflows exhibit the characteristic step feature seen without radioactive decay. However, even with source terms that continue adding new concentrations to the system, all four radioxenon isotope outflows have ceased by day 50. The outflow of ^{135}Xe, despite having an initial activity of over 10^6 Ci, barely reaches a cumulative outflow of 10^{-20} Ci by 20 days before stopping.

Table 4.6 summarizes a cursory sensitivity study that was conducted on the major physical parameters of the system using the system configuration outlined above. This set of parameters and the resulting 55 day outflows depicted in Figure 4.13 form the first set of data in the table. While the sensitivity study described here was conducted with ^{135}Xe, the radioisotope was not included in the graphical results of Figures 4.14-4.18 simply because the resulting outflows were a minimum of 15 orders of magnitude smaller than the other three, variations of which could not be depicted on the same scale as the other three.

The first set of data considers variations of the fracture separation, δ_m, and is plotted in Figure 4.14. The effect of the fracture separation is probably the most complicated of all the parameters to make sense of due to its critical function in the barometric pumping process. On the one hand, smaller separations mean that trace gas within the matrix has less far to travel horizontally during barometric lows to enter the fracture. On the other hand, however, smaller separations mean that the trace gas migrating upwards along the fracture diffuses less into the buffer regions of the matrix. This is a *very* critical feature of the double-porosity model because if gas does not seep into the higher matrix levels, then the concentration gradient does not stretch upwards and no "ratcheting" effect ensues. The effect of radioactive decay complicates this balance even further because it places a time restriction on how long the contaminant has

to migrate upwards and establish quasi-equilibrium, and therefore it tends to lend more importance to the first of the above critical effects.

Table 4.6. Summary of vertical transport code sensitivity study. The shaded rows are for the initial system configuration that was used to produce Figure 4.13. Parameters are varied around these values.

Physical Parameters					**Cumulative Outflow at 55 days (Ci)**				**Ratio**
δ_m (m)	δ_f (m)	$\Delta p/p_0$	ϕ_m	ϕ_f	^{133m}Xe	^{133}Xe	^{131m}Xe	^{135}Xe	^{133m}Xe/^{131m}Xe
0.1	1.001	2/30	0.1	1	3.651E-04	1.007E+00	3.425E-02	3.185E-13	1.066E-02
0.25	0.001	2/30	0.1	1	1.536E-02	4.518E+01	3.552E+00	5.851E-13	4.324E-03
0.5	0.001	2/30	0.1	1	2.726E-05	2.269E+02	2.439E+01	4.847E-19	1.118E-06
1	0.001	2/30	0.1	1	8.608E-02	1.022E+03	8.147E+01	4.753E-20	1.057E-03
2	0.001	2/30	0.1	1	1.536E-02	9.857E+02	8.553E+01	5.853E-24	1.795E-04
5	0.001	2/30	0.1	1	6.557E-04	1.728E+01	8.023E-02	2.509E-26	8.173E-03
10	0.001	2/30	0.1	1	2.563E-03	9.215E+01	2.901E+00	1.344E-24	8.834E-04
1	0.00005	2/30	0.1	1	3.507E-02	7.394E+02	7.379E+01	0.000E+00	4.754E-04
1	0.0001	2/30	0.1	1	9.782E-02	9.209E+02	6.378E+01	6.076E-21	1.534E-03
1	0.0005	2/30	0.1	1	5.924E-02	1.184E+03	7.915E+01	1.198E-20	7.484E-04
1	0.001	2/30	0.1	1	8.608E-02	1.022E+03	8.147E+01	4.753E-20	1.057E-03
1	0.002	2/30	0.1	1	9.203E-02	1.023E+03	8.267E+01	5.645E-20	1.113E-03
1	0.005	2/30	0.1	1	9.070E-02	1.124E+03	7.827E+01	6.359E-20	1.159E-03
1	0.01	2/30	0.1	1	8.202E-02	1.071E+03	7.732E+01	5.134E-20	1.061E-03
1	0.05	2/30	0.1	1	8.030E-02	1.025E+03	8.341E+01	1.483E-20	9.628E-04
1	0.001	5/90	0.1	1	1.009E-03	2.307E+02	4.492E+01	1.712E-29	2.246E-05
1	0.001	2/30	0.1	1	8.608E-02	1.022E+03	8.147E+01	4.753E-20	1.057E-03
1	0.001	7/90	0.1	1	5.820E-01	2.660E+03	9.990E+01	7.236E-16	5.826E-03
1	0.001	8/90	0.1	1	2.084E+00	4.694E+03	1.638E+02	1.623E-13	1.272E-02
1	0.001	2/30	0.01	1	2.276E-01	1.586E+03	1.105E+02	8.761E-18	2.059E-03
1	0.001	2/30	0.05	1	1.567E-01	1.258E+03	1.002E+02	1.589E-19	1.565E-03
1	0.001	2/30	0.08	1	1.104E-01	1.101E+03	9.544E+01	5.922E-23	1.157E-03
1	0.001	2/30	0.1	1	8.608E-02	1.022E+03	8.147E+01	4.753E-20	1.057E-03
1	0.001	2/30	0.2	1	6.195E-03	5.978E+02	6.294E+01	7.169E-32	9.842E-05
1	0.001	2/30	0.3	1	1.012E-03	1.922E+02	8.438E+00	1.881E-34	1.200E-04
1	0.001	2/30	0.5	1	9.151E-09	2.055E-05	1.513E-08	1.960E-38	6.048E-01
1	0.001	2/30	0.1	0.5	3.323E-25	1.123E-20	1.665E-18	1.484E-53	1.996E-07
1	0.001	2/30	0.1	0.7	1.037E-05	8.090E-01	1.899E-03	1.024E-41	5.459E-03
1	0.001	2/30	0.1	0.9	6.296E-03	4.551E+02	5.489E+01	1.373E-27	1.147E-04
1	0.001	2/30	0.1	1	8.608E-02	1.022E+03	8.147E+01	4.753E-20	1.057E-03

With regard to Figure 4.14, fracture separations below 1 m lead to a decrease in the outflow at 55 days, attributable to the lack of effective seepage in the buffer regions. At *very* small fracture separations on a scale similar to the fracture width (1 mm here), the code begins to break down significantly as huge velocity gradients surpass the capability of the FRAM scheme to eliminate spurious oscillations. Also the model mesh becomes insufficient to characterize cell by cell flows over any reasonable length of time, again due to velocity gradients. At slightly larger values than 1 m, the effects of radioactive decay begin to outweigh the benefit of fracture-matrix diffusion. Beyond 5 m, the outflow again rises slowly, but never back to the levels of around 1 m.

In contrast, variation of fracture width, δ_m, exhibits very little affect on the resulting outflow of all three radioxenon isotopes. Once again this is somewhat expected because even though a larger width can cause faster vertical flow along the fracture, these effects will be countered by a subsequent decrease in the rate of fracture-matrix diffusion, which tends to lessen the overall outflow. Attention should be drawn here to the fact that in Chapter 3 the transport model was built assuming $\Gamma = A$, where A is the cross-sectional area of the fracture and Γ is the fracture-matrix contact area per unit length. Realistically, variation of the fracture width would inevitable alter the value of the ratio Γ / A, and therefore the sensitivity study on δ_m oversimplifies the effect of this variation.

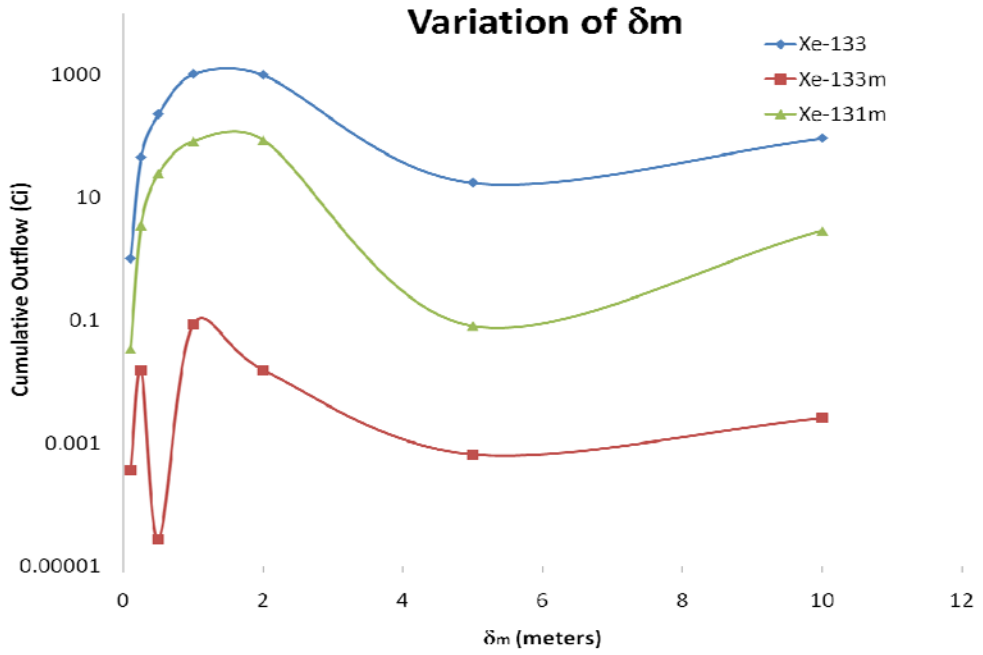

Figure 4.14. Sensitivity study on δm at 55 days.

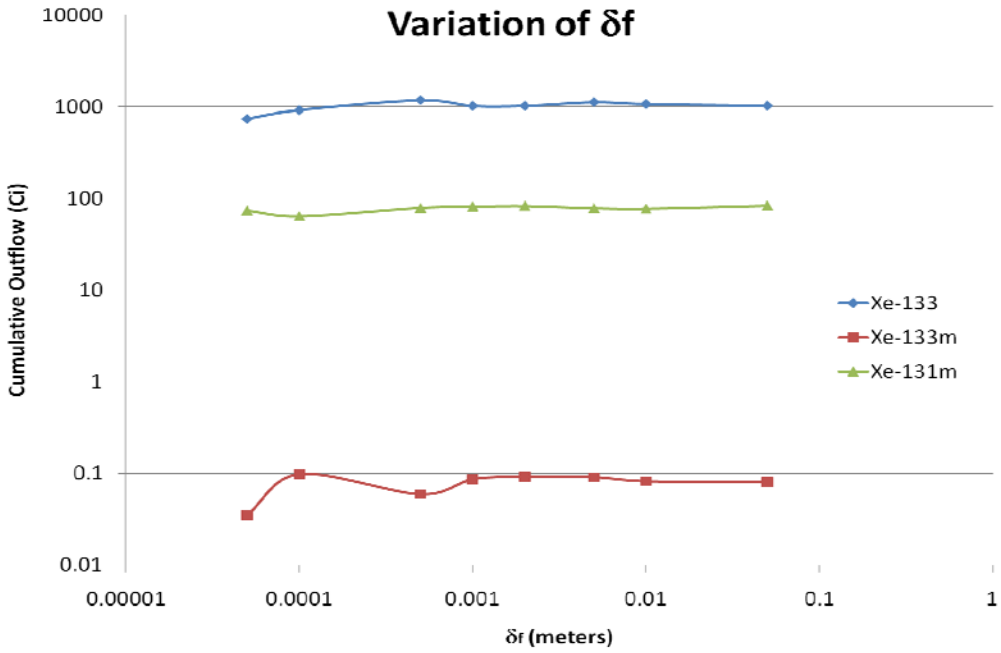

Figure 4.15. Sensitivity study on δf at 55 days.

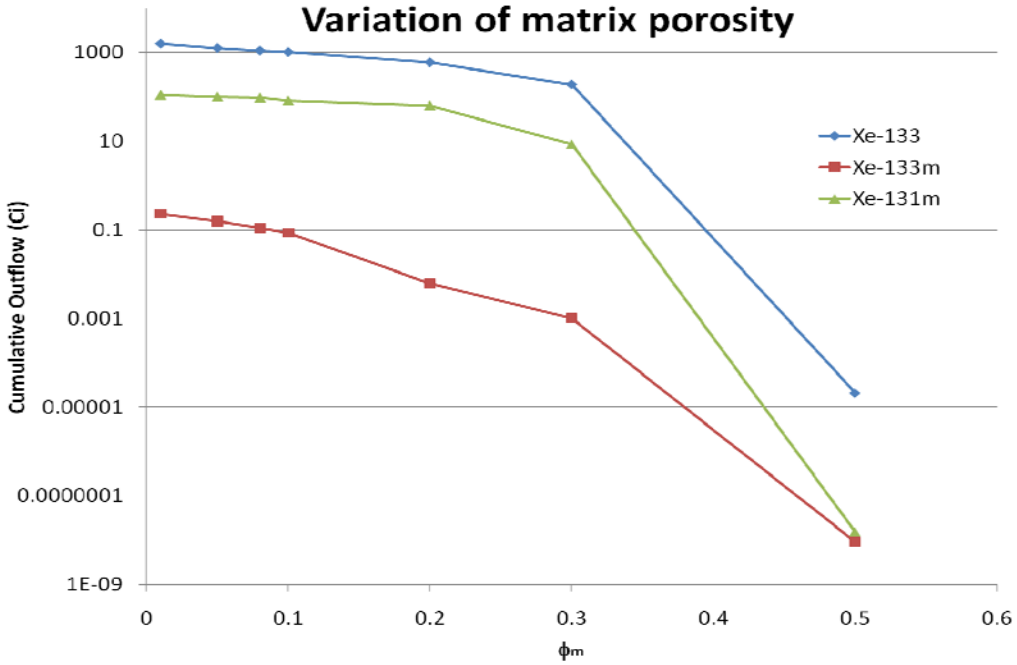

Figure 4.16. Sensitivity study on ϕm at 55 days.

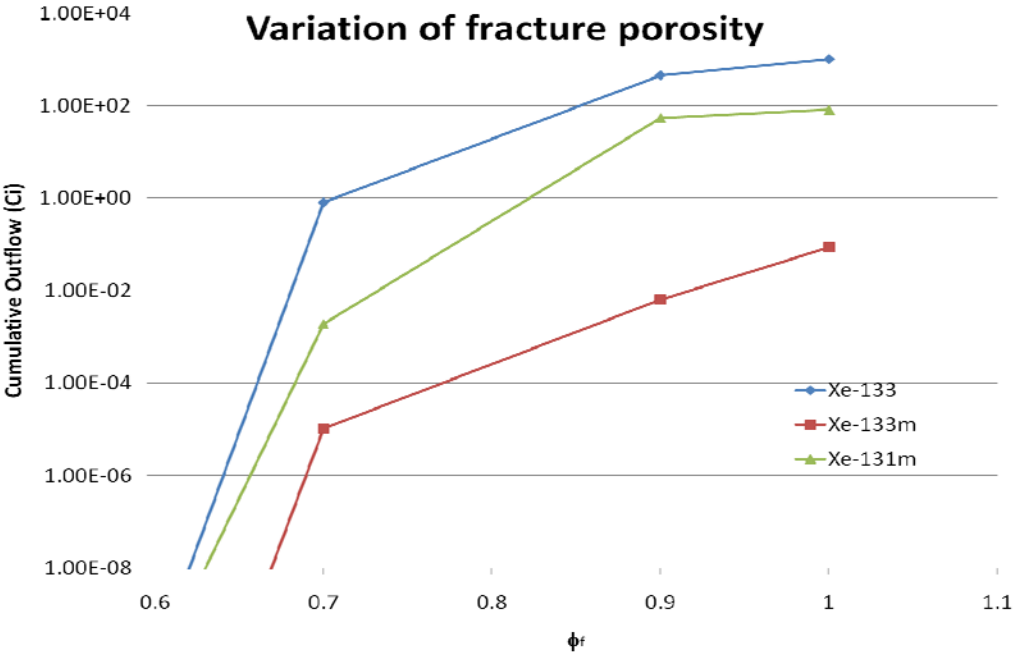

Figure 4.17. Sensitivity study on ϕf at 55 days.

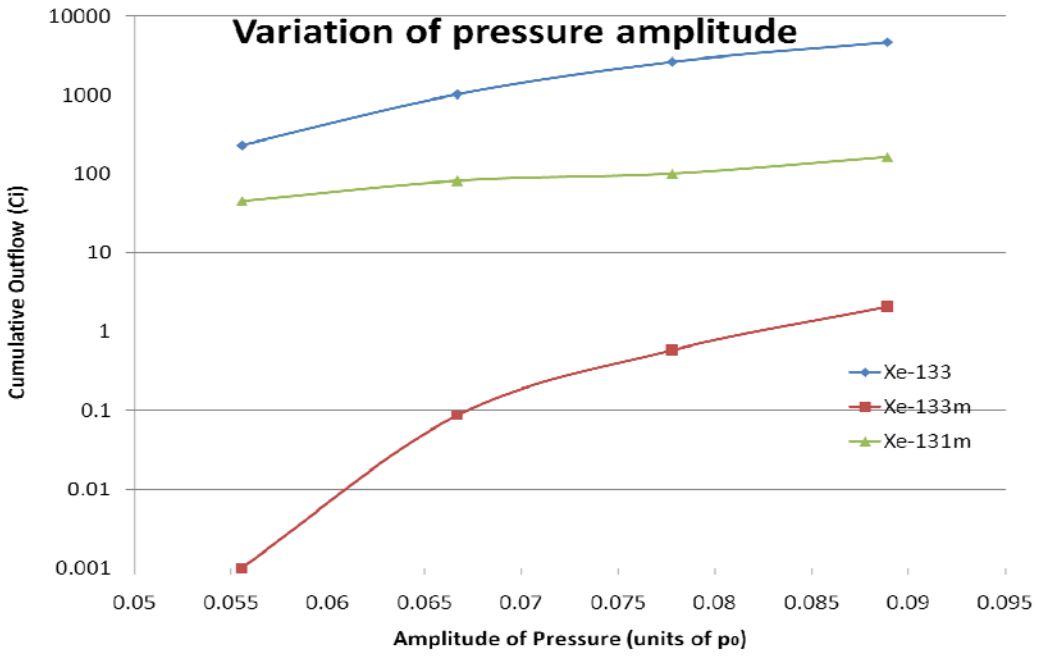

Figure 4.18. Sensitivity study on $\Delta p/p_0$ at 55 days.

The effect of varying the matrix porosity ϕ_m is shown in Figure 4.16 and shows a relatively easy to explain correlation. The net effect of increasing the matrix porosity is that pressure waves extend increasingly far into the matrix, and subsequently horizontal advection essentially washes out the fracture-matrix seepage mechanism required for the barometric "ratcheting" effect. Beyond porosities of 0.3 to 0.5, the system has basically evolved into the very ineffectual scenario of the homogeneous medium considered in Section 2.2.3.

Decreasing the fracture porosity ϕ_m below 1.0 has an equally decided effect on the overall outflow, as shown in Figure 4.17. The effect of a lower porosity in the fracture is essentially to inhibit the importance of barometric pumping. Lower porosity means a much diminished pressure response within the fracture, and a complete squashing of the pressure response within the matrix. With no pressure variation, no advection occurs.

Once again, the model dissolves into that of a homogeneous medium like in Section 2.2.3.

Figure 4.18 shows the results of varying the amplitude of the pressure variations. Given that the entire model is based on transport driven by pressure gradients, increasing the strength of the variations has the obvious effect of drawing out more of the contaminant. Of all the parameters of variation considered in the sensitive study, variation of the pressure amplitude seems to have the most direct, and profound, effect on the resulting isotopic ratio of cumulative radioxenon outflow. From Figures 4.3 – 4.5, the half-lives of ^{131m}Xe, ^{133m}Xe, and ^{133}Xe respectively are 11.9 days, 2.19 days, and 5.243 days. Now note from Figure 4.18 that ^{133m}Xe displays a very large dependence on the amplitude of the pressure while ^{131m}Xe outflow varies *much* more slowly. The significantly shorter half-life of the former means that its cumulative outflow is more strongly dependent on how fast the barometric pumping process occurs as compared to the longer-lived isotope. ^{133}Xe has a half-life significantly shorter than ^{131m}Xe but still twice as long as ^{133m}Xe; accordingly the effect of the increasing pressure amplitude is of a degree between that of the other two.

Finally, as a last demonstration of the potential of the vertical transport code in examining the radioxenon fractionation that results from subsurface transport, Figures 4.19, 4.20, and 4.21 below depict multi isotopic ratio correlation (MIRC) plots of the ratios ^{135}Xe/^{133}Xe versus ^{133m}Xe/^{131m}Xe as compared to the results of standard fully-fractionated and non-fractionated ^{235}U weapon models [35]. These figures were produced using the same 55 day calculation with the same default parameters as have been used throughout this chapter. In each case, one parameter, δ_m, δ_f or $\Delta p/p_0$, was varied and the vertical transport code was run while explicitly tracking the instantaneous contaminant

outflow during each iteration of the code. The data points represent averaged outflows during particular 4 day pressure-lows during which contaminant is escaping the system.

From the figures, the radioxenon fractionation exhibits a complicated response to the varied parameters in much the same way as described previously in reference to Figures 4.14-4.18. However, of greatest surprise in these figures is that isotopic fractionation caused by the vertical transport yields a number of outflows in which the ratios fall outside of the standard, expected limits as depicted by the red and blue lines corresponding to non-fractionated and fully-fractionated ^{235}U weapon models, though by 55 days the ratios typically fall back within the limits. Based on the vertical transport code calculations, clearly the subsurface transport can affect the isotopic fractionation of the radioxenon that emanates from a subsurface nuclear explosion. Additionally, these results solidify the need for a much greater sensitivity study and refinement of the code to further explore the effects of the vertical transport on radioxenon fractionation.

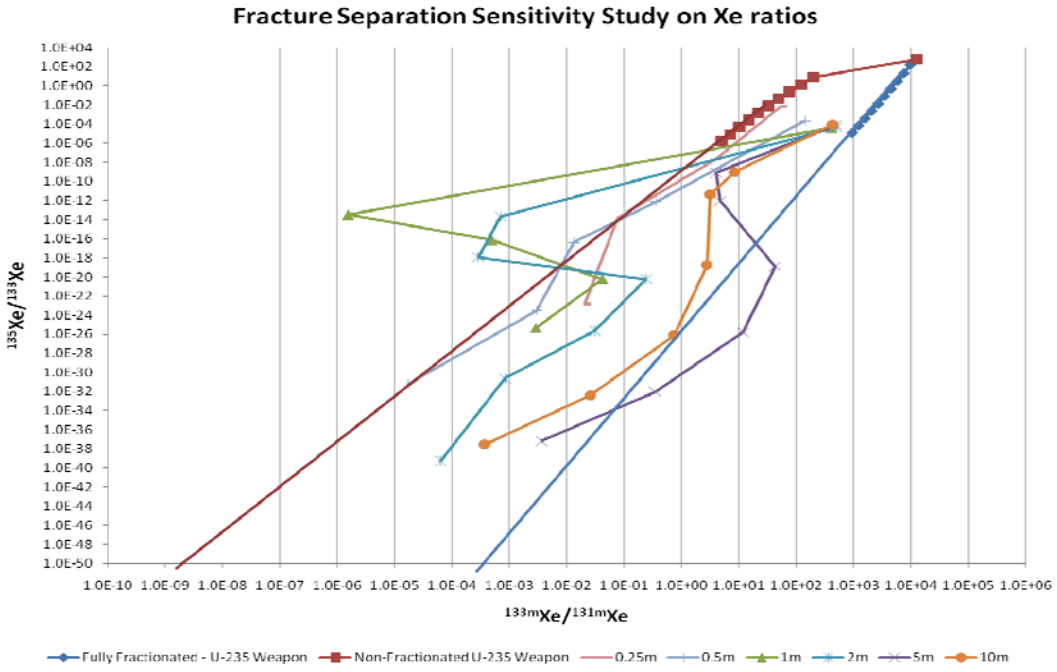

Figure 4.19. Xe fractionation sensitivity to fracture separation δ_m out to 55 days.

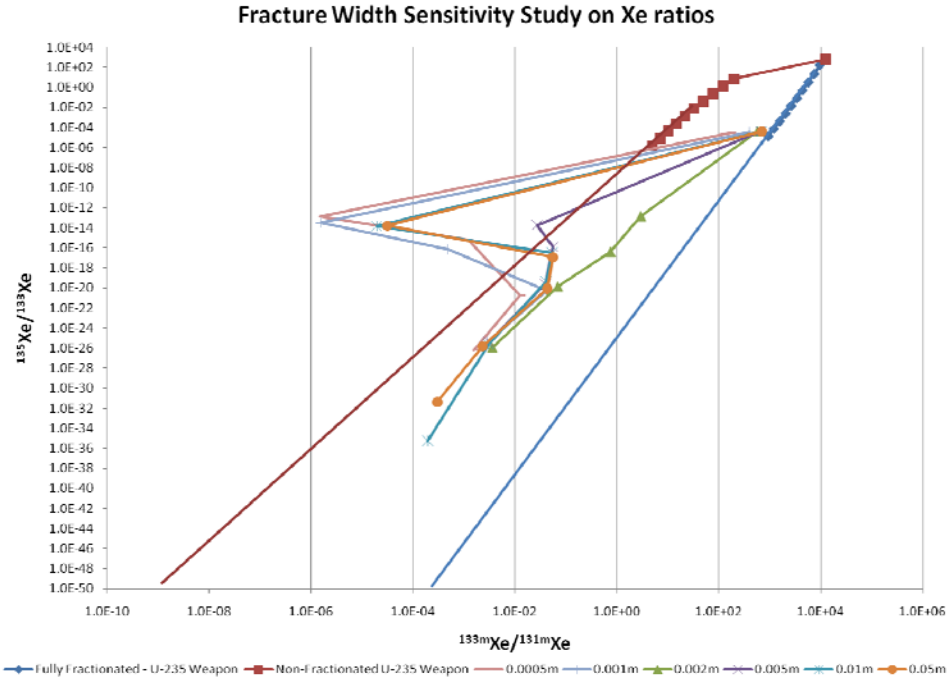

Figure 4.20. Xe fractionation sensitivity to fracture width δ_f out to 55 days.

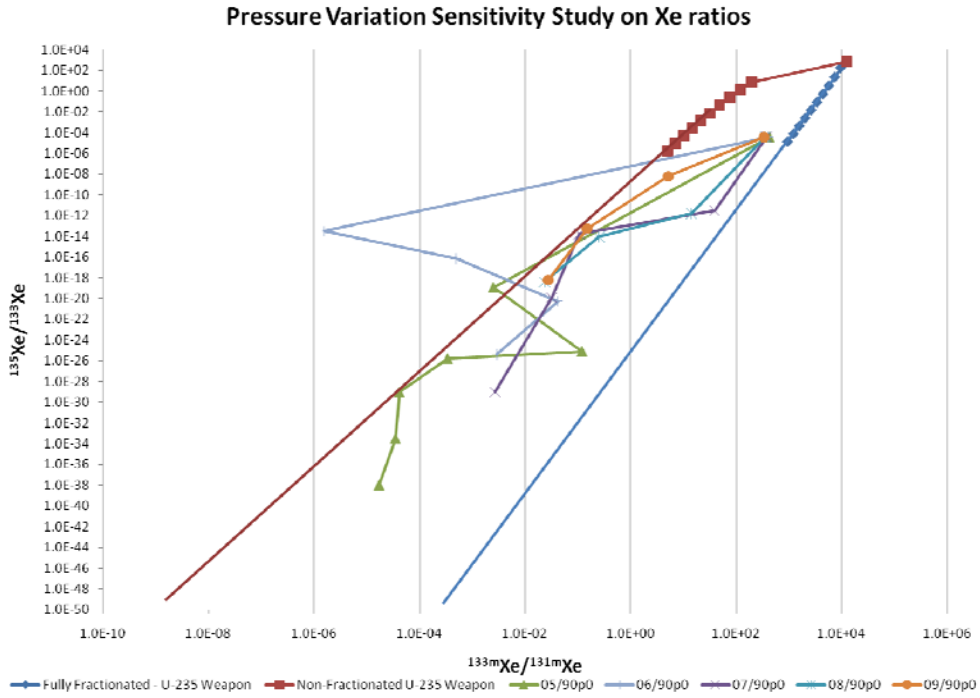

Figure 4.21. Xe fractionation sensitivity to pressure variation $\Delta p/p_0$ out to 55 days.

Chapter 5: Conclusions and Recommendations

The broad objective put forward for this work was to develop, implement, and ultimately evaluate a complete model for the detonation of a simple underground nuclear explosion and the subsequent vertical transport of resulting radioxenon to the surface. This task therefore consisted of two integral components. First, the fast-fission burn of a fissile spherical core normalized to 1 kton total energy was modeled with a surrounding layer of geologic medium. The resulting source term was then used in the testing and evaluation of the constructed vertical transport model, written in MATLAB.

The codes MCNP5 and ORIGEN 2.2 were utilized in the calculation of the nuclear explosion source terms. MCNP5 was used to determine the neutron flux profiles of a modeled explosion scenario in which a 8.7 cm HEU (or 5.1 cm Pu) core was fissioned over 1 μs with 200 cm of various compositions of surrounding geologic media. The thickness value of 200 cm was determined numerically as a suitable thickness to guarantee that less than 0.1% of the system neutrons escaped. ORIGEN 2.2 was used in tandem with MONTEBURNS and MCNP to track the changing material compositions within the system. The resulting source term was found to consist of the following initial inventories: $A_{Xe131m} = 5.252$ Ci/kton, $A_{Xe133m} = 3.3\text{E+3}$ Ci/kton, $A_{Xe133} = 2.58\text{E+4}$ Ci/kton and $A_{Xe135} = 1.275\text{E+6}$ Ci/kton. To facilitate the integration of the source term results in the vertical transport code, an analytical source term model was constructed to define the decayed source term values at arbitrary times following the definition of an initial inventory. The MATLAB code for this is shown in A.5 of the Appendix.

The vertical transport model developed for this work stems from the double-porosity model of 1D transport within a fractured, permeable medium. Oscillations in barometric pressure due to natural variations in weather can result in a literal barometric

pumping of deep subsurface contaminant that would otherwise take years to diffuse to the surface. The numerical scheme employed in this work was first suggested by Nilson et al. (1990). During periods of falling surface pressure, contaminant gas is drawn into fractures and pulled upward by advective flow driven by the pressure response within the fracture. Gas that would otherwise be pulled right back down fractures during subsequent pressure increases instead filters by diffusion into the fresh-air buffer regions where it is contained until the next period of falling pressure. Over many successive cycles, a net upward "ratcheting" of contaminant stretches the concentration gradient and eventually leads to outflow at the surface.

The complete MATLAB code for the vertical transport model is provided in A.6 of the Appendix. The model was first analyzed without inclusion of radioactive decay and time-evolving source terms. The model accurately calculates the pressure response within the system due to a harmonically varying surface pressure, and the upward migration of the contamination front exhibits the expected characteristics. Finally, through a sample calculation with a single initial source, the vertical transport model displayed a quasi-steady-state outflow of contaminant gas of an amount equaling nearly 1% initial inventory per barometric cycle, thus in good agreement with the analytical calculation considering the breathing and diffusion-exchange efficiencies.

The vertical transport code was then used to model the vertical transport of the full calculated radioxenon source. At the conclusion of this work, the model can take as input an arbitrary function specifying the barometric pressure at the surface, a time-evolving source term that includes both migrating and static components, and a specification of the physical system parameters, and from these estimate the resulting surface outflow as a function of time. A cursory sensitivity analysis was conducted on a number of system parameters, including the fracture width, fracture separation, matrix

porosity, fracture porosity, and amplitude of pressure, to determine how the radioxenon outflow responds. Overall, the analysis yielded variations in outflow that were in line with expectations. Variation in pressure amplitude, in particular, showed a large disparity (fractionation) in the outflow response among the various radioxenon isotopes. Finally, the radioxenon fractionation $^{135}Xe/^{133}Xe$ versus $^{133m}Xe/^{131m}Xe$ versus varied parameters δ_m, δ_f or $\Delta p/p_0$ was shown to lead to outflows that fell outside the standard bounds of expected non-fractionated and fully-fractionated ^{235}U weapon models. These interesting results suggest that subsurface vertical transport results in some degree of isotopic fractionation of radioxenon from an underground nuclear explosion. Certainly additional study is necessitated.

As a last demonstration of the vertical transport code functionality, a calculation of ^{133}Xe outflow was conducted with parameters meant to match a numerical estimate by Carrigan et al. (1996). Carrigan predicted that for a 1 kton nuclear explosion located 400m underground, after 50 days the surface gas concentration of ^{133}Xe would be 41 Bq/m^3. Using δ_m = 6.4 m and a depth of L = 400 m, $p_0 = 7.73 \times 10^4$ Pa and harmonic variation of pressure with an amplitude of $\Delta p = 2/30 p_0$ (other parameters fixed to their nominal values as used throughout this work), an average outflow of ^{133}Xe between days 48 and 55 was estimated to be 3.255×10^{-5} $Ci/min \cdot m^3$. Carrigan describes NTS (Nevada Test Site) source counters as being able to pump about 1 L/min; combined with a stated collection volume of 10^{-5} m^3 s, a resulting average surface gas concentration of 128.3 Bq/m^3 was estimated with the vertical transport model, representing a factor of 3 higher than the Carrigan estimate. However, due to the Carrigan estimate being assumed to be conservatively low, as well as the fact that the vertical transport code in this work assumed a perfectly harmonic pressure variation, the calculated value in this work is on par with the Carrigan prediction.

The explosion and vertical transport model developed and demonstrated satisfy all of the goals set forth for this work. Nevertheless, there are a numerous possibilities for further work. With regard to the nuclear explosion model, it should be understood that this work has essentially utilized MCNP and ORIGEN 2.2 to model what amounts to the absolute simplest nuclear explosion model possible. This is not just with respect to the modeling of the fission device. Virtually no consideration has been given to the physical impacts of an underground nuclear explosion, such as cavity melting and expansion or the formation of so-called stress-containment cages. Physical effects such as these can drastically alter the physical properties of the surrounding halo such that the subsequent gas transport is altered.

The vertical transport model developed considers a two-porosity system: fracture and matrix. Realistic systems contain depth-varying physical parameters, and the framework already exists in the code for the incorporation of a perfectly general system configuration and composition. The potential effects of such a complex extension to the code could be anticipated through a more thorough sensitivity analysis of the relevant physical parameters, which in and of itself would constitute a very natural extension of this work.

The framework also exists in the transport code for the input of an arbitrary barometric pressure history. For the purposes and scope of this work, this incorporation was not considered, but the results of the sensitivity analysis suggest a very strong correlation between the isotopic fractionation of radioxenon and the nature of the driving barometric pressure fluctuations. As such, this arbitrary pressure history extension should be considered a particularly critical next step.

Beyond these major considerations, the transport code could be refined in a very long list of ways. For instance, the implementation of the FRAM scheme can be extended

to include higher-order “filtering” of spurious oscillations. Higher-order differencing schemes combined with finer mesh configurations could increase the accuracy of the numerical solution scheme so long as the effects of numerical diffusion are held in check. Sorption effects were not considered in this work, and among other important parent nuclides, iodine was assumed to remain static within the system.

Beyond the extension of the code itself, it is expected that the developed vertical transport model will be further utilized to make predictions of the isotopic fractionation of radioxenon that results from its subsurface transport, which was indeed the original motivation for conducting this work.

Appendix

A.1 EXAMPLE KCODE MCNP DECK USED FOR K_{EFF} CALCULATION OF CORE

```
1          Solid Bare HEU sphere  ENDF/B-VI
2          1          1                  4.7984e-02          -1          imp:n=1
3          2          0                                                  1          imp:n=0
4
5          1          so         8.7407
6
7          kcode                         5000      1.2  50   250
8          sdef                        cel=1     erg=d1    rad=d2    pos=0.0 0.0 0.0
9          sp1                          -3
10         si2                          0.0    8.7407
11         sp2                          -21    2
12         totnu
13         m1         92234.66c   1.02     92235.66c   93.77
14                    92238.66c   5.21
15         prdmp    j    275
16         print
```

Line	Description of Input
1	Title Card
2	Defines cell 1 with material 1, density 4.7984×10^{-02} ($\times10^{24}$ atoms/cm^3), geometry of -1 (inside of surface 1) and with relative neutron importance 1
3	Defines cell 2 with material 0 (vacuum), geometry of 1 (outside surface 1) and with neutron importance 0
5	Defines surface 1 of type so (sphere) with radius 8.7407 cm
7	Specifies MCNP criticality source used to determine k_{eff} using 5000 source histories per cycle, initial guess of k_{eff} = 1.2, skipping the first 50 cycles before tallying, and running 250 cycles total
8	Defines a general source in cell 1, with energy distribution d1 (random) and radially distributed based on distribution d2 (random) about position (0,0,0)
9	Defines source probability of source 1 as -3, corresponding to Watt-fission spectrum
10	Defines source info of source 2 to be distributed in bin boundaries from 0 to 8.7407
11	Defines source probability of source 2 as -21 with parameter 2: given by a power law (uniform spread in a sphere)
12	total fission card; uses both prompt and delayed
13 & 14	Defines material 1 compositions with ^{234}U, ^{235}U, and ^{238}U.

A.2 TABLE OF GEOLOGIC MATERIAL COMPOSITIONS

*compositions are in ppm

		Rock			Soil	
Element		Wedepohl (1971)	Taylor (1964)	Mason (1966)	Vinogradov (1959)	Bowen (1966)
1	H	700	0	1400	0	0
3	Li	30	20	20	30	30
4	Be	2	2.8	2.8	6	6
5	B	9	10	10	10	10
6	C	320	200	200	20000	20000
7	N	20	20	20	1000	1000
8	O	472500	464000	466000	490000	490000
9	F	720	625	625	200	200
11	Na	24500	23600	28300	6300	6300
12	Mg	13900	23300	20900	6300	5000
13	Al	78300	82300	81300	71300	71000
14	Si	305400	281500	277200	330000	330000
15	P	810	1050	1050	800	650
16	S	310	260	260	850	700
17	Cl	320	130	130	100	100
19	K	28200	20900	25900	13600	14000
20	Ca	28700	41500	36300	13700	13700
21	Sc	14	22	22	7	7
22	Ti	4700	5700	4400	4600	5000
23	V	95	135	135	100	100
24	Cr	70	100	100	200	100
25	Mn	690	950	950	850	850
26	Fe	35000	56300	50000	38000	38000
27	Co	12	25	25	8	8
28	Ni	44	75	75	40	40
29	Cu	30	55	55	55	20
30	Zn	60	70	70	70	50

Element	Rock			Soil	
	Wedepohl (1971)	Taylor (1964)	Mason (1966)	Vinogradov (1959)	Bowen (1966)
31 Ga	17	15	15	15	30
32 Ge	1.3	1.5	1.5	1.5	1
33 As	1.7	1.8	1.8	1.8	6
34 Se	0.09	0.05	0.05	0.05	0.2
35 Br	2.9	2.5	2.5	2.5	5
37 Rb	120	90	90	90	100
38 Sr	290	375	375	375	300
39 Y	34	33	33	33	50
40 Zr	160	165	165	165	300
41 Nb	20	20	20	20	0
42 Mo	1	1.5	1.5	1.5	2
44 Ru	0.001	0	0.01	0.01	0
45 Rh	0.001	0	0.005	0.005	0
46 Pd	0.01	0	0.01	0.01	0
47 Ag	0.06	0.07	0.07	0.07	0.1
48 Cd	0.1	0.2	0.2	0.2	0.06
49 In	0.07	0.1	0.1	0.1	0
50 Sn	3	2	2	2	10
51 Sb	0.2	0.2	0.2	0.2	0
52 Te	0.002	0	0.01	0.01	0
53 In	0.5	0.5	0.5	0.5	5
55 Cs	2.7	3	3	3	6
56 Ba	590	425	425	425	500
57 La	44	30	30	30	30
58 Ce	75	60	60	60	50
59 Pr	7.6	8.2	8.2	8.2	0
60 Nd	30	28	28	28	0
62 Sm	6.6	6	6	6	0
63 Eu	1.4	1.2	1.2	1.2	0
64 Gd	8.8	5.4	5.4	5.4	0
65 Tb	1.4	0.9	0.9	0.9	0

Element	Rock			Soil	
	Wedepohl (1971)	Taylor (1964)	Mason (1966)	Vinogradov (1959)	Bowen (1966)
66 Dy	6.1	3	3	3	0
67 Ho	1.8	1.2	1.2	1.2	0
68 Er	3.4	2.8	2.8	2.8	0
69 Tm	0.6	0.48	0.5	0.5	0
70 Yb	0	0	0	0	0
71 Lu	0.6	0.5	0.5	0.5	0
72 Hf	3	3	3	3	6
73 Ta	3.4	2	2	2	0
74 W	1.3	1.5	1.5	1.5	1
75 Re	0.001	0	0.001	0.001	0
76 Os	0	0	0	0	0
77 Ir	0.001	0	0.001	0.001	0
78 Pt	0.005	0	0.01	0.01	0
79 Au	0.004	0.004	0.004	0.004	0
80 Hg	0.03	0.08	0.08	0.08	0.03
81 Tl	0	0	0	0	0
82 Pb	15	12.5	13	13	10
83 Bi	0.2	0.17	0.2	0.2	0
90 Th	11	9.6	7.2	7.2	5
92 U	3.5	2.7	1.8	1.8	1

A.3 EXAMPLE MCNP DECK AS USED IN SOURCE TERM CALCULATIONS

Shown is the MCNP input used for the source term calculation of 150 cm thick Wedepohl rock surrounding a Pu fissioning sphere.

```
 Solid Bare Pu sphere  ENDF/B-VI
1        1            -19.74          -1          imp:n=1
2        2            -2.7             1 -2       imp:n=1
3        0                             2          imp:n=0

1        so       5.05
2        so       155.05

kcode     10000     1.3  25   100
sdef   cel=1     erg=d1    rad=d2    pos=0.0 0.0 0.0
sp1    -3
si2    0.0    5.05
sp2    -21    2
totnu
m1    94238.66c   -0.0001       94239.66c  -0.9380        94240.66c  -0.0580        94241.66c  -0.0013
      94242.66c   -0.0002       95241.66c  -0.0022
m2    1001.66c    -0.0007       3007.66c  -0.00003        4009.66c -0.000002        5011.66c -0.000009
      6000.66c    -0.00032      7014.66c  -0.00002        8016.66c  -0.4725         9019.66c  -0.00072
      11023.66c  -0.0245        12000.66c  -0.0139        13027.66c -0.0783         14028.66c -0.3054
      15031.66c  -0.00081       16032.66c  -0.00031       17000.66c -0.00032        19000.66c -0.0282
      20040.70c  -0.0287        21045.66c  -0.000014      22000.66c -0.0047         23000.66c -0.000095
      24050.66c  -0.00007       25055.66c  -0.00069       26054.66c -0.035          27059.66c -0.000012
      28058.66c  -0.000044      29063.66c  -0.00003       30000.70c -0.00006        31000.66c -0.000017
      32074.70c  -0.0000013     33075.70c  -0.0000017     34080.70c -0.00000009     35081.70c -0.0000029
      37085.66c  -0.00012       38088.70c  -0.00029       39089.66c -0.000034       40090.66c -0.00016
      41093.66   -0.00002       42000.66c  -0.000001      44102.70c -0.000000001    45103.66c -1E-09
      46106.66c -0.00000001     47107.66c  -0.00000006    48000.50c -0.0000001      49000.66c -0.00000007
      50120.70c -0.000003       51121.70c  -0.0000002     52120.70c -0.000000002    53127.66c -0.0000005
      55133.66c -0.0000027      56138.66c  -0.00059       57139.70c -0.000044       58140.70c -0.000075
      59141.70c -0.0000076      60142.70c  -0.00003       62152.70c -0.0000066      63151.66c -0.0000014
      64158.66c -0.0000088      65159.70c  -0.0000014     66164.70c -0.0000061      67165.66c -0.0000018
      68166.70c -0.0000034      69169.55c  -0.0000006     71175.66c -0.0000006      72180.66c -0.000003
      73181.66c -0.0000034      74000.55c  -0.0000013     75187.66c -0.000000001    77193.66c -1E-09
      78000.40c -0.000000005    79197.66c  -0.000000004    80000.40c -0.00000003     82208.66c -0.000015
      83209.66c -0.0000002      90232.66c  -0.000011      92235.66c -2.52E-08        92238.66c -3.4748E-06

prdmp    j    275
print
```

A.4 EXAMPLE MONTEBURNS INPUT FILE AS USED IN SOURCE TERM CALCULATION

```
Godiva Spherical Core Surrounded by geologic media
PC              ! Type of Operating System
2               ! Number of MCNP materials to burn
1               ! MCNP material number #1 (will burn all cells with this mat)
2               ! MCNP material number #2
0.              ! Material #1 volume (cc), input 0 to use mcnp value (if exists)
0.              ! Material #2 volume
4.184E12        ! Power in MWt (for the entire system modeled in mcnp deck)
-200.           ! Recov. energy/fis (MeV); if negative use for U235, ratio other isos
1.1574E-11      ! Total number of days burned (used if no feed)
4               ! Number of outer burn steps
10              ! Number of internal burn steps (multiple of 10)
1               ! Number of predictor steps (+1 on first step), 1 usually sufficient
0               ! Step number to restart after (0=beginning)
FFTFC           ! number of default origen2 lib - next line is origen2 lib location
c:/origen22/libs
.0000001        ! fractional importance (track isos with abs,fis,atom,mass fraction)
0               ! Intermediate keff calc. 0) No 1) Yes
6               ! Number of automatic tally isotopes, followed by list.
92235.66c
92238.66c
94239.66c
94240.66c
94241.66c
94242.66c
41              ! Number of automatic tally isotopes, followed by list.
1001.66c
3007.66c
6000.66c
7014.66c
8016.66c
9019.66c
    .
    .
    .
72180.66c
80000.40c
82208.66c
83209.66c
90232.66c
```

A.5 MATLAB CODE FOR ANALYTICAL SOURCE TERM CALCULATION

```
Cycles = 100*144;         % this is for delta_t = 600s so that means 144 cycles per day
NewSourceXe133=zeros(Cycles,1);
NewSourceXe133m= zeros(Cycles,1);
NewSourceXe131m= zeros(Cycles,1);
NewSourceXe135= zeros(Cycles,1);
NewSourceXe135m= zeros(Cycles,1);
T=zeros(Cycles+1,1);
T(1)=0;

AXe131m=zeros(101,1);
AXe133=zeros(101,1);
AXe133m=zeros(101,1);         % Initializes the activity matrices
AXe135=zeros(101,1);
AXe135m=zeros(101,1);


AXe131m(1)=5.252;
AXe133(1)=2.582E+4;
AXe133m(1)=3.3E+3;            % Sets the first entries to the initial concs
AXe135(1)=1.275E+6;
AXe135m(1)=7.062E+5;

for i=1:Cycles
   T(i+1)=(i)*0.006944;         % (=delta_t in days)
    t=i*0.006944;

%%%%%%%%%%%%%%%%%%%%%%%%%%%%%%%%%%%%%%%%%%%%%%%%%%%%%%%%%%%%%%%%%%%%%%%%%%%
%%%%%%%%%%%%%%%%%%%%       XE-131M CHAIN     %%%%%%%%%%%%%%%%%%%%
%%%%%%%%%%%%%%%%%%%%%%%%%%%%%%%%%%%%%%%%%%%%%%%%%%%%%%%%%%%%%%%%%%%%%%%%%%%

ASb131i=2.256E+5;
ATe131mi=8.511E+4;
ATe131i=1.348E+6;                    % Sets the initial activities
AI131i=9.689E+4;
AXe131mi=5.252;

LIn132=2.97949E+5;
LIn131=2.13885E+5;
LSn131=1.06943E+3;
LSn131m=1.024E+3;
LSb131=43.3405;                      % Sets the decay constants
LTe131m=0.554518;
LTe131=39.92533;
LI131=0.08642;
LXe131m=0.058082;

ASb131=ASb131i*exp(-LSb131*t);

ATe131m=ATe131mi*exp(-LTe131m*t)+((0.15*LTe131m*ASb131i)/(LSb131-LTe131m))*(exp(-...
   LTe131m*t)-exp(-LSb131*t));

ATe131=LTe131*(ATe131i/LTe131*exp(-LTe131*t)+((0.85*LSb131*ASb131i/LSb131)/(LSb131-...
   LTe131))*(exp(-LTe131*t)-exp(-LSb131*t))+((0.222*LTe131m*ATe131mi/LTe131m)/...
```

```
   (LTe131m-LTe131))*(exp(-LTe131*t)-exp(-LTe131m*t))+((0.222)*(0.15)*LSb131*LTe131m*...
   ASb131i/LSb131)*(exp(-LTe131*t)/((LTe131m-LTe131)*(LSb131-LTe131))+exp(-LTe131m*t)/...
   ((LTe131-LTe131m)*(LSb131-LTe131m))+exp(-LSb131*t)/((LTe131-LSb131)*(LTe131m-...
   LSb131))));


AI131=LI131*(AI131i/LI131*exp(-LI131*t)+(0.778*LTe131m*ATe131mi/LTe131m)/(LTe131m-...
   LI131)*(exp(-LI131*t)-exp(-LTe131m*t))+((0.778)*(0.15)*LSb131*LTe131m*ASb131i/...
   LSb131)*(exp(-LI131*t)/((LTe131m-LI131)*(LSb131-LI131))+exp(-LTe131m*t)/((LI131-...
   LTe131m)*(LSb131-LTe131m))+exp(-LSb131*t)/((LI131-LSb131)*(LTe131m-LSb131)))+...
   (LTe131*ATe131i/LTe131)/(LTe131-LI131)*(exp(-LI131*t)-exp(-LTe131*t))+...
   (0.85*LTe131*LSb131*ASb131i/LSb131)*(exp(-LI131*t)/((LTe131-LI131)*(LSb131-...
   LI131))+exp(-LTe131*t)/((LI131-LTe131)*(LSb131-LTe131))+exp(-Sb131*t)/((LI131-...
   LSb131)*(LTe131-LSb131)))+ (0.222*LTe131*LTe131m*ATe131mi/LTe131m)*(exp(-...
   LI131*t)/((LTe131-LI131)*(LTe131m-LI131))+exp(-LTe131*t)/((LI131-LTe131)*(LTe131m-...
   LTe131))+exp(-LTe131m*t)/((LI131-LTe131m)*(LTe131-LTe131m)))+(0.222*0.15*...
   LTe131*LTe131m*LSb131*ASb131i/LSb131)*(exp(-LI131*t)/((LTe131-LI131)*(LTe131m-...
   LI131)*(LSb131-LI131))+exp(-LTe131*t)/((LI131-LTe131)*(LTe131m-LTe131)*(LSb131-...
   LTe131))+exp(-LTe131m*t)/((LI131-LTe131m)*(LTe131-LTe131m)*(LSb131-LTe131m))+...
   exp(-LSb131*t)/((LI131-LSb131)*(LTe131-LSb131)*(LTe131m-LSb131))));


AXe131m(i+1)=LXe131m*(AXe131mi*exp(-LXe131m*t)+((0.011*AI131i)/(LI131-LXe131m))*...
   (exp(-LXe131m*t)-exp(-LI131*t))+(0.011*0.778*LI131*ATe131mi)*(exp(-LXe131m*t)/...
   ((LI131-LXe131m)*(LTe131m-LXe131m))+exp(-LI131*t)/((LXe131m-LI131)*(LTe131m-...
   LI131))+exp(-LTe131m*t)/((LXe131m-LTe131m)*(LI131-LTe131m)))+(0.011*0.778*0.15*...
   LI131*LTe131m*ASb131i)*(exp(-LXe131m*t)/((LI131-LXe131m)*(LTe131m-LXe131m)*...
   (LSb131-LXe131m))+exp(-LI131*t)/((LXe131m-LI131)*(LTe131m-LI131)*(LSb131-LI131))+...
   exp(-LTe131m*t)/((LXe131m-LTe131m)*(LI131-LTe131m)*(LSb131-LTe131m))+...
   exp(-LSb131*t)/((LXe131m-LSb131)*(LI131-LSb131)*(LTe131m-LSb131)))+...
   (0.011*LI131*ATe131i)*(exp(-LXe131m*t)/((LI131-LXe131m)*(LTe131-LXe131m))+...
   exp(-LI131*t)/((LXe131m-LI131)*(LTe131-LI131))+exp(-LTe131*t)/((LXe131m-...
   LTe131)*(LI131-LTe131)))+(0.011*0.85*LI131*LTe131*ASb131i)*(exp(-LXe131m*t)/...
   ((LI131-LXe131m)*(LTe131-LXe131m)*(LSb131-LXe131m))+exp(-LI131*t)/((LXe131m-...
   LI131)*(LTe131-LI131)*(LSb131-LI131))+exp(-LTe131*t)/((LXe131m-LTe131)*(LI131-...
   LTe131)*(LSb131-LTe131))+exp(-Sb131*t)/((LXe131m-LSb131)*(LI131-LSb131)*(LTe131-...
   LSb131)))+(0.011*0.222*LI131*LTe131*ATe131mi)*(exp(-Xe131m*t)/((LI131-LXe131m)*...
   (LTe131-LXe131m)*(LTe131m-LXe131m))+exp(-LI131*t)/((LXe131m-LI131)*(LTe131-LI131)*...
   (LTe131m-LI131))+exp(-LTe131*t)/((LXe131m-LTe131)*(LI131-LTe131)*(LTe131m-LTe131))+...
   exp(-LTe131m*t)/((LXe131m-LTe131m)*(LI131-LTe131m)*(LTe131-LTe131m)))+...
   (0.011*0.15*0.222*LI131*LTe131*LTe131m*ASb131i)*(exp(-LXe131m*t)/((LI131-LXe131m)*...
   (LTe131-LXe131m)*(LTe131m-LXe131m)*(LSb131-LXe131m))+exp(-LI131*t)/((LXe131m-...
   LI131)*(LTe131-LI131)*(LTe131m-LI131)*(LSb131-LI131))+exp(-LTe131*t)/((LXe131m-...
   LTe131)*(LI131-LTe131)*(LTe131m-LTe131)*(LSb131-LTe131))+exp(-LTe131m*t)/...
   ((LXe131m-LTe131m)*(LI131-LTe131m)*(LTe131-LTe131m)*(LSb131-LTe131m))+...
   exp(-LSb131*t)/((LXe131m-LSb131)*(LI131-LSb131)*(LTe131-LSb131)*(LTe131m-...
   LSb131))));

%%%%%%%%%%%%%%%%%%%%%%%%%%%%%%%%%%%%%%%%%%%%%%%%%%%%%%%%%%%%%%%%%%%%%%%%%%%
%%%%%%%%%%%%%%%%%%%%       XE-135 CHAIN     %%%%%%%%%%%%%%%%%%%%
%%%%%%%%%%%%%%%%%%%%%%%%%%%%%%%%%%%%%%%%%%%%%%%%%%%%%%%%%%%%%%%%%%%%%%%%%%%


AI135=0;                    % just initializing the variable
AXe135m=0;
AXe135=0;

```

```
AI135i=4.399E+6;            % starting activities
AXe135mi=7.062E+5;
AXe135i=1.275E+6;

LI135=2.53204;              % these are the decay constants in 1/d
LXe135m=65.23738;
LXe135=1.82008;


AI135=AI135i*exp(-LI135*t);

AXe135m(i+1)=LXe135m*(AXe135mi/LXe135m*exp(-LXe135m*t)+((0.154*AI135i)/(LI135-...
   LXe135m))*(exp(-LXe135m*t)-exp(-LI135*t)));

AXe135(i+1)=LXe135*((AXe135i/LXe135)*exp(-LXe135*t)+((0.846*AI135i)/(LI135-LXe135))*...
   (exp(-LXe135*t)-exp(-LI135*t))+((0.994*AXe135mi)/(LXe135m-LXe135))*(exp(-LXe135*t)-...
   exp(-LXe135m*t))+(0.994*0.154*LXe135m*AI135i)*(exp(-LXe135*t)/((LXe135m-LXe135)*...
   (LI135-LXe135))+exp(-LXe135m*t)/((LXe135-LXe135m)*(LI135-LXe135m))+exp(-LI135*t)/...
   ((LXe135-LI135)*(LXe135m-LI135))));

%%%%%%%%%%%%%%%%%%%%%%%%%%%%%%%%%%%%%%%%%%%%%%%%%%%%%%%%%%%%%%%%%%%%%%%
%%%%%%%%%%%%%%%%%%%%    XE-133 CHAIN    %%%%%%%%%%%%%%%%%%%%%%%%%%
%%%%%%%%%%%%%%%%%%%%%%%%%%%%%%%%%%%%%%%%%%%%%%%%%%%%%%%%%%%%%%%%%%%%%%%

ATe133m=0;
ATe133=0;
AI133=0;                    %just initializing the variable
AXe133m=0;
AXe133=0;

ATe133mi=1.637E+6;
ATe133i=2.809E+5;
AI133i=1.868E+6;            %starting activities
AXe133mi=3.3E+3;
AXe133i=2.582E+4;

LTe133m=18.0168;
LTe133=80.1712;
LI133=0.799785;             %these are the decay constants in 1/d
LXe133m=0.316506;
LXe133=0.132204;


ATe133m=ATe133mi*exp(-LTe133m*t);

ATe133=LTe133*(ATe133i/LTe133*exp(-LTe133*t)+((0.175*ATe133mi)/(LTe133m-LTe133))*...
   (exp(-LTe133*t)-exp(-LTe133m*t)));

AI133=LI133*(AI133i/LI133*exp(-LI133*t)+((0.825*ATe133mi)/(LTe133m-LI133))*...
   (exp(-LI133*t)-exp(-LTe133m*t))+((ATe133i)/(LTe133-LI133))*(exp(-LI133*t)-...
   exp(-LTe133*t))+(0.175*LTe133*ATe133mi)*(exp(-LI133*t)/((LTe133-LI133)*(LTe133m-...
   LI133))+exp(-LTe133*t)/((LI133-LTe133)*(LTe133m-LTe133))+exp(-LTe133m*t)/((LI133-...
   LTe133m)*(LTe133-LTe133m))));

AXe133m(i+1)=LXe133m*(AXe133mi/LXe133m*exp(-LXe133m*t)+((0.02882*AI133i)/(LI133-...
   LXe133m))*(exp(-LXe133m*t)-exp(-LI133*t))+(0.02882*0.825*LI133*ATe133mi)*...
   (exp(-LXe133m*t)/((LI133-LXe133m)*(LTe133m-LXe133m))+exp(-LI133*t)/((LXe133m-...
```

```
    LI133)*(LTe133m-LI133))+exp(-LTe133m*t)/((LXe133m-LTe133m)*(LI133-LTe133m)))+...
    (0.02882*LI133*ATe133i)*(exp(-LXe133m*t)/((LI133-LXe133m)*(LTe133-LXe133m))+...
    exp(-LI133*t)/((LXe133m-LI133)*(LTe133-LI133))+exp(-LTe133*t)/((LXe133m-LTe133)*...
    (LI133-LTe133)))+(0.02882*0.175*LI133*LTe133*ATe133mi)*(exp(-LXe133m*t)/((LI133-...
    LXe133m)*(LTe133-LXe133m)*(LTe133m-LXe133m))+exp(-LI133*t)/((LXe133m-...
    LI133)*(LTe133-LI133)*(LTe133m-LI133))+exp(-LTe133*t)/((LXe133m-LTe133)*(LI133-...
    LTe133)*(LTe133m-LTe133))+exp(-LTe133m*t)/((LXe133m-LTe133m)*(LI133-LTe133m)*...
    (LTe133-LTe133m))));

AXe133(i+1)=LXe133*(AXe133i/LXe133*exp(-Xe133*t)+(0.97118*LI133)*(((AI133i/LI133)/...
    (LI133-LXe133))*(exp(-LXe133*t)-exp(-LI133*t))+ (0.825*ATe133mi)*(exp(-LXe133*t)/...
    ((LI133-LXe133)*(LTe133m-LXe133))+exp(-LI133*t)/((LXe133-LI133)*(LTe133m-LI133))+...
    exp(-LTe133m*t)/((LXe133-LTe133m)*(LI133-LTe133m)))+ (ATe133i)*(exp(-LXe133*t)/...
    ((LI133-LXe133)*(LTe133-LXe133))+exp(-LI133*t)/((LXe133-LI133)*(LTe133-LI133))+...
    exp(-LTe133*t)/((LXe133-LTe133)*(LI133-LTe133)))+(0.175*LTe133*ATe133m)*...
    (exp(-LXe133*t)/((LI133-LXe133)*(LTe133-LXe133)*(LTe133m-LXe133))+exp(-LI133*t)/...
    ((LXe133-LI133)*(LTe133-LI133)*(LTe133m-LI133))+exp(-LTe133*t)/((LXe133-LTe133)*...
    (LI133-LTe133)*(LTe133m-LTe133))+exp(-LTe133m*t)/((LXe133-LTe133m)*(LI133-Te133m)*...
    (LTe133-LTe133m))))+((AXe133mi)/(LXe133m-LXe133))*(exp(-LXe133*t)-...
    exp(-LXe133m*t))+(0.02882*LXe133m*AI133i)*(exp(-LXe133*t)/((LXe133m-LXe133)*...
    (LI133-LXe133))+exp(-LXe133m*t)/((LXe133-LXe133m)*(LI133-LXe133m))+exp(-LI133*t)/...
    ((LXe133-LI133)*(LXe133m-LI133)))+(0.02882*0.825*LXe133m*LI133*ATe133mi)*...
    (exp(-LXe133*t)/((LXe133m-LXe133)*(LI133-LXe133)*(LI133-LTe133m))+exp(-LXe133m*t)/...
    ((LXe133-LXe133m)*(LI133-LXe133m)*(LI133-LTe133m))+exp(-LI133*t)/((LXe133-LI133)*...
    (LXe133m-LI133)*(LTe133m-LI133))+exp(-LTe133m*t)/((LXe133-LTe133m)*(LXe133m-...
    LTe133m)*(LI133-LTe133m)))+(0.02882*LXe133m*LI133*ATe133i)*(exp(-LXe133*t)/((LXe133m-…
    LXe133)*(LI133-LXe133)*(LI133-LTe133))+exp(-LXe133m*t)/((LXe133-LXe133m)*(LI133-...
    LXe133m)*(LI133-LTe133))+exp(-LI133*t)/((LXe133-LI133)*(LXe133m-LI133)*(LTe133-...
    LI133))+exp(-LTe133*t)/((LXe133-LTe133)*(LXe133m-LTe133)*(LI133-LTe133)))+...
    (0.02882*0.175*LXe133m*LI133*LTe133*ATe133mi)*(exp(-LXe133*t)/((LXe133m-LXe133)*...
    (LI133-LXe133)*(LI133-LTe133)*(LI133-LTe133m))+exp(-LXe133m*t)/((LXe133-LXe133m)*...
    (LI133-LXe133m)*(LI133-LTe133)*(LI133-LTe133m))+exp(-LI133*t)/((LXe133-LI133)*...
    (LXe133m-LI133)*(LTe133-LI133)*(LTe133m-LI133))+exp(-LTe133*t)/((LXe133-LTe133)*...
    (LXe133m-LTe133)*(LI133-LTe133)*(LTe133m-LTe133))+exp(-LTe133m*t)/((LXe133-
    LTe133m)*(LXe133m-LTe133m)*(LI133-LTe133m)*(LTe133-LTe133m))));


%%%%%%%%%%%%%%%%%%%%%%%%%%%%%%%%%%%%%%%%%%%%%%%%%%%%%%%%%%%%%%%%%%%%%%%%%%%%
%%%%%%%%%%%%%%%%%%%%%%%%%%%%%%%%%%%%%%%%%%%%%%%%%%%%%%%%%%%%%%%%%%%%%%%%%%%%
%%%%%%%%%%%%%%%%%%%%%%%%%%%%%%%%%%%%%%%%%%%%%%%%%%%%%%%%%%%%%%%%%%%%%%%%%%%%


end

semilogy(T,AXe131m,T,AXe133,T,AXe133m,T,AXe135)

for i=2:Cycles+1
    NewSourceXe133(i)= AXe133(i)-AXe133(i-1)*exp(-LXe133*.006944);
    NewSourceXe133m(i)= AXe133m(i)-AXe133m(i-1)*exp(-LXe133m*.006944);
    NewSourceXe131m(i)= AXe131m(i)-AXe131m(i-1)*exp(-LXe131m*.006944);
    NewSourceXe135(i)= AXe135(i)-AXe135(i-1)*exp(-LXe135*.006944);
    NewSourceXe135m(i)= AXe135m(i)-AXe135m(i-1)*exp(-LXe135m*.006944);
end

semilogy(T,NewSourceXe133)
```

A.6 FULL MATLAB CODE FOR THE VERTICAL TRANSPORT MODEL

```
format long;
clc


%%%%%%%%%%%%   System Grid Setup    %%%%%%%%%%%%%%%
Cycles = 100*144; % at 5 minutes per cycle, 144 cycles = 1 day
N = 200;
M = 7;

%%%%%%%%%%%    Surface Pressure History    %%%%%%%
Static_Pressure=10^5;
delP=(2/30)*Static_Pressure;
Press=zeros(Cycles,1);
for ii=0:(Cycles-1)
    Press(ii+1)=Static_Pressure + delP*cos(8.7266E-6*ii*600);
end
PressNew = Press(:) - Static_Pressure;

%%%%%%%%%% Define Physical Parameters      %%%%%%
Del_f = 1*10^(-3);
Del_m = 1;
phi_f = 1;                                  % fracture porosity
phi_m = 0.1;                                % matrix porosity
p_0 = Static_Pressure;                      % static pressure [ Pa ]
mu = 2*10^(-5);                             % air viscosity [ Pa _ s ]
k_m = 10^(-15);                             % matrix permeability
alpha_f = (2*Del_f )^2*p_0/(12*mu*phi_f);   % pneumatic diffusivity of fracture
alpha_m = k_m*p_0/(mu*phi_m);               % pneumatic diffusivity of matrix
FLOOR = 500;                                % depth of watertable/bedrock floor
D = 3.1*10^(-6);                            % Xenon diffusivity [m^2/s ]
Del_t = 600;                                % length of time step
Del_x = FLOOR/N;                            % cell height
Del_y = Del_m/M;                            % cell width
Source2 = 2.582*10^(4);                     % source term [ Ci/kt ]
Contam_Volume = Del_m*300*phi_m;            % initial radionuclide volume [m^3]
Interface = ceil(2*N/5);                    % contaminant/fresh-air buffer interface
Concentration = Source2/((200-Interface)*6); % initial conc per volume [bq/(m^3 kt)]
decay = 1.530139E-6;                        %decay constant [s^-1]

%%%%%%%% Initialize Variables  %%%%%%%%%%%%%%%%%%%%%%%%%

OUTFLOW=zeros(Cycles,1);        % cumulative fraction outflow over original total conc
OVERFLOW=zeros(Cycles,1);       % cumulative outflow [Ci/kton]
INSTANT_OVERFLOW = zeros(Cycles,1); % outflow at each cycle [Ci/kt]
NewSource=zeros(Cycles,1);      % amount of contam produced in prev. time step

C_SURF = zeros(Cycles,1);       % these variables just track..
C_OVERALL = zeros(Cycles,1);    % various concs in the system.
C_OVERALL_ACTUAL = AXe133;

CONC = zeros(N,M,2);            % tracks Conc in a given time step
C_PROV = zeros(N,M);            % provisional Conc from step1 of FRAM
C_LAGRANGE = zeros(N,M);        % Conc bound from local Lagrange Eq.

C_0 = zeros(N,M);               % Just stores initial conc at t=0
C_Graph=zeros(N,M);             % Used to graph Conc, for convenience

ADVECTION_A = zeros(N,M);%%%%%%%%%%%%%%%%%%%%%%%%%
ADVECTION_Stablilize = zeros(N,M);              %
ADVECTION_Filtered1 = zeros(N,M);               %
ADVECTION_Filtered2 = zeros(N,M);               %
```

```
u = zeros(N-1,M-1,2);                           %
                                                %
C_AVG1 = zeros(N,M);                            %
C_AVG2 = zeros(N,M);                            %
C_AVG3 = zeros(N,M);                            %
C_AVG4 = zeros(N,M);                            %
C_AVG5 = zeros(N,M);      %These are all        %
                                                %
Conc_var = zeros(3,1);    %used in the FRAM     %
C_MIN1 = zeros(N,M);                            %
C_MIN2 = zeros(N,M);      %calculation of the   %
C_MIN3 = zeros(N,M);                            %
C_MAX1 = zeros(N,M);      %various advection    %
C_MAX2 = zeros(N,M);                            %
C_MAX3 = zeros(N,M);      %terms                %
                                                %
X1 = zeros(N,M);                                %
X2 = zeros(N,M);                                %
X3 = zeros(N,M);                                %
XA = zeros(N,M);                                %
XB = zeros(N,M);                                %
epsA = zeros(N,M);                              %
epsB = zeros(N,M);%%%%%%%%%%%%%%%%%%%%%%%%%%%%%%%


p = zeros(N,M,2);
f = zeros(N,M);
F = zeros(N,M);
fract_matrix_interact = zeros(N,Cycles);
b_x = zeros(N, 1);
B_x = zeros(N, 1);
t = zeros(Cycles,1);

e1 = zeros(N,M);
d1 = zeros(N,M);
g1 = zeros(N,M);
h1 = zeros(N,M,2);

e2 = zeros(N,M);
d2 = zeros(N,M);
g2 = zeros(N,M);
h2 = zeros(N,M,2);

e1(N,1,:) = 1;
d1(N,1,:) = 0;
g1(1,1,:) = 1;
h1(1,1,:) = 0;

for k = 1 : N
    e1(k,M,:) = 1;
    d1(k,M,:) = 0;
    g1(k,1,:) = 1;
    h1(k,1,:) = 0;
end

e2(3,1,:) = 1;
d2(3,1,:) = 0;
g2(N-2,1,:) = 1;
h2(N-2,1,:) = 0;

for k = 3 : N-2
    e2(k,M,:) = 1;
    d2(k,M,:) = 0;
    g2(k,1,:) = 1;
    h2(k,1,:) = 0;
end
```

```
129
130   %%%%%%%%%  Sets Initial Contaminant Distribution  %%%%%
131   CONC(Interface:N,2:M,2) = Concentration;              %Initial radionuclide distribution
132   C_0(Interface:N,2:M,2)=Concentration;
133
134   C_OVERALL(1)= sum(sum(CONC(4:N,:,2)));
135
136   C_PROV(:,:) = CONC(:,:,1);
137   C_LAGRANGE(:,:) = CONC(:,:,1);
138
139   %%%%%%%%%%%%%%%%%%%%%%%%%%%%%%%%%%%%%%%%%%%%%%%%%%%%%%%%%%%%%%%%
140   %%%%%%%%%%  STARTING CALCULATION   %%%%%%%%%%%%%%%%
141   %%%%%%%%%%%%%%%%%%%%%%%%%%%%%%%%%%%%%%%%%%%%%%%%%%%%%%%%%%%%%%%%
142   for time = 2 : Cycles
143       e1(N,1,:) = 1;
144       d1(N,1,:) = 0;
145       g1(1,1,:) = 1;
146       h1(1,1,:) = 0;
147
148       for k = 1 : N
149           e1(k,M,:) = 1;
150           d1(k,M,:) = 0;
151           g1(k,1,:) = 1;
152           h1(k,1,:) = 0;
153       end
154
155       e2(3,1,:) = 1;
156       d2(3,1,:) = 0;
157       g2(N-2,1,:) = 1;
158       h2(N-2,1,:) = 0;
159
160       for k = 3 : N-2
161           e2(k,M,:) = 1;
162           d2(k,M,:) = 0;
163           g2(k,1,:) = 1;
164           h2(k,1,:) = 0;
165       end
166
167       CONC(1:3,1,2) = 0;
168       CONC(1:3,1,1) = 0;
169       CONC(4,1,2)=0;
170       CONC(4,1,1)=0;
171
172
173       if time ~= 2
174           NewConcentration = (NewSourceXe133(time)-...
175               sum(sum(NewDecaySource(:,:,time))))/((200-Interface)*6);
176           %NewDecaySource(:,:,time) = CONC(:,:,2)*(1-exp(-decay*delta_t));
177   %this determines the decayed amount in each cell to be used for modeling of daughter
178          CONC(:,:,2) = CONC(:,:,2)*exp(-decay*Del_t);
179           CONC(:,:,2)= CONC(:,:,2) + NewDecaySource(:,:,time);
180   %this adds the migrating portion of NewSource resulting from parent decay
181           CONC(Interface:N,2:M,2)=CONC(Interface:N,2:M,2)+NewConcentration;
182   %this adds the stationary portion of NewSource to the original contam. distribution
183           NewSource(time)=sum(sum(CONC(:,:,2)))-sum(sum(CONC(:,:,1)));
184   %this variable simply tracks how much new source is added each cycle
185       end
186
187
188       p(1,1,2)= PressNew(time);
189       p(:,:,1)= p(:,:,2);
190       CONC(:,:,1)= CONC(:,:,2);
191       u(:,:,1)= u(:,:,2);
192
193       % Coefficients
194       a_y = -(alpha_m .* Del_t ./ Del_y .^2);
```

```
195         b_y = (1 + 2 .* alpha_m .* Del_t ./ Del_y .^2);
196         c_y = a_y;
197         a_x = -(alpha_f .* Del_t ./ Del_x .^2);
198         c_x = a_x;
199
200         f(:,2:M) = p(:,2:M,2);
201         h1(:,:,1)= h1(:,:,2);
202
203         %%%% Thomas Algorithm Solution for Matrix %%%%
204         for k = 1 : N
205             for l = M-1:-1:2
206                 e1(k,l)= -a_y ./(b_y + c_y .* e1(k,l+1));
207                 d1(k,l)=(f(k,l)- c_y .* d1(k,l+1)) ./ (b_y + c_y .* e1(k,l+1));
208             end
209             for l = 2 : M
210                 g1(k,l)= g1(k,l-1) .* e1(k,l);
211                 h1(k,l,2)= h1(k,l-1,2) .* e1(k,l) + d1(k,l);
212             end
213         end
214         %%%% Determine Fracture-Matrix Interaction %%%%
215         for k = 1 :N
216             f(k,1)= p(k,1,1)- p( k,1,1) * Del_y * 0.1*sum(g1(k,:)) - Del_y *...
217                     0.1*(sum(h1(k,:,1) - h1(k,:,2)));
218         end
219         for k = 1 : N
220             b_x(k)= 1 + 2 .* alpha_f .* Del_t ./ Del_x .^2 - Del_y * 0.1*sum(g1(k,:));
221         end
222         %%%% Thomas Algorithm Solution for Fracture %%%%
223         for k = N-1:-1:1
224             e1(k,1) = -a_x ./ (b_x(k) + c_x .* e1(k+1,1));
225             d1(k,1) = (f(k,1) - c_x .* d1(k+1,1)) ./ (b_x(k)+ c_x .* e1(k+1,1));
226         end
227         %%%% Final Calculation of Fracture Pressure %%%%
228         for k = 2 : N
229             p(k,1,2) = e1(k,1) .* p(k-1,1,2) + d1(k,1);
230         end
231         %%%% Final Calculation of Matrix Pressure %%%%
232         for k = 1 : N
233             for l = 2 : M
234                 p(k,l,2) = g1(k,l) * p(k,1,2) + h1(k,l,2);
235             end
236         end
237
238         %%%% Calculation of fluid-flow velocities %%%%
239         for k = 2:N-1
240             u(k,1,2)= (2*Del_f).^2 / (12 * mu) .* (p(k+1,1,2) - p(k-1,1,2)) ./ (2*Del_x);
241             for l = 2 : M-1
242                 u(k,l,2)= -k_m / mu .* (p(k,l+1,2) - p(k,l-1,2)) ./ (2*Del_y);
243             end
244         end
245         u(1,1,2)= u(2,1,2);
246
247         %%%% Starting FRAM Processing of Advection %%%%
248         for k = N-2:-1:2
249             C_AVG1(k,1) = CONC(k,1,1) + CONC(k-1,1,1);
250             C_AVG2(k,1) = CONC(k+1,1,1) + CONC(k,1,1);
251             C_AVG3(k,1) = CONC(k+1,1,1) - CONC(k,1,1);
252             C_AVG4(k,1) = CONC(k,1,1) - CONC(k-1,1,1);
253             ADVECTION_A(k,1) = 0.5 * Del_t/Del_x * ...
254                 (C_AVG1(k,1) * u(k,1,2) - C_AVG2(k,1) *u( k+1,1,2));
255             ADVECTION_Stablilize(k,1) = 0.25 * Del_t^2 / Del_x^2 * ...
256                 (u(k +1,1,2).^2 * C_AVG3(k,1) - u(k,1,2).^2 * C_AVG4(k,1));
257             C_PROV(k,1) = CONC(k,1,1) - ADVECTION_A(k,1) + ADVECTION_Stablilize(k,1);
258
259             for l = 2 : M-2
260                 C_AVG1(k,l) = CONC(k,l,1) + CONC(k,l-1,1);
```

```
            C_AVG2(k,l) = CONC(k,l+1,1) + CONC(k,l,1);
            C_AVG3(k,l) = CONC(k,l+1,1) - CONC(k,l,1);
            C_AVG4(k,l) = CONC(k,l,1 ) - CONC(k,l-1,1);
            ADVECTION_A(k,l) = 0.5 * Del_t/Del_y * ...
                (C_AVG1(k,l) * u(k,l,2) - C_AVG2(k,l) * u(k,l+1,2) ) ;
            ADVECTION_Stablilize(k,l) = 0.25 * Del_t^2 /Del_y^2 * ...
                (u(k,l+1,2)^2 * C_AVG3(k,l) - u(k,l,2)^2 * C_AVG4(k,l));
            C_PROV(k,l) = CONC(k,l,1) - ADVECTION_A(k,l) + ADVECTION_Stablilize(k,l);
        end
    end
    for k = 2 : N-2
        C_AVG5(k,1) = 0.5 * (CONC(k,1,1)+ CONC(k-1,1,1));
        C_LAGRANGE(k,1) = C_AVG5(k,1) - C_AVG5(k,1) * Del_t/Del_x * (u(k+1,2)-u(k,2));
        for l = 2 :M-2
            C_AVG5(k,l) = 0.5 * CONC(k,l,1)+ CONC(k-1,l,1);
            C_LAGRANGE(k,l) = C_AVG5(k,l) - C_AVG5(k,l) * Del_t/Del_x * (u(k,l+1,2)-...
                u( k,l,2));
        end
    end
    for k  = 3 : N-2
        C_COMP1(1) = C_LAGRANGE(k-2,1);
        C_COMP1(2) = C_LAGRANGE(k-1,1);
        C_COMP1(3) = C_LAGRANGE(k,1);
        C_MIN1(k,1) = min( C_COMP1);
        C_MAX1(k,1) = max( C_COMP1);

        C_COMP2(1) = C_LAGRANGE(k-1,1);
        C_COMP2(2) = C_LAGRANGE(k,1);
        C_COMP2(3) = C_LAGRANGE(k +1,1);
        C_MIN2(k,1) = min( C_COMP2);
        C_MAX2(k,1) = max( C_COMP2);

        C_COMP3(1) = C_LAGRANGE(k,1);
        C_COMP3(2) = C_LAGRANGE(k +1,1);
        C_COMP3(3) = C_LAGRANGE(k +2,1);
        C_MIN3(k,1) = min( C_COMP3);
        C_MAX3(k,1) = max( C_COMP3);

        for l=3 : M-2
            C_COMP1(1) = C_LAGRANGE(k,l-2);
            C_COMP1(2) = C_LAGRANGE(k,l-1);
            C_COMP1(3) = C_LAGRANGE(k,l);
            C_MIN1(k,l) = min( C_COMP1);
            C_MAX1(k,1) = max( C_COMP1);

            C_COMP2(1) = C_LAGRANGE(k,l-1);
            C_COMP2(2) = C_LAGRANGE(k,l);
            C_COMP2(3) = C_LAGRANGE(k,l +1);
            C_MIN2(k,1) = min( C_COMP2);
            C_MAX2(k,1) = max( C_COMP2);

            C_COMP3(1) = C_LAGRANGE(k,l);
            C_COMP3(2) = C_LAGRANGE(k,l +1);
            C_COMP3(3) = C_LAGRANGE(k,l +2);
            C_MIN3(k,1) = min( C_COMP3);
            C_MAX3(k,1) = max( C_COMP3);
        end
    end

    for k=3 :N-2
        if (C_MIN1(k,1)<= C_PROV(k-1,1)) && (C_PROV(k-1,1) <= C_MAX1(k,1))
            X1(k,1) = 0;
        else
            X1(k,1) = 1;
        end
        if (C_MIN2(k,1)<= C_PROV(k,1)) && (C_PROV(k,1) <= C_MAX2(k,1))
```

```
            X2(k,1) = 0;
        else
            X2(k,1) = 1;
        end
        if (C_MIN3(k,1)<= C_PROV(k+1,1)) && (C_PROV(k+1,1) <= C_MAX3(k,1))
            X3(k,1) = 0;
        else
            X3( k,1)= 1;
        end

        XA(k,1)= max(X1(k,1),X2(k,1));
        XB(k,1)= max(X2(k,1),X3(k,1));

        epsA(k,1)= 0.5 * (u(k,1,2) * 0.5 * Del_x - u(k,1,2)^2 * Del_t);
        epsB(k,1)= 0.5 * (u(k+1,1,2) * 0.5 * Del_x - u(k+1,1,2)^2 * Del_t);

        for l = 2 :M-2
            if (C_MIN1(k,l)<= C_PROV(k,l-1)) && (C_PROV(k,l-1) <= C_MAX1(k,l))
                X1(k,l)= 0;
            else
                X1(k,l)= 1;
            end
            if (C_MIN2(k,l)<= C_PROV( k,l)) && (C_PROV( k,l)<= C_MAX2(k,l))
                X2(k,l)= 0;
            else
                X2(k,l)= 1;
            end
            if (C_MIN3(k,l)<= C_PROV( k,l +1)) && (C_PROV( k,l +1) <= C_MAX3(k,l))
                X3(k,l)= 0;
            else
                X3(k,l)= 1;
            end

            XA(k,l)= max(X1(k,l),X2(k,l));
            XB(k,l)= max(X2(k,l),X3(k,l));
            epsA(k,l)= 0.5 * (u(k,l,2) * 0.5 * Del_x - u(k,l,2)^2 * Del_t);
            epsB(k,l)= 0.5 * (u(k,l+1,2) * 0.5 * Del_x - u(k,l+1,2)^2 * Del_t);
        end
    end


    for k = 3 :N-2
        ADVECTION_Filtered1(k,1)= Del_t / Del_x * (0.5 * XB(k,1) * epsB(k,1) * ...
            (CONC(k+1,1,1) - CONC(k,1,1)));
        ADVECTION_Filtered2(k,1)= - Del_t / Del_x ^2 * (0.5 * XA(k,1) * epsA(k,1) * ...
            (CONC(k,1,1) - CONC(k-1,1,1)));
        for l = 2 :M-1
            ADVECTION_Filtered1(k,l)= Del_t / Del_x * (0.5 * XB(k,l) * epsB(k,l) * ...
                (CONC(k,l+1,1) - CONC(k,l,1)));
            ADVECTION_Filtered2(k,l)= -Del_t / Del_x ^2 * (0.5 * XA(k,l) * ...
                 epsA( k,l) * (CONC(k,l,1) - CONC(k,l-1,1)));
        end
    end

    %%%% Starting Solution Scheme for Concentrations %%%%

    %coefficients for full-implicit scheme
    A_y = -(D.* Del_t ./ (Del_y.^2));
    B_y = (1 + 2 .* D( 2).* Del_t ./ (Del_y .^2));
    C_y = A_y;
    A_x = -(D.* Del_t ./ (Del_x .^2));
    B_x = (1 + 2 .* D .* Del_t ./ Del_x .^2);
    C_x = A_x;

    %Incorporate matrix past : conc distribution,advection process and filtering
    F(:,2:M) = CONC(:,2:M,1) - ADVECTION_A(:,2:M) +ADVECTION_Stablilize(:,2:M) + ...
```

```
            ADVECTION_Filtered1(:,2:M) + ADVECTION_Filtered2(:,2:M);
    h2(:,:,1)= h2(:,:,2);

    %%%% Thomas Algorithm Solution for Matrix %%%%
    for k = 3:N-2
        for l = M-1:-1:2
            e2(k,l)= -A_y ./(B_y + C_y .* e2(k,l+1));
            d2(k,l)=(F(k,l) - C_y .* d2(k,l+1)) ./(B_y + C_y .* e2(k,l+1));
        end
        for l = 2:M
            g2(k,l)= g2(k,l-1).* e2(k,l);
            h2(k,l,2)= h2(k,l-1,2) .* e2(k,l) + d2(k,l);
        end
    end

    %Fracture-Matrix Interaction Term, Advection, Filtering
    for k = 3:N-2
        fract_matrix_interact(k,time)= CONC(k,1,1) * Del_y * 0.1*sum(g2(k,2:M)) +...
             Del_y * 0.1*(sum(h2(k,2:M,1) - h2(k,2:M,2)));
        F(k,1)= CONC(k,1,1) - ADVECTION_A(k,1) +ADVECTION_Stablilize(k,1) + ...
                 ADVECTION_Filtered1(k,1) + ADVECTION_Filtered2(k,1)-...
                 fract_matrix_interact(k,time);
    end
    for k = 3 : N-2
        B_x(k)= 1 + 2 .* D.* Del_t ./ Del_x.^2 - Del_y * 0.1*sum(g2(k,2:M));
    end
    %%%% Thomas Algorithm Solution for Fracture %%%%
    for k = 4 :N-2
        e2(k,1)= -A_x ./(B_x(k)+ C_x .* e2(k-1,1));
        d2(k,1)=(F(k,1) - C_x .* d2(k-1,1))./(B_x(k)+ C_x .* e2(k-1,1));
    end


    %%%% Final Calculation of Fracture Concentrations %%%%
    for k = N-3:-1:3
        CONC(k,1,2)= e2(k,1) * CONC(k+1,1,1)+ d2(k,1);
    end

    %%%% Final Calculation of Matrix Concentrations %%%%
    for k = N-2:-1:3
        for l = 3:M
            CONC(k,l,2)= g2(k,l) * CONC(k,1,1) + h2(k,l,2);
        end
        CONC(k,2,2)= g2(k,2) * CONC(k,2,1) + h2(k,2,2);
    end


    %%%%%%%%%% Determine Conc Outflow  %%%%%%%%%%%%%%%%%%

    deloverflow = CONC(4,1,2);

    OVERFLOW(time)=OVERFLOW(time-1)+deloverflow;
    C_OVERALL(time) = sum(sum(CONC(4:N,:,2))) - deloverflow;
    C_SURF(time)= CONC(4,1,2);

    OUTFLOW(time)=OVERFLOW(time)/C_OVERALL(1);
    OUTFLOW(time)
    INSTANT_OVERFLOW(time) = deloverflow;
    time
end

%%%%%%% End of Calculation %%%%%
```

DISCLAIMER FOR UNITED STATES GOVERNMENT SPONSORED WORK

This report was prepared as an account of work sponsored by an agency of the United States Government. Neither the United States Government nor any agency thereof, nor any of their employees, makes any warranty, expressed or implied, or assumes any legal liability or responsibility for the accuracy, completeness, or usefulness of any information, apparatus, product, or process disclosed, or represents that its use would infringe privately owned rights. Reference herein to any specific commercial product, process, or service by name, trademark, manufacturer, or otherwise does not necessarily constitute or imply its endorsement, recommendation or favoring buy the United States Government or any agency thereof. The views and opinions of authors expressed herein do not necessarily state or reflect those of the United States Government or any agency thereof.

References

1 CTBTO Preparatory Commission. Status of Signature and Ratification. [Internet]. 2010 [cited 2010 October]. Available from: http://www.ctbto.org/the-treaty/status-of-signature-and-ratification.

2 CTBTO Preparatory Commission. Monitoring Technologies: How they work. [Internet]. [cited 2010 October]. Available from: http://www.ctbto.org/verification-regime/monitoring-technologies-how-theywork/seismic-monitoring/page-1.

3 Hwang, Shuen-Cheng; Lein, Robert D.; Morgan, Daniel A. Kirk-Othmer Encyclopedia of Chemical Technology. 5th ed. Wiley; 2005.

4 Bowyer, TW; Abel, KH; Hubbard, CW; Panisko, ME; Reeder, PL; Thompson, RC; Warner, RA. Field testing of collection and measurement of radioxenon for the Comprehensive Test Ban Treaty. Journal of Radioanalytical and Nuclear Chemistry. 240(1):109-122, 1999.

5 Biegalski, K.; Biegalski, S.; and Williams, D.L. Proceedings of 21st Seismic Research Review.; September 1999; Las Vegas, NV.

6 Carrigan, CR.; Heinle, R.A.; Hudson, G.B.; Nitao, J.J.; and Zucca, J.J. Barometric gas transport along faults and its application to nuclear test-ban monitoring. In: International Workshop on Mt.Unzen. Lawrence Livermore National Laboratories, UCRL-JC-127585; June 1997; Shimabara, Japan.

7 Hannon, Willard J. The Non-Proliferation Experiment. In: Proceedings of the Symposium on the Non-Proliferation Experiment: Results and implications for Test Ban Treaties. Lawrence Livermore National Laboratory, CONF-9409100; April 1994. p. 2.1–2.11.

8 Baldwin, M.J.; Bradford, R.P.; Hopkins, S.P.; Townsend, D.R.; and Harris-West, B.L. Geology, geophysics, and physical properties of the U12n.25 Non-Proliferation Experiment site. In: Proceedings of the Symposium on the Non-Proliferation Experiment: Results and implications for Test Ban Treaties. Lawrence Livermore National Laboratory, CONF-9409100. p. 5.1-.514, April 1994.

9 Wilson, C.R.; and Witherspoon, P.A. An investigation of laminar flow in fractured porous rocks. Technical Report. University of California, Berkeley; 1970.

10 Nelson, R.A.; and Handin, J. Experimental study of fracture permeability in porous rock. American Association of Petroleum Geologists, Bulletin. 61(2):227–236, 1977.

11 Gale, J.E. Assessing the permeability characteristics of fractured rock. Technical Report. Lawrence Berkeley Laboratory, Berkeley, California; 1979.

12 Nilson, R.H.; and Lie, K.H. Double-porosity modeling of oscillatory gas motion and contaminant transport in a fractured porous medium. International Journal of

Numerical and Analytical Methods in Geomechanics. 14:565-585, 1990.

13 Grisak, G.E. and J.F. Pickens. Solute transport through fractured media: the effect of matrix diffusion. Water resources Research. 16(4):719-730, 1980.

14 Tang, D.H.; E.O. Frind; and E.A. Sudicky. Contaminant transport in fractured porous media: analytical solution for a single fracture. Water Resources Research. 17(3):555–564, 198.

15 Neretnieks, I. and A. Rasmuson. An approach to modeling radionuclide migration in a medium with strongly varying velocity and block sizes along the flow path. Water resources Research. 20(12):1823–1836, 1984.

16 Gringarten, A.C. Interpretation of tests in fissured and multilayered reservoirs with double-porosity behavior. Journal of Petroleum Technology. 36:549–564, 1984.

17 Chen, Z.X. Transient flow of slightly compressible fluids through double-porosity, double-permeability systems. Transport in Porous Media. 4: 147–184, 1989.

18 Nitao, J.J. Reference manual for the NUFT flow and transport code version 1.0. Technical Report, UCRL-ID-113520. Lawrence Livermore National Laboratory; 1996.

19 Carrigan, C.R. The non-proliferation experiment and gas sampling as an on-site inspection activity: a progress report. Technical Report LLNL-CONF-9404100. Lawrence Livermore National Laboratory; 1994.

20 Carrigan, C.R.; R.A. Heinle; G.B. Hudson; J.J. Nitao; and J.J. Zucca. Trace gas emissions on geological faults as indicators of underground nuclear testing. Nature. 382:528–531, 1996.

21 Wikipedia user "Fastfission;" images released into the public domain. Wikipedia: Nuclear weapon. [Internet]. 2006 [cited 2010 October]. Available from: http://en.wikipedia.org/wiki/Nuclear_weapon.

22 Niksch, L.A. North Korea's Nuclear Weapons Program. Congressional Research Service Issue Brief for Congress. The Library of Congress; 2005.

23 Sublette, Carey. What Are the Real Yields of India's Test? [Internet]. 2001 [cited 2010 October]. Available from: http://nuclearweaponarchive.org/India/IndiaRealYields.html.

24 Nilson, R.H., E.W. Peterson, K.H. Lie, N.R. Burkhard, and J.R Hearst. Atmospheric pumping: a mechanism causing vertical transport of contaminated gases through fractured permeable media. Journal of Geophysical Research. 96(B13):21933–21948, 1991.

25 Stacey, Weston M. Nuclear Reactor Physics. New York: John Wiley & Sons, Inc.; 2001.

26 Bird, R.B., W.E. Stewart, and E.N. Lightfoot. Transport Phenomena. New York: John Wiley; 1960.

27 Epstein, Norman. On tortuosity and the tortuosity factor in flow and diffusion through porous media. Chemical Engineering Science. 44(3):777-779, 1989.

28 Carslaw, H.S. and J.C. Jaeger. Conduction of heat in solids. New York: Oxford University Press; 1959.

29 Chatwin, P.C. On the longitudinal dispersion of passive contaminant in oscillatory flows in tubes. Journal of Fluid Mechanics. 7:513–527, 1975.

30 Kurzweg, U.H. Enhanced heat conduction in oscillating viscous flows within parallel plate channels. Journal of Fluid Mechanics. 156:91-300, 1985.

31 Chapman, M. FRAM — A nonlinear damping algorithm for the continuity equation. Journal of Computational Physics. 44(1):84–103, 1981.

32 Chapman, M. and E.M. Waisman. A noise suppression algorithm for the numerical solution of Maxwell's equations. Journal of Computational Physics. 58(1):44 – 58, 1985.

33 Press, W.H., B.P. Flannery, S.A. Teukolsky, and W.T. Vetterling. Numerical Recipes: The Art of Scientific Computing. Cambridge University Press; 1986.

34 Hirt, C.W. Heuristic Stability Theory for finite-difference Equations. Journal of Computational Physics. 2:339– 335, 1968.

35 G. Le Petit, P. Armand, G. Brachet, T. Taffary, J. P. Fontaine, P. Achim, X. Blanchard, J. C. Piwowarczyk, F. Pointurier. Contribution to the development of atmospheric radioxenon monitoring. Journal of Radioanalytical and Nuclear Chemistry. 276(2):391-398, 2008.

Vita

Justin D. Lowrey was born in Dallas, Texas and graduated valedictorian from Skyline High School of Dallas, Texas in 2002. Lowrey attended the University of Texas at Austin, majoring in Physics and Astronomy, and graduated with highest honors in 2006. He was a graduate student in high energy physics and honors physics teaching associate at the University of California at Santa Barbara for two years before transferring back to the University of Texas at Austin in 2009. Lowrey is currently a graduate student in the Department of Mechanical Engineering at the University of Texas at Austin.

Email address: justin@lowreys.net

This thesis was typed by the author.